Journal of Metamorphic Geology

WILEY

Journal of METAMORPHIC GEOLOGY

ORIGINAL ARTICLE OPEN ACCESS

Petrochronology of High-Pressure Veins Reveals the Evolution of Fluid Sources in Subducted Oceanic Crust (Rocciavrè Eclogites, W. Alps)

Clément Herviou[1,2,3] | Guillaume Bonnet[4,5] | Samuel Angiboust[2] | Aitor Cambeses[6] | Tom Raimondo[7]

[1]Department of Earth, Marine and Environmental Sciences, University of North Carolina, Chapel Hill, North Carolina, USA | [2]LGL-TPE, UMR5276, Université de Lyon 1, Université de Lyon 1, ENS de Lyon, CNRS, Lyon-Villeurbanne, France | [3]Institut de physique du globe de Paris, Université Paris Cité, CNRS UMR7194, Paris, France | [4]Institute of Geological Sciences, University of Bern, Bern, Switzerland | [5]Institut des Sciences de la Terre deParis, CNRS-INSU, Sorbonne Université, Paris, France | [6]Department of Mineralogy and Petrology, Faculty of Sciences, University of Granada, Granada, Spain | [7]UniSA STEM, University of South Australia, Adelaide, South Australia, Australia

Correspondence: Clément Herviou (herviou@ipgp.fr)

Received: 29 December 2023 | **Revised:** 7 October 2024 | **Accepted:** 12 December 2024

Funding: This study was partly funded by an RGF-Alpes project (BRGM) and by an ENS de Lyon grant to S. Angiboust.

Keywords: fluid inclusions | fluid–rock interactions | high-pressure veins | petrochronology | subduction fluids | Western Alps

ABSTRACT

The Rocciavrè massif is a large eclogitized ophiolitic fragment exposed in the Western Alps (Piemonte, Italy) exhibiting an almost complete sequence of the subducted Liguro-Piemont lithosphere. Raman spectroscopy on carbonaceous material in metasediments from Rocciavrè and the juxtaposed Orsiera massif indicates maximum temperatures in the range ~510°C–550°C, whereas thermodynamic modelling in mafic lithologies reveals peak burial metamorphic conditions of 550°C–590°C/2.2–3.0 GPa for both units, suggesting the absence of a metamorphic gap between them. Late Jurassic (ca. 151–158 Ma) zircons extracted from Rocciavrè metagabbros reflect the crystallization age near the seafloor, and no alpine metamorphic rims have been detected. The garnet-omphacite-rutile–dominated Fe-Ti metagabbros are crosscut by a variety of high-pressure vein systems, including garnet-rich, omphacite-rich, omphacite-quartz–rich, glaucophane-quartz–rich and winchite-actinolite-talc veins. Vein textures, mineral assemblages and mineral compositions suggest the formation of garnet-rich and omphacite-rich veins at conditions close to peak burial and the successive formation of omphacite-quartz–rich and glaucophane-quartz–rich types by reopening former omphacite-rich veins at eclogite- to epidote-blueschist-facies conditions along the exhumation path. In contrast, winchite-actinolite-talc veins are interpreted as retrograde greenschist-facies features. In situ U-Pb dating of monazite constrains the age omphacite-quartz–rich veining at 40.4 ± 0.2 Ma. Major and trace element mapping of vein assemblages shows various zoning patterns of omphacite and rutile crystals for a large variety of elements (e.g., Fe, Mg, Mn, Sr, Li, U and Cr). Aqueous primary fluid inclusions trapped in vein-filling and host-rock minerals have intermediate to high salinity values, interpreted to reflect the partial signature of hydrothermal alteration preserved up to eclogite-facies conditions. High fluid inclusion salinity values associated with the presence of N_2 (± CO_2) suggest the presence of fluids produced by local dehydration reactions at peak burial. In contrast, some inclusions from glaucophane-quartz–rich veins contain a low to intermediate salinity CO_2-CH_4–bearing fluid interpreted as reflecting a sedimentary contribution and a larger scale of fluid circulation. In addition, the mineralogy of winchite-actinolite-talc veins associated with high-salinity values suggests an ultramafic signature. The successive steps of vein formation are interpreted to record the evolution from a closed to open chemical system during exhumation, with late sedimentary and ultramafic fluid contributions that witness the mobility of fluids within the mafic sequence and transport distances

likely reaching the kilometre scale. The Rocciavrè massif, which shares a similar metamorphic history to the Monviso Lago Superiore Unit further south, enables a precise characterization of fluid–rock interaction processes in subduction from eclogite-facies to greenschist-facies conditions.

1 | Introduction

In subduction zones, the increase of pressure–temperature (P–T) conditions during burial of the downgoing oceanic lithosphere causes the successive breakdown of hydrous minerals (e.g., Schmidt and Poli 2014). The release of fluids caused by these dehydration reactions affects the convergent plate boundary dynamics, notably by operating a key role in earthquake nucleation and arc magma generation (Hacker et al. 2003; Rupke et al. 2004). The volume of fluids and their composition are partially controlled by the geochemistry of devolatilizing rocks, whereas their scales of migration are governed by transient changes in permeability. All these factors influence the extent of fluid–rock interactions and of the related rheological and chemical modifications (e.g., van Keken et al. 2011; Bebout and Penniston-Dorland 2016; Smye and England 2023). It is therefore paramount to identify fluid sources and pathways to assess their impact on rocks at depth and their importance in subduction systems.

Exhumed high-pressure low-temperature (HP-LT) metamorphic complexes, now exposed across worldwide orogens, provide snapshots of the processes that occurred millions of years ago along fossil subduction zones (Maruyama, Liou, and Terabayashi 1996; Guillot et al. 2009; Agard et al. 2009, 2018). By providing data at various scales, the characterization of these exhumed metamorphic rocks complements the geophysical observations made on active subduction zones and helps to understand the processes occurring beyond the reach of deep drilling.

Because of their ability to flow, interact with rocks and lead to mineral crystallization once supersaturated, the fluids circulating at depths in subduction zones are particularly challenging to track. Metamorphic veins, i.e., mineralized fractures, are considered the best-preserved witnesses of fluid pathways and fluid–rock interactions (Oliver and Bons 2001; Bons, Elburg, and Gomez-Rivas 2012). Veins are particularly abundant in low-grade to blueschist-facies sediments of exhumed accretionary complexes (Fisher et al. 1995; Fagereng 2011; Ujiie et al. 2018; Muñoz-Montecinos et al. 2020; Cerchiari et al. 2020; Rajič et al. 2023a, 2023b; Platt et al. 2024) but scarcer in HP-LT rocks buried at greater depths. The characterization of veins containing eclogite-facies mineral assemblages therefore gives valuable clues on fluid circulation processes in deep subduction environments (Spandler and Hermann 2006; Beinlich et al. 2010; Spandler, Pettke, and Rubatto 2011; John et al. 2012; Taetz et al. 2018; Locatelli et al. 2019; Hoover et al. 2023). These veins also provide information on the mechanisms of fracturing at depths where fluid release is expected to cause embrittlement and generate intraslab seismicity (Hacker et al. 2003; Kita et al. 2006; Abers et al. 2006).

In the Western Alps, the Liguro-Piemont domain corresponds to a nappe-stack of HP-LT units buried from ~30- to 80-km depths (Agard 2021) that is particularly well-suited to study deep subduction processes. In this complex, the Rocciavrè massif (Piemonte, Italy) is a well-exposed coherent piece of oceanic lithosphere buried up to eclogite-facies conditions during subduction (e.g., Pognante 1985). This study aims first at refining the peak P–T conditions reached by the Rocciavrè eclogites, in order to provide a well-defined framework to investigate subduction processes. Then, the main target of this work is to characterize successive high-pressure veins occurring in mafic rocks and to analyse their petrology, geochemistry and geochronology in order to constrain the fluid sources and scales of fluid migration during deep oceanic crust subduction.

2 | Geological Setting

2.1 | The Western Alps Liguro-Piemont Domain: Fragments of a Slow-Spreading Oceanic Lithosphere Recovered From Subduction

The Western Alps were formed as a consequence of the east- to south-east dipping subduction of the Liguro-Piemont and Valais slow-spreading oceans below Adria/Apulia (Schmid et al. 1996, 2017; Handy et al. 2010; Agard and Handy 2021; Agard 2021). This phase of oceanic subduction started in the Late Cretaceous and was followed by an episode of continental subduction (Chopin 1984; Compagnoni and Rolfo 2003; Bonnet et al. 2022; Mendes et al. 2023) that ended with the collision of Eurasia and Adria/Apulia, which has been ongoing for ~34–32 Myr (e.g., Simon-Labric et al. 2009; Bellanger et al. 2015).

Fragments of the Liguro-Piemont (ultra) slow-spreading oceanic lithosphere (Lagabrielle and Cannat 1990; Lagabrielle, Vitale Brovarone, and Ildefonse 2015; Decrausaz et al. 2021) were exhumed from subduction and are now continuously exposed in the internal zones of the Western Alps forming a nappe-stack known as Liguro-Piemont (or Piemonte-Liguria) domain (e.g., Agard 2021). In this complex, metasediments (the so-called Schistes Lustrés) are volumetrically dominant and embed variable amounts of a generally dismembered oceanic basement made of mafic and ultramafic rocks (Deville et al. 1992; Herviou et al. 2022). Most radiochronological ages suggest the formation of the Liguro-Piemont discontinuous mafic crust during the Middle and Late Jurassic (Manatschal and Müntener 2009; Li et al. 2013; De Togni et al. 2024), whereas the Schistes Lustrés, which correspond to former pelagic–hemipelagic seafloor deposits, are Late Jurassic to Late Cretaceous in age (Lemoine and Tricart 1986; Deville et al. 1992; Lemoine 2003).

These rocks were buried between ~30- and 80-km depth during subduction (Berger and Bousquet 2008; Agard 2021; Herviou et al. 2022), reaching peak burial from ca. 60 to 40 Ma before being sliced off the downgoing plate and exhumed as tectonic slices from the Late Eocene to the Miocene (Agard et al. 2002; Rubatto and Hermann 2003; Schwartz et al. 2007, 2020; Angiboust and Glodny 2020; Dragovic, Angiboust, and Tappa 2020; Ghignone et al. 2021b; Herviou and Bonnet 2023; Gyomlai et al. 2023). This stack of tectonic units therefore corresponds to a deep

accretionary complex (see Angiboust et al. 2022) formed by successive events of slab offscraping and underplating (Agard et al. 2009, 2018; Agard 2021; Herviou et al. 2022).

Several independent subduction slices were identified along transects crossing the Liguro-Piemont domain (Fudral 1996; Lagabrielle 1987; see Herviou et al. 2022 for a compilation). Recently, the overall structure of the complex was reappraised using the compilation of metamorphic, structural, lithostratigraphic and geochronological data in each tectonic slice demonstrating a tri-modal distribution of units with an increase of metamorphic grade from the Liguro-Piemont Upper (LPU, 320°C–400°C; 1.2–1.9 GPa) to the Middle (LPM, 415°C–475°C; 1.7–2.2 GPa) and Lower units (LPL, 500°C–580°C; 2.2–2.8 GPa; Figure 1a; Herviou et al. 2022). The LPU and LPM units metamorphosed up to blueschist-facies conditions are dominated by metasediments (< 90%) and separated from the eclogitic and much richer in mafic and ultramafic rocks (> 40%) LPL units by a major extensional contact (Philippot 1990; Ballèvre, Lagabrielle, and Merle 1990; Ballèvre and Merle 1993). The different stratigraphic successions of the units suggest a variability of slicing mechanisms with strain localization in different horizons of weakness (talcschists, serpentinites, pelites; Herviou et al. 2022; Herviou and Bonnet 2023). Furthermore, the peak burial depths of the LPU (~35–45 km), LPM (~55–65 km) and LPL (~70–80 km) units are similar to those inferred for offscraping and underplating in both modern and fossil subduction zones, reflecting major changes in mechanical coupling along the plate interface at these depth ranges (Herviou et al. 2022; Agard et al. 2018; Plunder et al. 2015).

2.2 | The Rocciavrè Massif: A Large Coherent Slab Piece Metamorphosed up to Eclogite-Facies Conditions

This study focuses on the Rocciavrè massif, a large (~8 × 4 km) almost flat-lying mafic-ultramafic body occurring in the eclogitic LPL units of the Cottian Alps (Piemonte, Italy; Figure 1a–c). It structurally overlies the Dora-Maira internal crystalline massif, which is mostly composed of the 'Silvery Micaschist unit' in the studied locality (Sandrone et al. 1993). This massif contains a coherent portion of Liguro-Piemont oceanic lithosphere with serpentinites at its base, overlaid by a thick sequence of metagabbros, and in rare places by a thin sequence of oceanic metasediments occurring at the top of the pile (Figures 2a and 1b–c). Like in the other LPL units, this succession of sedimentary deposits is limited to the Late Jurassic–Early Cretaceous and devoid of the thick Upper Cretaceous calcschist series generally occurring in the blueschist-facies LPU and LPM units (Herviou et al. 2022). Most of the metagabbros are of Mg-Al composition and are intruded by scarcer Fe-Ti metagabbros occurring as dykes and sills (Pognante, Lombardo, and Venturelli 1982; Pognante and Toscani 1985; Figure 2a). Rodingite lenses, which are common in Alpine ultramafic massifs (e.g., Zanoni, Rebay, and Spalla 2016;

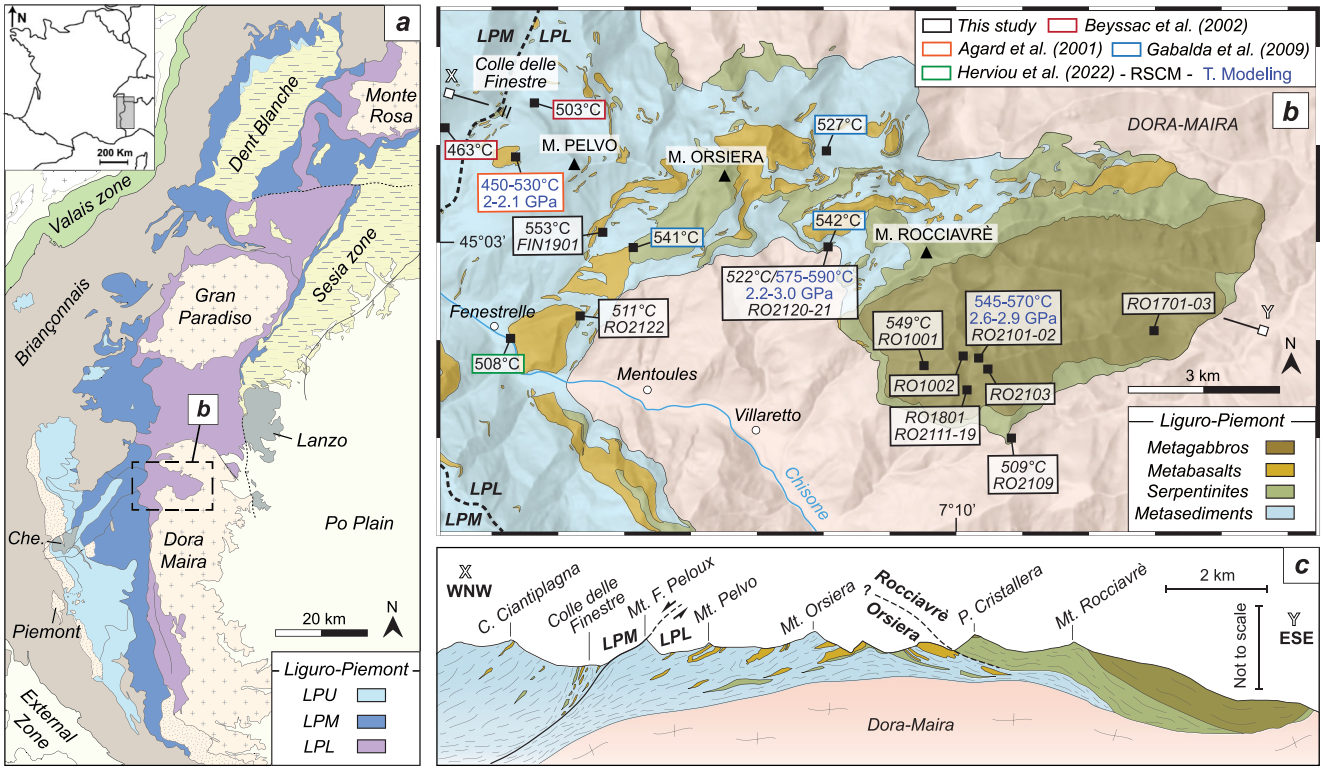

FIGURE 1 | Maps and cross-section of the studied area. (a) Structural map of the Western Alps focused on the Liguro-Piemont domain and showing the distribution of the three types of units. Modified after Herviou et al. (2022). (b) Geological map of the Rocciavrè and Orsiera massifs displaying the location of the studied samples and peak pressure–temperature estimations from this work and previous studies (Agard, Jolivet, and Goffe 2001; Beyssac et al. 2002; Gabalda 2009; Herviou et al. 2022). Modified after Servizio Geologico d'Italia (1999). (c) Schematic cross-section of the Orsiera and Rocciavrè units, modified after Servizio Geologico d'Italia (1999). Abbreviations: Che.: Chenaillet ophiolite; LPU: Liguro-Piemont Upper units; LPM: Liguro-Piemont Middle units; LPL: Liguro-Piemont Lower units; RSCM: Raman Spectroscopy on Carbonaceous Material; T. Modelling: thermodynamic modelling.

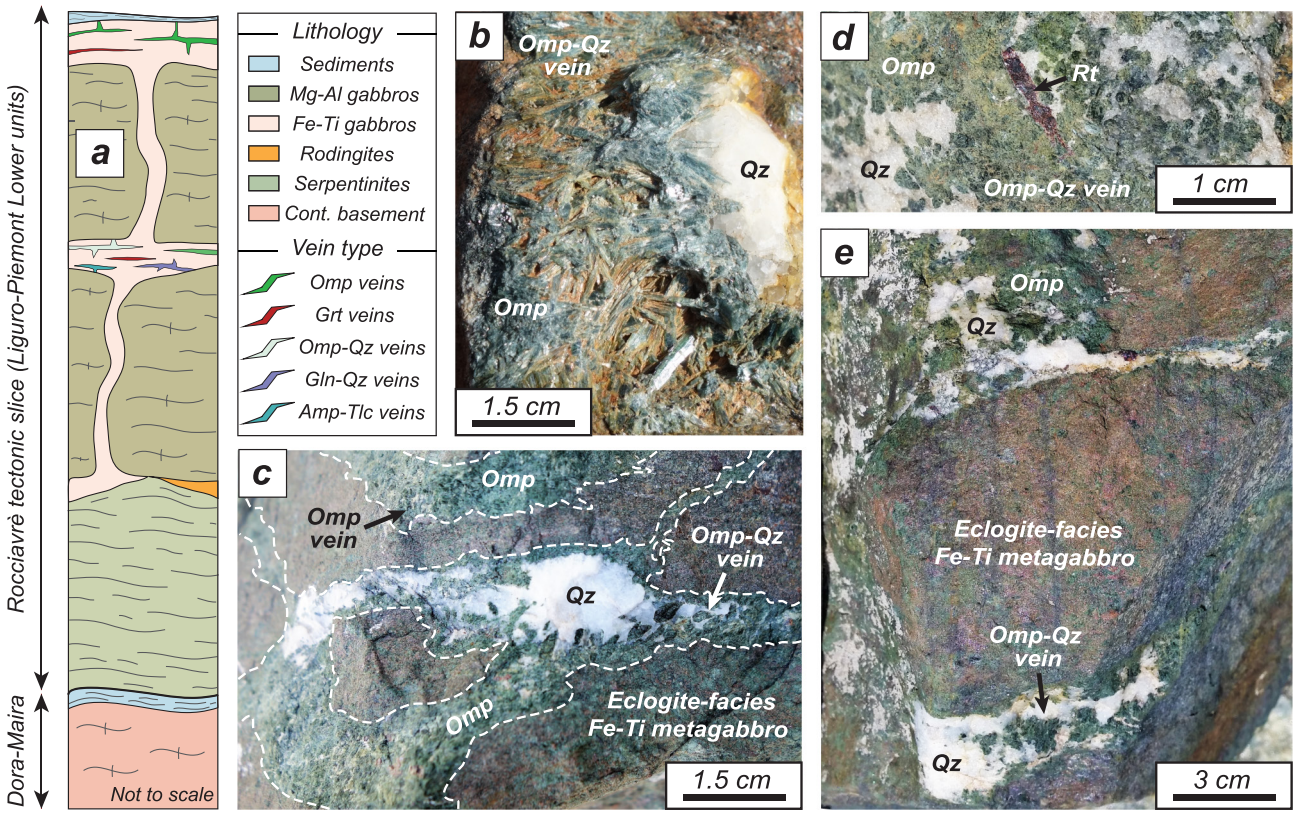

FIGURE 2 | Stratigraphic column and field observations of high-pressure veins. (a) Stratigraphic column of the Rocciavrè unit lying on top of the Dora-Maira internal crystalline massif, displaying the various types of high-pressure veins observed in two main Fe-Ti metagabbro horizons. (b) Omphacite-quartz–rich vein. (c) Connected omphacite-bearing veins crosscutting eclogite-facies metagabbros and showing the formation of omphacite-quartz–rich veins by reopening omphacite-rich veins. (d) Cm-size prismatic crystal of rutile in an omphacite-quartz–rich vein. (e) Omphacite-quartz–rich veins crosscutting Fe-Ti metagabbros and starting to form a brecciated texture. Abbreviations: Cont.: continental; Amp: amphibole; Gln: glaucophane; Grt: garnet; Omp: omphacite; Qz: quartz; Rt: rutile; Tlc: talc.

Ferrando et al. 2010), are frequently found at the lithological boundary between serpentinites and metagabbros (Figure 2a).

The Rocciavrè massif is juxtaposed to the west to the Orsiera massif, also metamorphosed at eclogite-facies conditions but containing larger amounts of metasediments embedding ultramafic and mafic rocks (Figure 1b,c). On its easternmost part, the Orsiera massif is juxtaposed to the LPM blueschist-facies units by a major tectonic contact, particularly well-exposed in the Colle delle Finestre (Figure 1b,c; e.g., Agard, Jolivet, and Goffe 2001; Agard 2021). In contrast to Rocciavrè, mafic rocks of the Orsiera massif mostly correspond to metabasalts and prasinites—typical Alpine metamafics of basaltic composition, usually of volcano-detrital origin and that have commonly been very retrogressed during exhumation (e.g., Lagabrielle and Polino 1985; Figure 1b,c). The difference in the nature of exposed material and the discordance of the stratigraphic succession with the almost complete Liguro-Piemont column of Rocciavrè structurally on top of the Orsiera metasediments (Figure 1c) suggest that Orsiera and Rocciavrè massif correspond to two distinct tectonic slices that were stacked during exhumation (see Herviou et al. 2022, their §7.1). This distinction is also supported by the difference of peak burial ages, with In situ high-silica phengite Ar-Ar ages at 61–53 Ma for Orsiera massif metasediments (Agard et al. 2002) and a phengite-glaucophane-epidote-apatite Rb-Sr age at 46.3 ± 2.8 Ma in the Rocciavrè metagabbros (Angiboust and Glodny 2020). The Rocciavrè and Orsiera units might therefore respectively correspond to two different types of eclogitic LPL units, the mafic-ultramafic–dominated (MUM units of Agard 2021; ≥ 60% mafic-ultramafic rocks) and the sediment-dominated units (S units of Agard 2021; ≥ 60% sediments), with the latter potentially representing the former cover of the mafic-ultramafic units (Agard 2021; Herviou et al. 2022).

In the Rocciavrè tectonic slice, metamorphosed up to eclogite-facies conditions, the eclogitic assemblages are particularly well-expressed in the Fe-Ti metagabbros (Figures 2–3) and have been the subject of extensive petrographic investigations from the late 70s to the 90s (Pognante 1979, 1981, 1984, 1985, 1991; Pognante and Kienast 1987). The Rocciavrè metagabbros were moderately affected by ductile deformation, compared with those of analogous neighbouring LPL units (Philippot and Kienast 1989; Philippot and Van Roermund 1992; Angiboust et al. 2011, 2012b; Locatelli et al. 2018), leading to the preservation of initial magmatic textures and the development of eclogitic assemblages in coronitic textures, except in higher strain zones (Pognante 1985). Peak P–T conditions of Rocciavrè eclogites were estimated at ~450°C–500°C for a minimum pressure of 1.2–1.3 GPa (Pognante 1981, 1985, 1991; Pognante and Kienast 1987). These estimates are much lower than those estimated for other LPL units such as the Lago-Superiore unit in the Monviso massif (~550°C–580°C, 2.6–2.8 GPa; Groppo and Castelli 2010; Angiboust et al. 2012b; Locatelli et al. 2018;

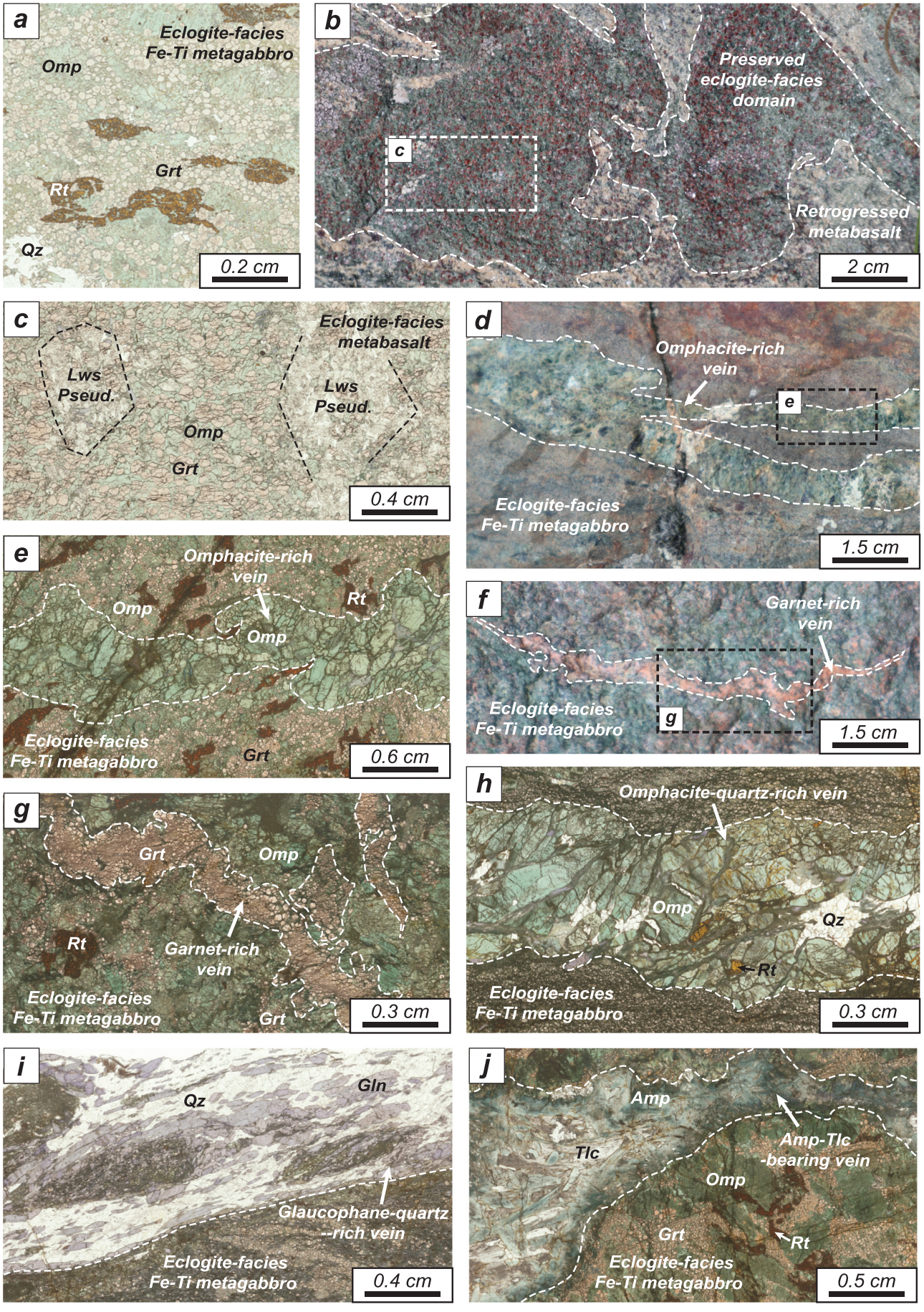

FIGURE 3 | Legend on next page.

FIGURE 3 | Field and thin section pictures of Rocciavrè and Orsiera eclogites and of the different types of high-pressure vein. Observed in Rocciavrè Fe-Ti metagabbros. (a) Rocciavrè eclogite-facies Fe-Ti metagabbro (RO2101). (b) and (c) Preserved eclogite-facies domain in an Orsiera metabasalt showing pluri-millimetre-large lawsonite pseudomorphs (RO2120). (d) and (e) Omphacite-rich veins (RO2112). (f) and (g) Garnet-rich veins (RO2113). (h). Omphacite-quartz–rich vein. Note the presence of quartz inclusions in some omphacite crystals (RO2111). (i) Glaucophane-quartz–rich vein. Note the plastic deformation and different orientations of the blue-amphibole showing intense shearing (RO2116). (j) Blue-green amphibole-talc–rich vein (RO2117). Abbreviations: Amp: amphibole; Gln: glaucophane; Grt: garnet; Lws: lawsonite; Omp: omphacite; Qz: quartz; Rt: rutile; Tlc: talc.

Caurant et al. 2023), the Savoy Lower unit (~500°C–550°C, 2.3–2.9 GPa; Plunder et al. 2012; Ghignone et al. 2021a; Herviou et al. 2022) and the Zermatt-Saas unit (500°C–600°C, 2.2–3.0 GPa; Bucher et al. 2005; Angiboust et al. 2009). However, no re-evaluation of Rocciavrè eclogites peak P–T conditions has been conducted for decades.

In the Orsiera tectonic slice, peak P–T conditions have been estimated in mafic rocks at 450 ± 50°C for a minimum pressure of 1.2 GPa (Bouffette and Caron 1991) and at 450°C–540°C/2–2.1 GPa for metasediments (Agard, Jolivet, and Goffe 2001; Beyssac et al. 2002; Gabalda et al. 2009; Herviou et al. 2022).

We herein report the occurrence of a wide variety of high-pressure veins including omphacite-rich, garnet-rich, omphacite-quartz–rich, glaucophane-quartz–rich and winchite-actinolite-talc veins. These veins, on which this study is focused, were observed crosscutting the Fe-Ti metagabbros of the Rocciavrè massif. No vein sets have been observed in the Mg-Al metagabbros, which appear almost systematically devoid of high-pressure index minerals (and are therefore not suited for thermobarometric purposes).

3 | Analytical Methods

3.1 | Sampling Strategy

In order to investigate the petrochronological evolution and the high-pressure fluid records of the Rocciavrè eclogites, representative samples containing well-preserved parageneses were selected and included: Fe-Ti metagabbros (RO1002, RO1703, RO2101, RO2103), Mg-Al metagabbros (RO1701), various types of metamorphic veins crosscutting the Fe-Ti metagabbros (RO1801, RO2102, RO2111, RO2112, RO2113, RO2114, RO2115, RO2116, RO2117, RO2119) and metasediments (RO1001, RO2109).

In addition, eclogite-facies metabasalts (RO2120) and metasediments (FIN1901, RO2121, RO2122) were collected in the Orsiera massif for thermobarometric purposes, in order to detect potential peak P–T differences between the Rocciavrè and Orsiera LPL units.

All the samples used in this work are displayed on the simplified geological map of Figure 1b. A list including the GPS location and mineralogy of all samples is presented in Data S1. Additional field pictures are displayed in Data S2.

3.2 | Characterization of Mineralogy and Mineral Chemistry

Mineral assemblages were determined using optical microscopy and scanning electron microscopy (SEM; Zeiss Supra 55VP equipped with an SSD detector PTG Sahara for EDS analysis; ISTeP, Sorbonne Université, Paris). SEM-EDS maps were acquired, in order to image the distribution of element zonation in the investigated phases. Additional microphotographs are displayed in Data S3.

Mineral compositions were obtained by electron probe microanalysis (EPMA) at Camparis (Sorbonne Université, Paris) using a Cameca SX-FIVE and a Cameca SX-100. Point analysis was conducted using classical analytical conditions (15-kV acceleration voltage, 10-nA beam current allowing a ~2-μm beam size in wavelength-dispersive spectroscopy mode) using diopside (Ca, Mg, Si), $MnTiO_3$ (Mn, Ti), orthoclase (K, Al), Fe_2O_3 (Fe), albite (Na) and Cr_2O_3 (Cr) as standards for calibration of elements (in parentheses). Representative mineral analyses are presented in Data S4. Monazite chemical maps were acquired with a 20-kV acceleration voltage and a 40-nA beam current, using diopside (Ca, Si), apatite (P), REE-enriched glasses (Y, REE), UO_2 (U) and monazite (Th) as standards for calibration of elements (in parentheses). The signals used were Si Kα, P Kα, Ca Kα, Y Lα, La Lα, Ce Lα, Nd Lβ, Eu Lβ, Th Mα and U Mβ. These compositional maps of monazite crystals are displayed in Data S5.

3.3 | Raman Spectroscopy on Carbonaceous Material Thermometry

To estimate the maximum temperature recorded by metasediments at peak burial, Raman spectra of carbonaceous material (RSCM) were obtained using a Renishaw inVia Spectrometer at ENS Paris. The excitation light was provided by a laser (Cobolt Fandango) at 514.5 nm and at a power of 50 mW, focused on the sample using a ×100 objective (Leica). Eleven to sixteen spectra per sample were acquired in the range of 1000–2000 cm^{-1}; acquisition time was 30–90 s with 10% of laser power following the spectral acquisition parameters of Beyssac et al. (2002). Peak position, baseline correction and band widths were determined using Peakfit software, and Matlab codes, and temperatures were determined using Beyssac et al. (2002) methodology. This method has an uncertainty on estimated temperatures of approximately ±50°C (Beyssac et al. 2002).

3.4 | Whole-Rock Geochemistry and Thermodynamic Modelling

To conduct thermodynamic modelling, major element whole-rock geochemistry was acquired at ALS global using an ICP-OES spectrometer on two representative samples exposing well-preserved eclogite-facies mineral assemblages: a Fe-Ti metagabbro from the Rocciavrè massif (RO2101) and a metabasalt from the Orsiera tectonic slice (RO2120). Whole-rock analyses are presented in Data S6.

P–T phase equilibria diagrams for a specific bulk composition (pseudosections) were calculated in the range 1.5–3.0 GPa/400°C–650°C by minimization of Gibbs free energy using Perple_X software version 7.0 (Connolly 1990, 2005, 2009) and the internally consistent dataset hp04 (Holland and Powell 1998; modified in 2004). These pseudosections were conducted using the system SiO_2-Al_2O_3-FeO-Fe_2O_3-MnO-MgO-CaO-Na_2O-TiO_2-H_2O and adding K_2O for RO2101 containing phengite crystals. TiO_2 was considered in the calculation because of the abundance of rutile in both samples. Solution models were selected from Holland and Powell (1998) for garnet, epidote/clinozoisite and phengite; Holland, Baker, and Powell (1998) for chlorite; Green, Holland, and Powell (2007) for omphacite; Diener et al. (2007) for clinoamphiboles; Fuhrman and Lindsley (1988) for feldspar; and Holland and Powell (1991, 1998) for H_2O, considered in excess. All other phases were considered as pure endmembers and talc as an ideal solution. XFe^{3+} ($Fe^{3+}/(Fe^{2+}+Fe^{3+})$; in mol.%) ratios of 0.2 and 0.3 for RO2101 and RO2120, respectively, were set up considering the mass balance between Fe^{3+}-rich omphacite and Fe^{2+}-rich garnet (Droop 1987; Data S4). These values are in the same range as the ones used for eclogites from analogous Alpine units (e.g., Locatelli et al. 2018).

3.5 | Characterization of Fluid Inclusion Generations and Compositions

Fluid inclusion (FI) analyses were performed on 100-μm-thick double-polished sections. FIs were observed using optical microscopy, in order to characterize their morphology, gas/liquid ratios and textural location within crystals. To characterize the pristine fluid present during crystal growth, only FIs showing good textural evidence of primary entrapment were selected (i.e., either isolated or occurring in clusters oriented parallel to crystal growth directions; Roedder 1984; Van den Kerkhof and Hein 2001). FIs were carefully examined, and we selected inclusions with the most regular shapes in order to avoid as much as possible postentrapment modification of their chemistry (e.g., Diamond, Tarantola, and Stünitz 2010; Diamond and Tarantola 2015). FIs aligned on trails crosscutting several mineral grains, interpreted as secondary inclusions in recrystallized fractures, were not considered in this study.

Salinity, gas content and nature of minerals in the 265 studied FIs were determined by Raman spectroscopy, by focusing the laser on the liquid phase, on the gas bubble and on solids respectively. Raman measurements were performed at GeoRessources laboratory (Université de Lorraine, Nancy) using a LabRAM HR spectrometer (Horiba Jobin-Yvon) equipped with a liquid nitrogen-cooled CCD detector, a 600-groove·mm^{-1} grating for salinity measurements and a 1800-groove·mm^{-1} grating for gas analysis. The excitation light was provided by a 514.532-nm Ar^+ laser (Stabilite 2017, Newport Spectra-Physics) at the power of 200, 160 or 120 mW, focused on the sample using a 100× objective (Olympus).

Salinity values were determined using the method described in Caumon et al. (2013). Raman spectra of water in the studied FIs were acquired with the same spectrometers used for calibration by Caumon et al. (2013), and salinity was determined using the intensity ratio of two defined positions (3260 and 3425 cm^{-1}) after subtraction of a linear baseline (Data S7). This method has an uncertainty of ±0.4 wt.% NaCl eq. and is well-suited and accurate for the characterization of FI salinity in high-pressure rocks (Herviou et al. 2021).

For gas analysis, Raman spectra were corrected using an ICS function (Intensity Correction System) to normalize the instrument response with wavelength. Gas spectra were identified using peak positions compiled by Frezzotti, Tecce, and Casagli (2012). CO_2 was detected by the presence of the Fermi diad (Fermi 1931; 1285- and 1388-cm^{-1} peaks), N_2 by its main peak at 2331 cm^{-1} and CH_4 by its main peak at 2917 cm^{-1} (Data S7). The presence of N_2 was later confirmed by subtracting the peak area of atmospheric N_2 to the peak area of the N_2 potentially detected inside the inclusion.

3.6 | LA-ICP-MS Trace Element Mapping

LA-ICP-MS trace element mapping was conducted on an omphacite-quartz–rich vein (RO1801) using a Resonetics M-50-LR 193-nm excimer laser coupled to an Agilent 8900x Quadrupole ICP-MS at Adelaide Microscopy, University of Adelaide. The mapping conditions and protocols were similar to those outlined in Raimondo et al. (2017). Preablation of each raster scan was completed to minimize the effect of redeposition (25 μm, 75% overlap), followed by 20 s of washout and 10 s of background measurement. A beam diameter of 25 μm, line spacing of 25 μm and repetition rate of 10 Hz were employed, resulting in an energy density of 3.5 J/cm^2 on the sample. Standards including reference glasses NIST SRM 610 (Pearce et al. 1997; Jochum et al. 2011a) and GSD-1G (Jochum et al. 2011b) were analysed in duplicate every 2 h during the mapping session. A beam diameter of 43 μm was used for all standard analyses, which included five preablation shots (43 μm, 75% overlap) followed by 20 s of washout, 30 s of background measurement and 40 s of ablation. Data acquisition was performed in time-resolved analysis mode as a single continuous experiment. Each analysis comprised a suite of 35 elements, and dwell times were as follows: 0.002 s (Na, Mg, Al, Si, K, Ca, Mn, Fe, Ni), 0.005 s (Sc, Ti, V, Cr, Nb, Ba, Hf, Th, U), 0.008 s (Sr, Y, Zr, REE, Ta, Pb) and 0.01 s (Li). The total sweep time was 0.297 s. Postacquisition processing was performed using the software Iolite (Woodhead et al. 2007; Hellstrom et al. 2008; Paton et al. 2011), with data reduction and image processing procedures following those outlined in Raimondo et al. (2017). All trace element maps are presented in Data S8.

3.7 | In Situ U-Pb Dating of Zircon

Zircon crystals were separated from 40 kg of two representative vein-free metagabbros belonging to the base of the Rocciavrè gabbroic sequence (see sample location in Figure 1b): one eclogitized Fe-Ti metagabbro (RO1703) and one Mg-Al metagabbro (RO1701), both sampled at the Fonte Neiretto locality (Pognante 1985). Zircon separation was conducted using panning, first in water and then in ethanol, followed by the magnetic extraction of Fe-rich minerals with a Nd magnet. Finally, zircon crystals were handpicked using a binocular microscope.

The zircon grains were cast on 'megamounts', that is, 35-mm epoxy discs fixed on the front of a mount holder, to ensure that no metallic parts nor surface discontinuities faced the secondary ions extraction plate. Megamounts were then polished to expose the centre of zircon crystals. The minerals were carefully studied with an optical microscope (reflected and transmitted light) and SEM (backscattering and cathodoluminescence) prior to SHRIMP analyses.

Zircon crystals were analysed at the CIC-UGR with the IBERSIMS SHRIMP IIe/mc ion microprobe for U-Th-Pb following the method described by Williams and Claesson (1987). The mount was coated with a ~12-nm-thick gold layer. Each spot was rasterized with the primary beam for 120 s prior to analysis and then analysed for six scans following the isotope peak sequence $^{196}Zr_2O$, ^{204}Pb, $^{204.1}$background, ^{206}Pb, ^{207}Pb, ^{208}Pb, ^{238}U, ^{248}ThO and ^{254}UO. Each peak of each scan was measured sequentially 10 times, with the following total counting times per scan: 2 s for mass 196; 5 s for masses 238, 248 and 254; 15 s for masses 204, 206 and 208; and 20 s for mass 207. The primary beam, composed of $^{16}O^{-16}O^{+}$, was set to an intensity of about 5 nA, with two Köhler apertures: (1) at 120 μm and (2) at 70 μm, which generated 17 × 20 and 9 × 12 μm elliptical spots on the target to analyse zircon cores and rims, respectively. The secondary beam exit slit was fixed at 80 μm, achieving a resolution of about 5000 at 1% peak height. All calibration procedures were performed on the standards included on the same mount. Mass calibration was done on the REG zircon (ca. 2.5 Ga, very high U, Th and common lead contents). The analytical session started by measuring the SL13 zircon (Claoué-Long et al. 1995), which was used as a concentration standard (238 ppm U). The TEMORA 1 zircon (416.8 ± 1.1 Ma; Black et al. 2003), used as an isotope ratios standard, was then measured every four unknowns. Data reduction was done with the SHRIMPTOOLS software (available at www.ugr.es/~fbea), which is a new implementation of the PRAWN software originally developed for the SHRIMP. Errors are reported at the 95% confidence interval (~2 σ). Standard errors (95% CI) on the 37 replicates of the TEMORA 1 standard measured during the analytical session were ±0.60% for $^{206}Pb/^{238}U$ and ±0.92% for $^{207}Pb/^{206}Pb$. The full analytical data set is presented in Data S9, and the spot location of analysed zircon crystals is shown in Data S10.

3.8 | In Situ U-Pb Dating of Monazite

Monazite was analysed by laser ablation inductively coupled plasma mass spectrometry (LA-ICP-MS) at the University of British Columbia Okanagan. Monazite found in the omphacite-quartz–rich vein (sample RO2114) was analysed In situ in order to preserve its petrographic context. Samples were ablated using a New Wave Research 193 nm Excimer ArF laser with a TV3 ablation cell, coupled to an Agilent 8900 triple-quadrupole ICP-MS system for U-Th-Pb and trace element measurement. Analyses were conducted at a laser fluence of 2.3 J/cm^2 and a 12 μm spot-size. Two preablation shots were fired offline on the samples to remove surface contamination. The background was measured for ~15 s. The material was then ablated at 6 Hz for ~25 s (with a full mass sweep every 0.3 s). Analyses of unknowns were bracketed (every 11 unknowns) by analyses of matrix-matched monazite reference material 44,069 (424.86 ± 0.36 Ma, TIMS $^{238}U/^{206}Pb$ date; Aleinikoff et al. 2006) for U-Pb geochronology and glass standard NIST SRM 610 (Jochum et al. 2011a) for trace elements. Measured masses were ^{31}P, ^{89}Y, ^{139}La, ^{140}Ce, ^{141}Pr, ^{146}Nd, ^{147}Sm, ^{153}Eu, ^{157}Gd, ^{159}Tb, ^{163}Dy, ^{165}Ho, ^{166}Er, ^{169}Tm, ^{172}Yb, ^{175}Lu, ^{206}Pb, ^{207}Pb, ^{208}Pb, ^{232}Th and ^{238}U.

Secondary U-Pb standards were included in each run as a monitor of accuracy. During the course of this study, we obtained common-Pb corrected (Stacey–Kramers iterative correction in IsoplotR after Stacey and Kramers 1975; Vermeesch 2018) dates of 269.8 ± 1.5 Ma (n = 22) for Trebilcock monazite (~273 Ma; Tomascak, Krogstad, and Walker 1996) and 508.9 ± 2.4 Ma (n = 22) for Stern monazite ('Bananeira', ~512 Ma; Kylander-Clark, Hacker, and Cottle 2013). These dates are accurate to within 1.2% (Trebilcock) and 0.6% (Stern) of the reference values. Internal standardization of trace elements was done on P (assuming 12.89 wt.% of P in monazite). The Iolite plug-in (Paton et al. 2011) for the WaveMetrics Igor Pro Software was used to correct measured isotopic ratios for baselines, time-dependent laser-induced fractionation and instrument drift. Baseline intensities were determined prior to each analysis. Two-sigma uncertainties on isotopic measurements were extracted from Iolite. The error correlation between the $^{238}U/^{206}Pb$ and $^{207}Pb/^{206}Pb$ ratios was recalculated following the method of Schmitz and Schoene (2007). A quadratic uncertainty was added to isotopic ratios to account for analytical uncertainty so that the MSWD of the weighted means of $^{238}U/^{206}Pb$ and $^{207}Pb/^{206}Pb$ equals 1 for secondary matrix-matched reference materials Stern and Trebilcock monazite (Horstwood et al. 2016). This correction adds relative uncertainties on the ratios of 3.8% (for $^{238}U/^{206}Pb$) and 1.2% (for $^{207}Pb/^{206}Pb$). In all calculations, spots with values of trace element composition inconsistent with monazite analyses were not considered in date calculation to avoid the contamination by inclusions or matrix minerals. A common Pb correction was applied to all analyses, following the method used in Soret et al. (2022). Common-Pb-corrected analyses are plotted on a Tera–Wasserburg projection, and the Concordia age is used as implemented in IsoplotR (Vermeesch 2018). The full analytical data set is presented in Data S11, whereas the spot location and textural position of all analysed monazite crystals in sample RO2114 are shown in Data S12.

4 | Petrographic and Structural Observations of Mafic Rocks, Metasediments and High-Pressure Veins

4.1 | Metagabbros of the Rocciavrè Unit

4.1.1 | Mg-Al Metagabbros

Mg-Al metagabbros of the Rocciavrè massif have a coarse-grained porphyroblastic texture with epidote/clinozoisite and albite dominating in the former plagioclase microdomains and omphacite (almost systematically replaced by Ca-Na amphibole) in the former magmatic pyroxene microdomains. Rare paragonite and chlorite are also present and generally associated with the Ca-Na amphibole.

4.1.2 | Fe-Ti Metagabbros

Dykes and sills of Fe-Ti metagabbros crosscutting Rocciavrè Mg-Al metagabbros (Figure 2a) have a fine-grained oriented porphyroclastic and up to mylonitic texture containing a well-preserved eclogite-facies assemblage mostly made of omphacite (~50 vol.%), garnet (~30–40 vol.%), rutile (a few vol.%) and quartz (a few vol.%; Figures 2c,e and 3a,d–j). Subidioblastic garnet crystals are frequently atoll-shaped with either omphacite or Ca-Na blue-green amphibole in their cores (Figure 4a). Oriented rutile crystals generally highlight the main mylonitic foliation (Figure 3a,e), such as in the Monviso massif Fe-Ti metagabbros (Angiboust et al. 2011, 2012b; Locatelli et al. 2018), and contain small phengite. Titanite and ilmenite

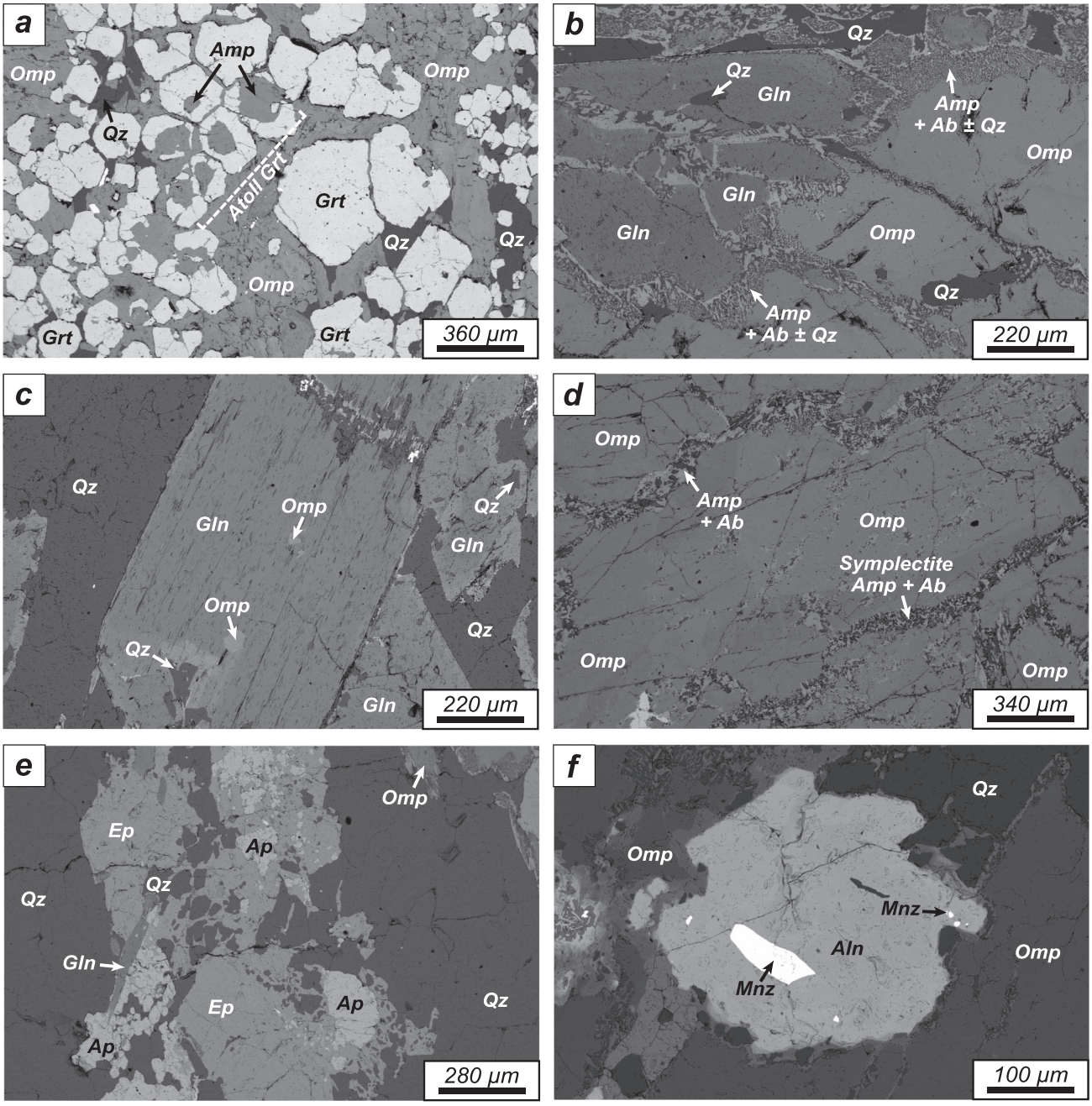

FIGURE 4 | Backscattered electron images of the Rocciavrè high-pressure veins and host Fe-Ti metagabbros. (a) Fe-Ti metagabbro with omphacite, garnet and quartz in textural equilibrium and atoll-shaped garnet filled by Ca-Na blue amphibole (RO2101). (b) Replacement of omphacite by glaucophane in an omphacite-quartz–rich vein. Note the Ca-Na green amphibole + albite ± quartz symplectites growing at crystal boundaries and the quartz inclusions in both omphacite and glaucophane crystals (RO211). (c) Omphacite and quartz inclusions in the glaucophane of glaucophane-quartz–rich veins (RO2116). (d) Ca-Na green amphibole + albite symplectites at the crystal boundaries of an omphacite-rich vein (RO2102). (e) Epidote/clinozoisite-apatite-quartz-glaucophane aggregates in an omphacite-quartz–rich vein (RO2114). (f) Monazite inclusions in an allanite associated with omphacite of an omphacite-quartz–rich vein (RO2114). Abbreviations: Ab: albite; Aln: allanite; Amp: amphibole; Ap: apatite; Ep: epidote/clinozoisite; Gln: glaucophane; Grt: garnet; Mnz: monazite; Omp: omphacite; Qz: quartz.

are observed around rutile. Talc crystals occur at a small modal proportion (less than a few vol.%) and are associated with omphacite. In some samples, whitish layers underlining the foliation are formed by epidote/clinozoisite and paragonite (Data S2) and are classically interpreted as pseudomorphs after lawsonite (e.g., Angiboust and Agard 2010; see also Bonnet et al. 2018). Textural equilibrium observations suggest a peak burial omphacite + garnet + rutile + quartz + talc ± lawsonite paragenesis. Additional accessory minerals include sparse apatite and zircon.

4.2 | Metabasalts of the Orsiera Unit

In the Orsiera tectonic slice, metabasalt and prasinite lenses embedded in the volumetrically dominant metasediments mostly exhibit exhumation-related greenschist-facies parageneses. In the core of some lenses, domains preserved from deformation and retrogression expose a fresh eclogite-facies assemblage (Figure 3b,c). These domains are mostly made of omphacite (~50–60 vol.%), garnet (~20–30 vol.%) and pluri-millimetre large lawsonite pseudomorphs now replaced by clinozoisite and paragonite (~10–20 vol.%). Accessory minerals include apatite and large rutile crystals (a few vol.%). Retrograde blue Na amphibole grows at the expense of euhedral omphacite crystals. At grain boundaries either between several omphacite crystals or between omphacite and garnet crystals, Ca green amphibole + albite symplectites are observed.

4.3 | Metasediments of the Rocciavrè and Orsiera Units

Schistes Lustrés from the Orsiera and Rocciavrè units expose the classical garnet + chloritoid association of index minerals typically observed in eclogite-facies metasediments from the Western Alps (Agard, Jolivet, and Goffe 2001; Bousquet et al. 2008; Herviou et al. 2022). Silica-rich phengite, quartz, carbonates (Ca- or Ca-Mg-Fe–bearing) and graphitic carbonaceous material complete the observed paragenesis. Most of the accessory minerals correspond to rutile crystals.

4.4 | High-Pressure Veins in Rocciavrè Fe-Ti Metagabbros

The presence of eclogite-facies omphacite-bearing veins, comparable with those observed in the Monviso massif (e.g., Philippot 1987; Locatelli et al. 2019), have been previously reported in the Rocciavrè massif (Brenan et al. 1994; Philippot, Agrinier, and Scambelluri 1998), but they have not been described yet. We herein report the occurrence of millimetre- to centimetre-thick omphacite-rich, garnet-rich, quartz-rich and blue-green amphibole-talc veins crosscutting at variable angles the main, gentle, flat-lying foliation visible in the Rocciavrè Fe-Ti metagabbros (Figures 2a–e and 3d–j; see also Data S2). A greater proportion of the quartz-rich veins (associated with garnet, omphacite or blue amphibole) and of the blue-green amphibole-talc veins has been noted in the lower half of the metagabbroic sequence, as displayed on a simplified summary of vein distribution in Figure 2a. In the amphibole-talc veins, fibrous amphibole crystals are characterized by bluish and Ca-Na–bearing cores, whereas the rims are greenish and calcic (Figure 3j; Data S3). No vein thicker than 3 cm was observed during field investigations. Some of the observed quartz-rich vein systems exhibit a previous generation of coarse-grained omphacite covering the walls and are often characterized by broken habits (Figure 2c,e and Data S3). Similarly, garnet has also been observed covering the walls of a vein ultimately filled by quartz (Data S2). Thus, quartz seems to occur as a phase that post-dates pure omphacite and garnet-bearing early vein sets. Widespread quartz inclusions in omphacite from omphacite-quartz–rich veins (Figures 3h and 4b) however suggest that part of the omphacite crystallization occurs synchronously to quartz precipitation. Similarly, quartz inclusions in blue amphibole from blue amphibole-quartz–rich veins suggest co-crystallization of blue amphibole and quartz (Figure 4b,c). In these veins, omphacite inclusions in the core of the same blue amphibole crystals suggest crystallization of amphibole at the expense of omphacite (Figure 4c). Garnet-rich and omphacite-rich vein sets generally have an irregular tortuous structure (Figure 3e–g). The orientation of omphacite crystals perpendicular to the walls in omphacite-rich veins suggests vein formation by Mode I tensile opening (Figure 3d–e). In contrast, quartz-rich veins commonly display a marked plastic deformation, indicated by quartz dynamic recrystallization (subgrain rotations and grain boundary migrations; e.g., Stipp et al. 2002) and by embedded blue-amphibole/omphacite crystals parallelized to the vein walls (Figure 3i and Data S3). Retrogression is marked in omphacite-bearing veins by the replacement of omphacite by blue amphibole and in all veins by the formation along grain boundaries of a symplectitic assemblage mostly made of albite and blue-green Ca-Na amphibole (Figure 4b,d).

In Rocciavrè veins, the accessory phases include spectacular prismatic rutile crystals, which are generally millimetre long and up to pluri-centimetre long, embedded within omphacite-quartz–rich veins (Figures 2d and 3h), as already reported by Brenan et al. (1994). Locally, epidote/clinozoisite together with apatite, quartz and blue amphibole aggregates are observed in two of the studied omphacite-quartz–rich and blue amphibole-quartz–rich veins (Figure 4e; see also sample RO16-01 from Angiboust and Glodny 2020). Several allanite crystals were observed associated with omphacite and quartz in the same omphacite-quartz–rich vein. In this sample (RO2114), monazite crystals occur as inclusions within allanite and omphacite (Figure 4f and Data S12). Zircon has not been observed in the studied set of veins.

5 | Mineral Chemical Compositions

To investigate mineral chemical compositions, different types of samples including Fe-Ti metagabbros and high-pressure veins from the Rocciavrè unit and metabasalts from the Orsiera Unit were selected. Plots of chemical compositions and SEM-EDS chemical maps are displayed in Figures 5a–d and 6a–i, respectively. Representative mineral analyses are presented in Data S4.

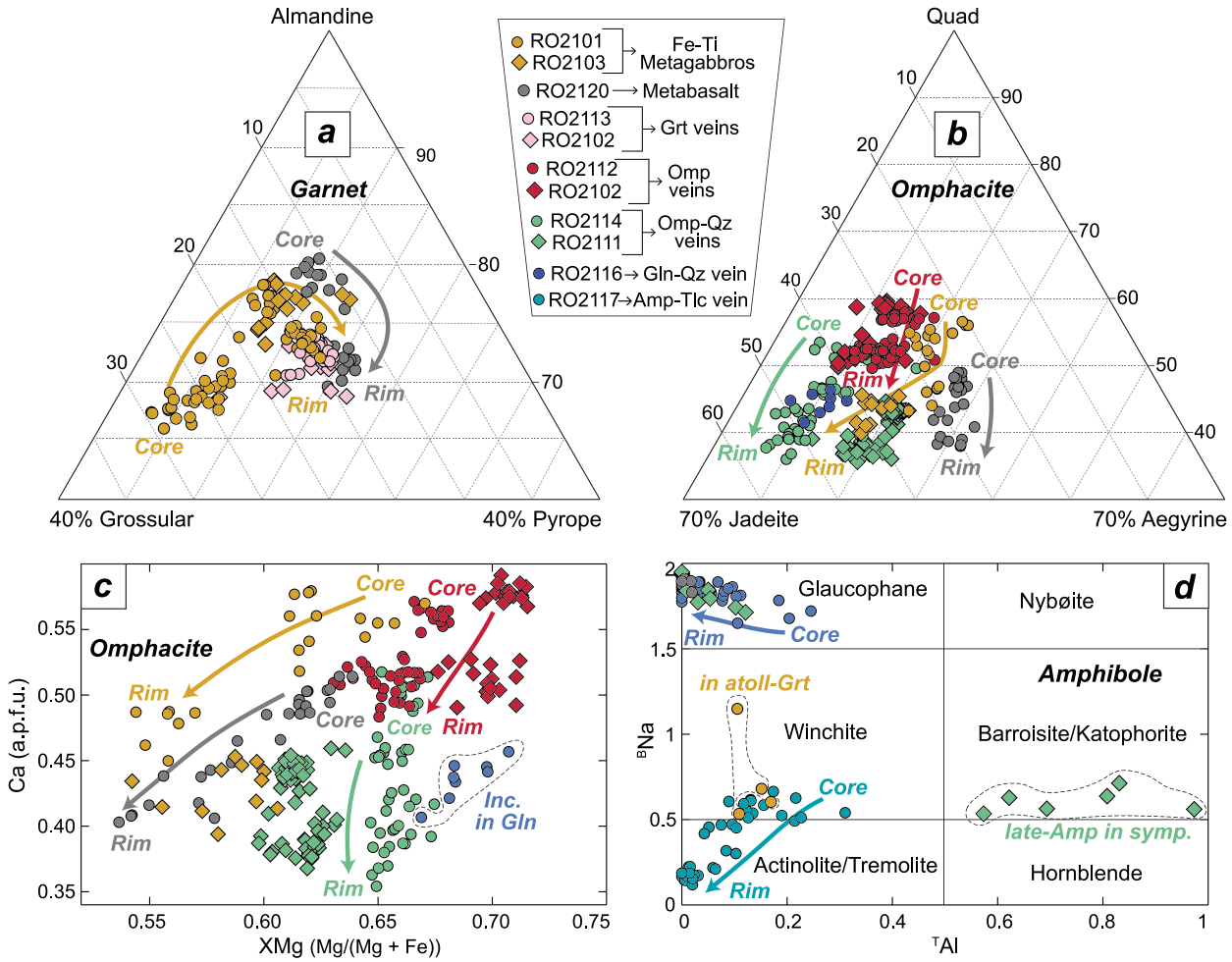

FIGURE 5 | Chemical composition of vein- and host-rock-forming minerals. (a) Ternary diagram of garnet compositions. (b) Ternary diagram of omphacite compositions. (c) Ca versus XMg in omphacite. (d) B-site Na versus T-site Al in amphiboles following Hawthorne et al. (2012) classification. Arrows in al plots correspond to core to rim trends in zoned crystals. Abbreviations: Amp: amphibole; Gln: glaucophane; Grt: garnet; Omp: omphacite; Qz: quartz.

5.1 | Garnet

Garnet crystals from the Fe-Ti metagabbros are zoned with cores richer in Mn and Ca and depleted in Mg and Fe compared with rims (Figures 5a and 6a–b; average core: $Alm_{66}Grs_{24}Prp_6Sps_4$; average rim: $Alm_{74}Grs_{16}Prp_9Sps_1$). In these samples, garnet rims with the highest XMg have pyrope contents ranging between 12% and 14%. In garnet-rich veins, garnet crystals are zoned with cores having a slight enrichment in grossular content and a slight depletion in pyrope content compared to rims (Figures 5a and 6c; average core: $Alm_{68}Grs_{23}Prp_7Sps_2$; average rim: $Alm_{71}Grs_{15}Prp_{13}Sps_1$). Finally, in the Orsiera metabasalts, garnet has rims richer in Mg and Ca, depleted in Mn and slightly depleted in Fe compared with cores (Figures 5a and 6d; average core: $Alm_{71}Grs_{11}Prp_9Sps_9$; average rim: $Alm_{69}Grs_{12}Prp_{14}Sps_5$) with maximum pyrope contents in the range 15%–17%.

5.2 | Omphacite

Omphacite crystals from Fe-Ti metagabbros, metabasalts, omphacite-rich veins and omphacite-quartz–rich veins are all zoned with a general increase in jadeite and aegirine contents from core to rim (Figures 5a and 6e–g). Some omphacite crystals from omphacite-bearing veins and in particular from omphacite-quartz–rich veins display much more complex zoning patterns, in patches (Figure 6h).

5.3 | Amphiboles

In blue amphibole-quartz–rich veins, the analysed amphiboles plot in the glaucophane field and are zoned with core richer in Mg (average XMg = 0.71) compared with rims (average XMg = 0.63; Figures 5d and 6i). Blue amphibole replacing omphacite crystals in omphacite-quartz–rich veins (Figure 4b) and in metabasalts also plot in the glaucophane field (Figure 5d). In the amphibole-talc veins, the bluish Ca-Na cores plot in the winchite field, whereas the green Ca rims plot in the actinolite/tremolite field (Figure 5d). The elevated Fe content of these amphibole cores (Data S4) suggests that they can be classified as actinolite rather than tremolite. Blue amphibole in the core of atoll garnets from Fe-Ti metagabbros also plots in the winchite field, whereas late-amphibole in the symplectites observed at grain boundaries in omphacite-quartz–rich veins plots in the barroisite/katophorite field.

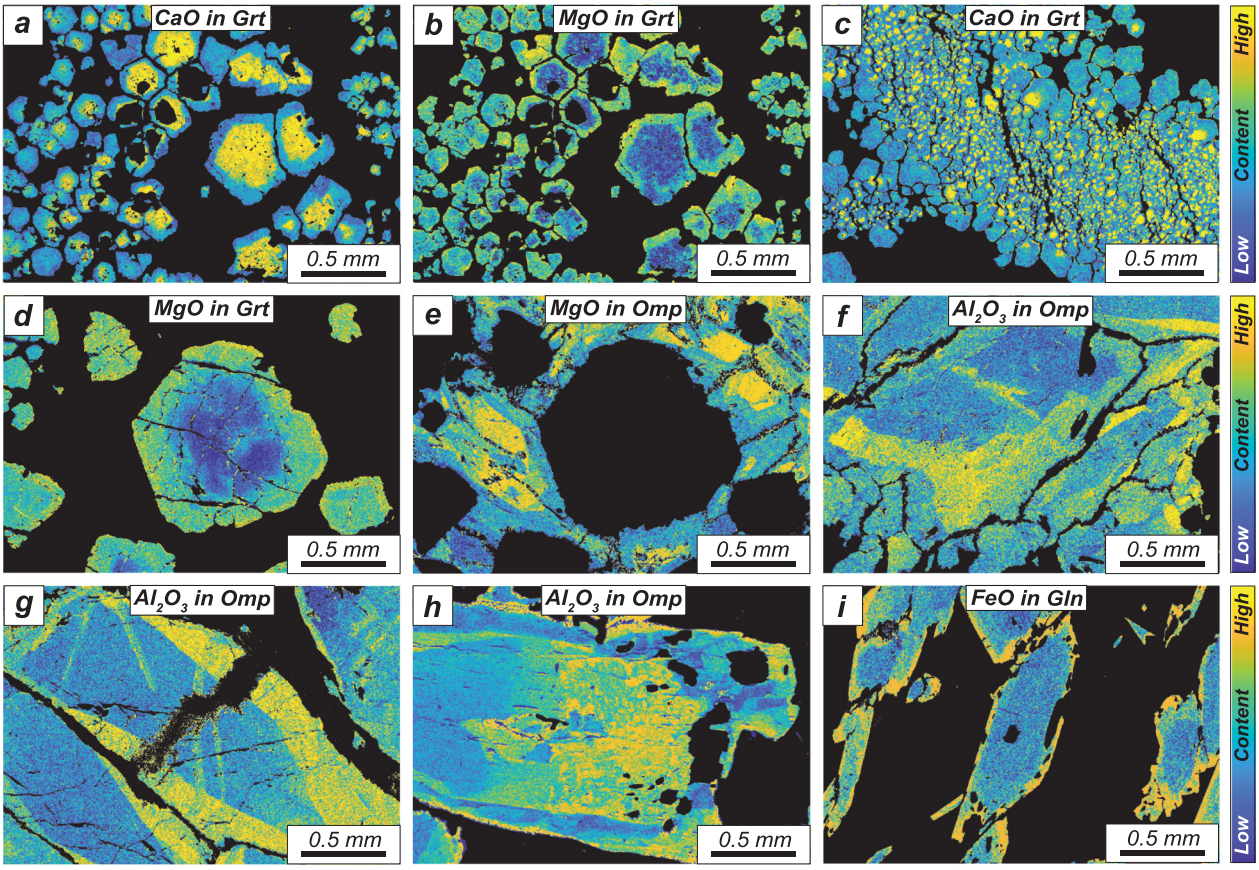

FIGURE 6 | SEM-EDS compositional maps in high-pressure veins and host rocks. (a) and (b) CaO and MgO content of garnet in a Rocciavrè Fe-Ti metagabbro (RO2101). (c) CaO content of garnet in a garnet-rich vein (RO2113). (d) MgO content of garnet in an Orsiera metabasalt (RO2120). (e) MgO content of garnet in an Orsiera metabasalt (RO2120). (f) Al_2O_3 content of omphacite in an omphacite-rich vein (RO2112). (g) and (h) Al_2O_3 content of omphacite in two omphacite-quartz–rich vein (RO2111 and RO2114, respectively). FeO content of glaucophane in a glaucophane-quartz–rich vein (RO2116). Abbreviations: Gln: glaucophane; Grt: garnet; Omp: omphacite.

5.4 | Phengite

Phengite crystals spatially associated with rutile crystals in Fe-Ti metagabbros are silica-rich highlighting important Tschermak substitution. The most substituted phengite analyses have a Si a.p.f.u. range of 3.67–3.73 for structural formulas calculated on an 11-oxygen basis.

5.5 | Epidote/Clinozoisite

Epidote/clinozoisite from omphacite-quartz–rich veins have an average XEpidote of 0.61.

5.6 | Talc

Talc from Fe-Ti metagabbros have an average XMg of 0.85, whereas talc from amphibole-talc veins have an average XMg of 0.87.

5.7 | Monazite

Monazite crystals always correspond to Ce-Monazite and are homogeneous in composition (Data S5).

6 | Thermobarometric Estimations

6.1 | Raman Spectroscopy on Carbonaceous Material

Temperatures of 509°C and 549°C were obtained by RSCM in the two samples from the Rocciavrè unit (Table 1 and Figure 1b). For the Orsiera unit, estimated temperatures lie between 511°C and 553°C (Table 1) and are in the same range as those previously estimated in the same unit, using the same methodology (503°C–542°C; Figure 1b; Beyssac et al. 2002; Gabalda et al. 2009; Herviou et al. 2022).

6.2 | Thermodynamic Modelling

6.2.1 | Rocciavrè Fe-Ti Metagabbro

For the selected sample RO2101 and in the range 1.5–3.0 GPa/400°C–650°C, two pseudosection fields reproduce the mineral assemblages globally observed in Rocciavrè Fe-Ti metagabbros: garnet-omphacite-lawsonite-rutile-talc-quartz-phengite and garnet-omphacite-rutile-talc-quartz-phengite (Figure 7a). Considering that the RO2101 sample is devoid of lawsonite relicts, the second field with no lawsonite was selected.

TABLE 1 | Raman spectroscopy on carbonaceous material temperatures.

Sample	Unit	*n* spectra	Mean T°C	SD	SE	mean R^2	R^2 ratio	SD R^2 ratio
RO1001	Rocciavrè	11	549	11	3	0.99	0.21	0.02
RO2109	Rocciavrè	15	509	20	5	0.98	0.30	0.05
FIN1901	Orsiera	16	553	47	12	0.97	0.20	0.11
RO2121	Orsiera	14	522	29	8	0.97	0.27	0.06
RO2122	Orsiera	15	511	15	4	0.98	0.29	0.03

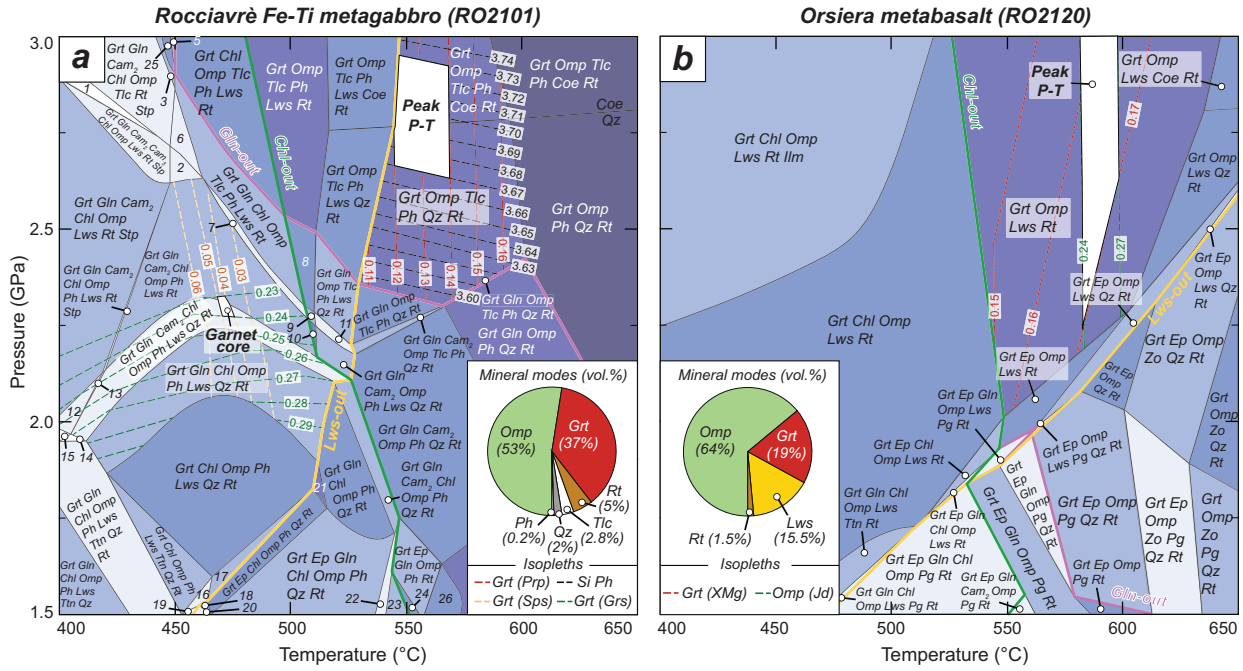

FIGURE 7 | Pressure–temperature (P–T) estimations for Rocciavrè and Orsiera eclogites. (a) P–T pseudosection for a Fe-Ti metagabbro of the Rocciavrè unit (RO2101) for a bulk composition of (in wt.% oxide) SiO_2 (45.30); Al_2O_3 (11.80); FeO (14.90); Fe_2O_3 (4.14); MnO (0.31); MgO (5.56); CaO (9.52); K_2O (0.02); Na_2O (3.19); TiO_2 (5.61); H_2O (in excess). (b) P–T pseudosection for a metabasalt of the Orsiera unit (RO2120) for a bulk composition of (in wt.% oxide) SiO_2 (48.50); Al_2O_3 (15.35); FeO (7.40); Fe_2O_3 (3.53); MnO (0.18); MgO (4.29); CaO (11.90); Na_2O (5.26); TiO_2 (1.68); H_2O (in excess). For both pseudosections, major dehydration reactions are represented by colour lines, isopleths by dashed lines and mineral modal proportions (in vol.%) by pie charts. Mineral assemblages in (a) 1: Grt Gln Cam_2 Cam_3 Chl Omp Tlc Lws Rt Stp; 2: Grt Gln Cam_2 Cam_3 Chl Omp Ph Lws Rt; 3: Grt Gln Chl Omp Tlc Lws Rt Stp; 4: Grt Chl Omp Tlc Lws Rt Stp; 5: Grt Gln Chl Omp Tlc Ph Lws Rt Stp; 6: Grt Gln Cam_2 Cam_3 Chl Omp Tlc Ph Lws Rt; 7: Grt Gln Cam_2 Chl Omp Tlc Ph Lws Rt; 8: Grt Gln Omp Tlc Ph Lws Rt; 9: Grt Gln Cam_2 Omp Tlc Ph Lws Rt; 10: Grt Gln Cam_2 Omp Ph Lws Rt; 11: Grt Gln Cam_2 Omp Tlc Ph Lws Qz Rt; 12: Grt Gln Cam_2 Chl Omp Lws Qz Rt Stp; 13: Grt Gln Cam_2 Chl Omp Ph Lws Qz Rt Stp; 14: Grt Gln Cam_2 Chl Omp Ph Lws Ttn Qz Rt; 15: Grt Gln Cam_2 Chl Omp Lws Ttn Qz Rt Stp; 16: Grt Ep Chl Omp Ph Lws Ttn Qz Rt; 17: Grt Ep Chl Omp Ph Lws Qz Rt; 18: Grt Ep Chl Omp Ph Ttn Qz Rt; 19: Grt Ep Gln Chl Omp Ph Lws Ttn Qz Rt; 20: Grt Ep Gln Chl Omp Ph Ttn Qz Rt; 21: Grt Chl Omp Ph Qz Rt; 22: Grt Ep Gln Cam_2 Chl Omp Ph Qz Rt; 23: Grt Ep Gln Cam_2 Chl Omp Ph Rt; 24: Grt Ep Gln Cam_2 Omp Ph Rt; 25: Grt Gln Chl Omp Tlc Ph Lws Rt Stp; 26: Grt Ep Gln Omp Ph Qz Rt. Abbreviations: Cam: clinoamphibole; Chl: chlorite; Coe: coesite; Ep: epidote/clinozoisite; Gln: glaucophane; Grt: garnet; Ilm: ilmenite; Lws: lawsonite; Omp: omphacite; Pg: paragonite; Ph: phengite; Qz: quartz; Rt: rutile; Stp: stilpnomelane; Tlc: talc; Ttn: titanite Zo: zoisite.

The best-fit box constraining the peak P–T conditions was determined by using the range of pyrope content for the Mg-richest garnet rims (XPrp = 0.12–0.14) and the range of silica content for the most substituted phengite (Si = 3.67–3.73 a.p.f.u.) and by plotting the corresponding isopleths (Figure 7a). In the obtained P–T field, the estimated modal phase proportions of omphacite (53 vol.%), garnet (37 vol.%), rutile (5 vol.%), talc (2.8 vol.%), quartz (2 vol.%) and phengite (0.2 vol.%) are consistent with the observations made in the sample despite a slight overestimation of the talc proportion. The estimated P–T conditions of 2.6–2.9 GPa and ~545°C–570°C fits within the range of temperature estimated by RSCM (509°C–549°C with an uncertainty of ±50°C; Beyssac et al. 2002; Table 1) and extends at pressure higher than the quartz–coesite transition (Figure 7a). Although coesite crystals have not been observed in the studied samples, growing evidence of coesite occurrences in analogous LPL units (Lago di Cignana: Reinecke 1991, 1998; Groppo, Beltrando, and Compagnoni 2009; Monviso: Ghignone et al. 2023; Susa valley: Ghignone et al. 2024) suggest that the initial presence of coesite, now transformed back into quartz, should not be ruled out. Using grossular and spessartine content isopleths, the prograde growth of the Mn-Ca–rich garnet cores is estimated at ~480°C/2.3 GPa (Figure 7a).

6.2.2 | Orsiera Metabasalt

For the Orsiera metabasalt pseudosection, the garnet-omphacite-lawsonite-rutile assemblage observed in the RO2120 sample is reproduced over a large P–T field at around 2–3 GPa and 530°C–640°C. With no phengite, the studied sample lacks good pressure-dependent isopleths for estimating relatively precise P–T fields. The intersection between the maximum pyrope content isopleths in garnet rims and the range of XMg and jadeitite content in omphacite cores give a best-fit box broadly estimated at 2.2–3.0 GPa and 575°C–590°C. This range fits our RSCM temperature estimates in the same unit (511°C–553°C ± 50°C; Table 1). In this P–T field, the estimated mineral modal proportions are consistent with those observed in the sample: omphacite (64 vol.%), garnet (19 vol.%), lawsonite (15.5 vol.%) and rutile (1.5 vol.%).

7 | Fluid Inclusion Petrography and Chemistry

7.1 | Petrographic Observations of Fluid Inclusions

FIs were characterized in 11 selected samples including one host Fe-Ti metagabbro, one garnet-rich vein, two omphacite-rich veins, four omphacite-quartz–rich veins, one glaucophane-quartz–rich vein, one winchite-actinolite-talc vein and one Orsiera metabasalt. The 265 studied inclusions are hosted in omphacite (veins, host Fe-Ti metagabbro, metabasalt), garnet (veins, metabasalt), glaucophane (vein) and winchite-actinolite (vein) crystals.

In omphacite crystals from omphacite-rich veins, omphacite-quartz–rich veins and the host Fe-Ti metagabbro, FIs are aqueous, tubular-shaped, typically 5–20 μm long and up to 35–40 μm long (Figure 8a,b). They occur isolated or in clusters and are always oriented parallel to the c-axis of omphacite, suggesting their primary entrapment. Most inclusions are two-phase containing a liquid and a vapour bubble, but several three-phase inclusions with a single transparent anisotropic crystal were observed in omphacite-rich veins and omphacite-quartz–rich veins (Figure 8a,b). The vapour bubble generally occupies ~10%–20% of the total inclusion volume.

Primary FIs in garnet from garnet-rich veins and from the metabasalt occur either isolated or in small inclusion clusters, have a slightly elongated shape with a typical size of 5–20 μm long and are aqueous (Figure 8c,d). Most of these inclusions are two-phase (liquid + vapour) with only one three-phase inclusion (liquid + vapour + solid) containing a single transparent anisotropic crystal observed in a garnet-rich vein. The vapour bubble is large, occupying ~20%–30% of the total volume (Figure 8c,d).

In the glaucophane and winchite-actinolite crystals, respectively from the glaucophane-quartz–rich and winchite-actinolite-talc veins, FIs are aqueous, tubular-shaped and typically 5–15 μm long (Figure 8e,f). These inclusions occur isolated or in small clusters and are always oriented parallel to the c-axis of amphibole crystals suggesting their primary entrapment (Figure 8e,f). All observed inclusions are two-phase (liquid + vapour) with vapour bubbles generally occupying ~10% of the total inclusion volume.

7.2 | Fluid Inclusion Gas Content

A strong N_2 signal (peak at 2331 cm^{-1}) was detected in most analysed inclusion bubbles (Figure 9a) except for garnet from

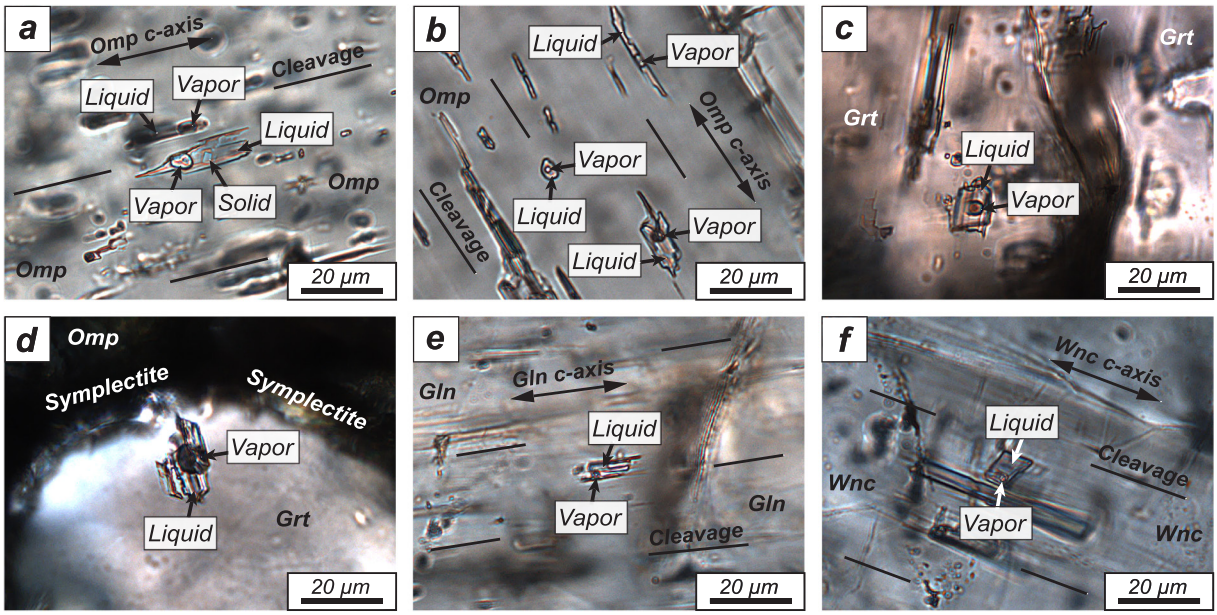

FIGURE 8 | Microphotographs of primary fluid inclusions. (a) and (b) Two-phase (liquid + vapour) and three-phase (liquid + vapour + solid) tubular fluid inclusions oriented parallel to the omphacite c-axis in omphacite-quartz–rich vein (RO2114, RO2111). (c) Two-phase fluid inclusion hosted in a garnet crystal from an Orsiera eclogitic metabasalt (RO2120). (d) Isolated two-phase fluid inclusion in a garnet from a garnet-rich vein (RO2102). (e) Two-phase fluid inclusion oriented parallel to the glaucophane c-axis in a glaucophane-quartz–rich vein (RO2116). (f) Two-phase fluid inclusion oriented parallel to the winchite c-axis in a winchite-actinolite-talc vein (RO2117). Abbreviations: Gln: glaucophane; Grt: garnet; Omp: omphacite; Wnc: winchite.

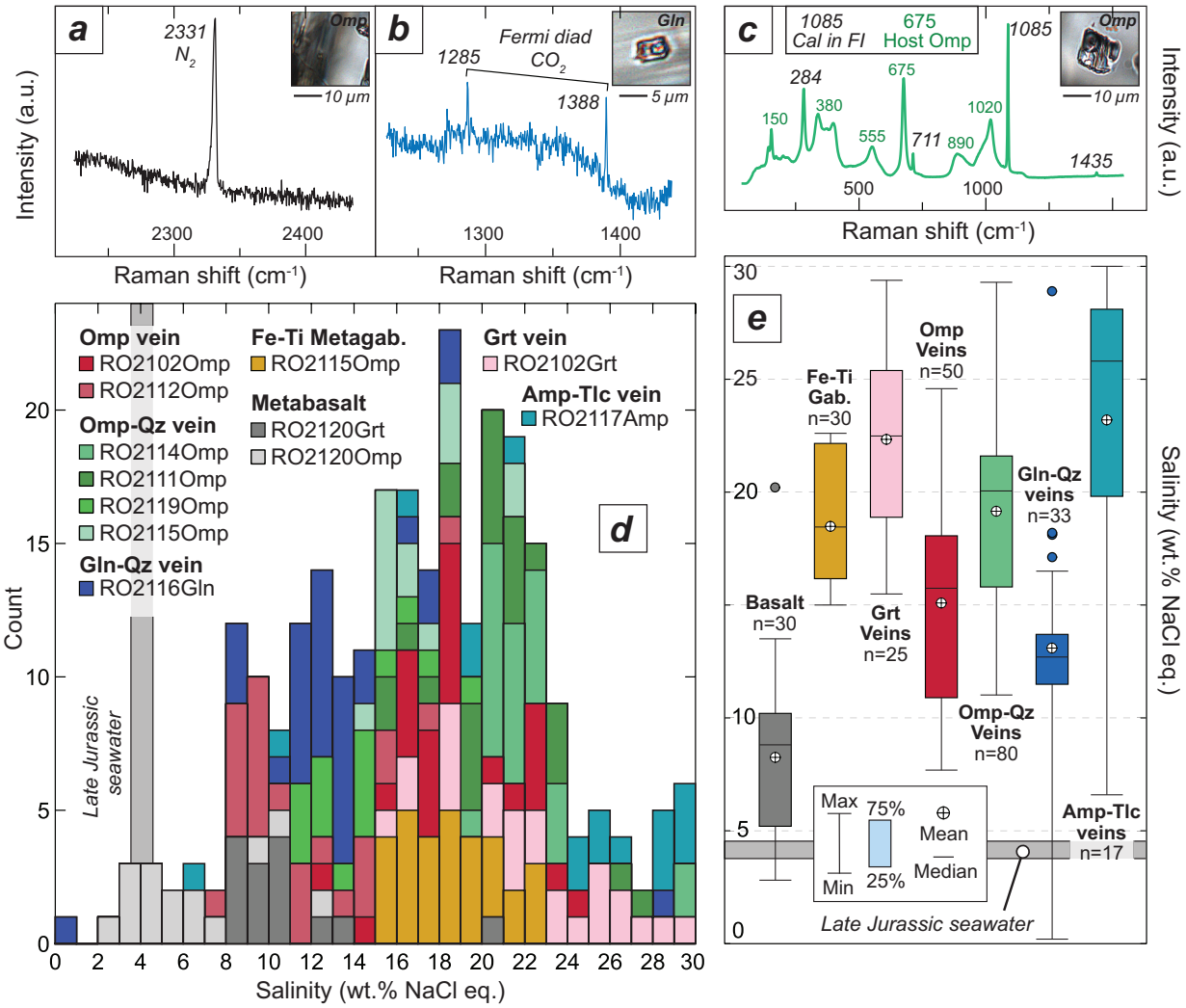

FIGURE 9 | Chemistry of primary fluid inclusions (FI). (a) and (b) Raman gas spectra in vapour bubbles of fluid inclusions: N_2 in an omphacite-hosted inclusion from an omphacite-rich vein (RO2112) and CO_2 in a glaucophane-hosted inclusion from a glaucophane-quartz–rich vein (RO2116), respectively. (c) Raman spectra of a calcite crystal in a fluid inclusion overprinting the signal of the host omphacite; omphacite-rich vein (RO2112). (d) Histogram of estimated fluid inclusion salinity for all analysed samples. The Late Jurassic seawater salinity is after Hay et al. (2006). Box plots of estimated fluid inclusion salinity grouped by sample type. Abbreviations: Amp: amphibole; Cal: calcite; Gab.: gabbro; Gln: glaucophane; Grt: garnet; Omp: omphacite; Qz: quartz; Tlc: talc.

garnet-rich veins where the small size of the inclusions (~5 µm) prevented good gas analyses. Gas analyses were also challenging in the small winchite-actinolite FIs, and N_2 was detected in only one inclusion of this vein type. The Fermi diad of CO_2 (peaks at 1285 and 1388 cm^{-1}) was detected in two N_2-bearing FIs hosted in garnet crystals from the Orsiera metabasalt. Finally, CO_2 and CH_4 (peak at 2917 cm^{-1}) peaks were simultaneously observed in two inclusions from the glaucophane-quartz–rich vein where no N_2 was detected (Figure 9b and Data S7).

7.3 | Solids in Fluid Inclusions

With peaks at 284, 711 and 1085 cm^{-1} overprinting the host signal, all solids observed in three-phase inclusions from omphacite in the veins and the one solid observed in a garnet-rich vein were identified as calcite crystals (Figure 9c; e.g., Frezzotti, Tecce, and Casagli 2012). No OH-bearing step-daughter mineral was observed. When present, these minerals, which are formed by the interaction between host minerals and trapped fluid, can affect the initial salinity of the fluid (e.g., Frezzotti and Ferrando 2015).

7.4 | Fluid Inclusion Salinity

The estimated salinity of the 265 characterized FIs is displayed by a sample in the histogram of Figure 9d and by sample type in the box plots of Figure 9e. The mean, median and standard deviation of the estimated salinity, as well as the number of studied FI types by sample and by type of sample, are displayed in Table 2.

High salinity values are generally estimated for FIs in (mean; median; sd; in wt.% NaCl eq. and FI numbers): the host Fe-Ti metagabbros (18.5 wt.%; 18.5 wt.%; 2.2; $n = 30$), the garnet-rich veins (22.4 wt.%; 22.5 wt.%; 3.9; $n = 25$), the omphacite-rich veins (15.1 wt.%; 15.7 wt.%; 4.7 $n = 50$) and the omphacite-quartz–rich veins (19.2 wt.%; 20.0 wt.%; 3.9; $n = 33$). Winchite-actinolite-talc

TABLE 2 | Summary of primary fluid inclusion (FI) chemistry.

Sample type	Sample	Unit	Host mineral	Detected fluid species	Mean salinity (wt.% NaCl eq.)	Median salinity (wt.% NaCl eq.)	SD salinity	*n* FI
Fe-Ti metagabbros	RO2115	Rocciavrè	Omphacite	Aq-N_2	18.5	18.5	2.2	30
Garnet-rich veins	RO2102	"	Garnet	Aq	22.4	22.5	3.9	25
Omphacite-rich veins	RO2102	"	Omphacite	Aq-N_2	18.7	18.0	2.9	25
"	RO2112	"	"	"	11.5	10.7	3.1	25
"	All omphacite-rich veins	"	"	"	15.1	15.7	4.7	50
Omphacite-quartz–rich veins	RO2114	"	"	"	22.2	21.6	2.4	25
"	RO2111	"	"	"	20.6	20.2	2.9	25
"	RO2119	"	"	"	14.0	14.2	2.4	15
"	RO2115	"	"	"	17.1	16.7	2.2	15
"	All omphacite-quartz–rich veins	"	"	"	19.2	20.0	3.9	80
Glaucophane-quartz–rich veins	RO2116	"	Glaucophane	Aq-N_2-CO_2-CH_4	13.1	12.7	4.3	33
Winchite-tremolite-talc veins	RO2117	"	Winchite-tremolite	Aq-N_2	23.2	25.8	6.8	17
Metabasalt	RO2120	Orsiera	Omphacite + garnet	Aq-N_2-CO_2	8.3	8.8	3.8	30

Abbreviation: Aq: aqueous fluid.

veins have the highest FI salinity (23.2 wt.%; 25.8 wt.%; 6.8; $n = 17$), whereas glaucophane-quartz–rich veins have more intermediate salinity values (13.1 wt.%; 12.7 wt.%; 4.3; $n = 33$). Among all samples, the metabasalts have the lowest values (8.3 wt.%; 8.8 wt.%; 3.8; $n = 30$) with garnet-hosted inclusions generally having a more saline fluid than omphacite-hosted FIs (Figure 9d). All samples have salinity values much higher than those estimated for Late Jurassic seawater (~3.7–4.2 wt.%; Hay et al. 2006; Figure 9d,e).

8 | Trace Element Mapping

LA-ICP-MS trace element maps were acquired from an omphacite-quartz–rich vein (RO1801). Selected maps are presented in Figure 10, and maps for all collected elements are displayed in Data S8. A mineral index map obtained after examining the relative abundance of major elements and creating a mask for each mineral phase is also provided in Figure 10.

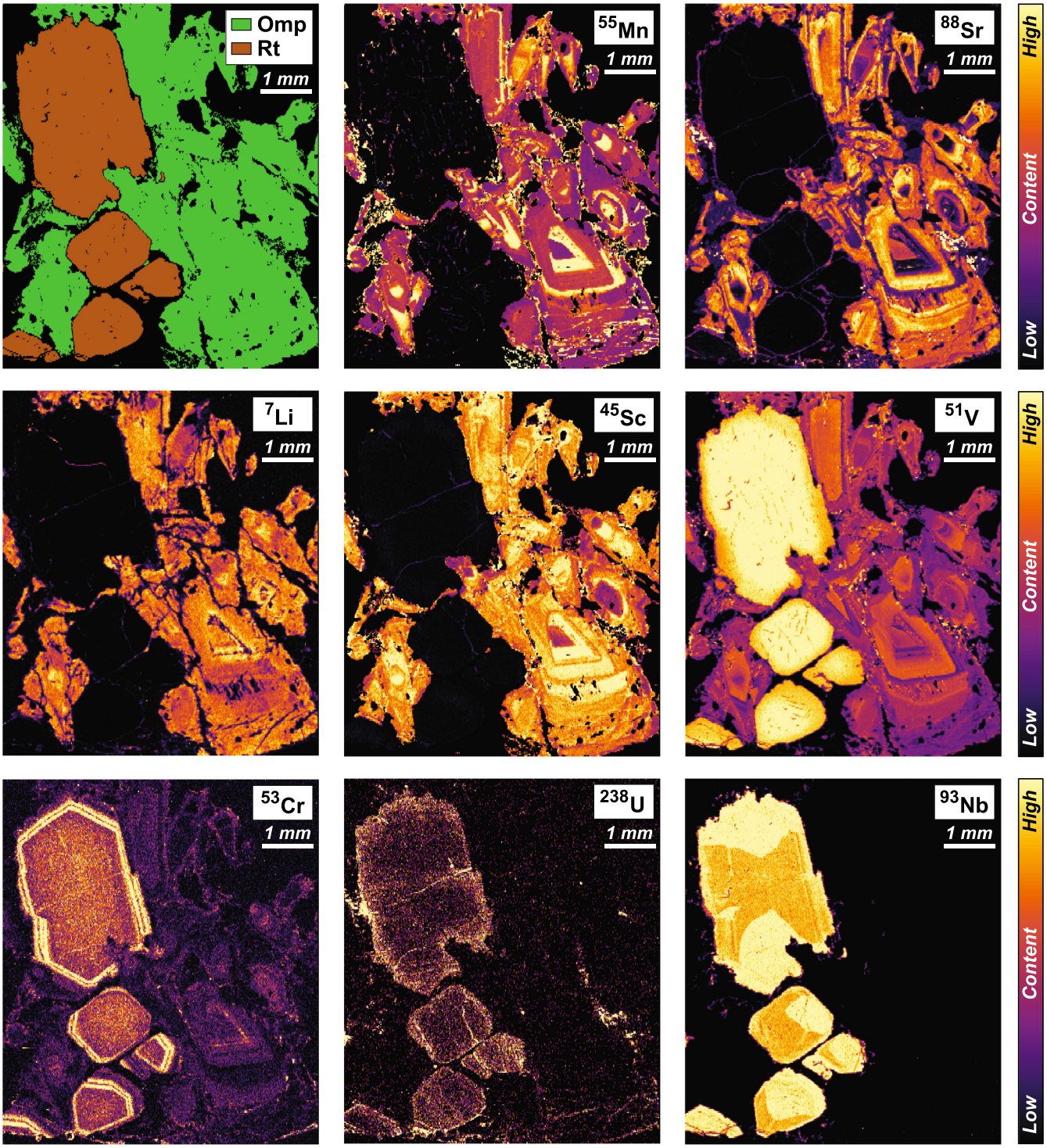

FIGURE 10 | LA-ICP-MS trace element maps in rutile and omphacite of an omphacite-quartz–rich vein. The distinction between rutile and omphacite crystals is shown on the first panel. Abbreviations: Omp: omphacite; Rt: rutile. A compilation of all trace element maps acquired is provided in Data S8.

Omphacite crystals mostly show oscillatory zoning patterns associated with some sector zoning in Mn, Sr, Li, Sc, V, Cr, Ni and the middle to heavy REE (Sm, Eu, Gd, Tb, Dy, Ho, Er, Tm, Yb, Lu). A thin rim exhibiting oscillatory enrichments in Cr, enriched in U and depleted in V compared with cores is observed in rutile crystals. Hourglass zoning is also observed in rutile for some HFSE (Nb, Ta, Zr).

Enrichments in some elements observed at grain boundaries are interpreted as smearing artefacts exaggerating the size of small inclusions (e.g., Raimondo et al. 2017; Hyppolito et al. 2019).

9 | In Situ U-Pb Dating of Zircon

9.1 | Fe-Ti Metagabbro

The studied Fe-Ti metagabbro (RO1703) contains abundant zircons. These crystals are translucent with a whitish colour, stubby, euhedral and equant to elongated bipyramidal prisms, although the main grains show broken morphologies resulting from sample preparation, with sizes ranging from 400 μm × 250 μm to 100 μm × 50 μm (Figure 11a). Cathodoluminescence images reveal different internal morphologies: some grains having a fine magmatic oscillatory zoning, some having a patchy zoning pattern and some having unzoned grains (Figure 11a). Thirty-seven U-Th-Pb measurements on 37 different zircon yielded variable concentrations of U (28–2495 ppm) and Th (5–2009 ppm) with Th/U ratios ranging between 0.13 and 1.18 and have a common lead contribution (f206 = 0.04%–34.99%; Data S9). Some analyses were discordant (discordance of −0.2%–50.08%; Data S9). We therefore applied a ^{208}Pb-based correction algorithm (Ludwig 2009 that corrected the majority of data to Concordia. The 24 concordant data (^{208}Pb-corrected discordance of −8–9.8) give a weighted mean (errors reported at 2 σ) of the 208-corrected ^{206}Pb/^{238}U age of 151 ± 4 Ma (MSWD = 6.29) virtually identical to ^{207}Pb-corrected age of 150 ± 4 Ma (MSWD = 5.16; Figure 11a).

9.2 | Mg-Al Metagabbro

The Mg-Al metagabbro sample (RO1701) contains few zircons, and only 12 grains were collected after the separation process. Grains are colourless, free of inclusions, euhedral short bipyramidal prisms with dimensions ranging from 200 μm × 100 μm to 100 μm × 50 μm (Figure 11b). Under the cathodoluminescence microscope, they show a sector to concentric oscillatory zoning with high cathodoluminescent bands and darker ones (Figure 11b). Thirteen measurements in 12 grains have low U (9–180 ppm) and Th (4–417 ppm) with Th/U ratio of 0.4–2.38 (Data S9). These zircon crystals have a common lead contribution (f206 = 0.3%–8.5%) and yield large discordant values (discordance of 5.6%–49%). They are however aligned in a Discordia line providing a lower intersection age of 150 ± 6 Ma (MSWD = 1.68; Data S9). We applied the ^{208}Pb-based correction and seven concordant data (discordance of −6.4%–10%) yield same age within error with a 208-corrected ^{206}Pb/^{238}U age of 158 ± 4 Ma (MSWD = 1.15) virtually identical to ^{207}Pb-corrected age of 158 ± 4 Ma (MSWD = 0.93; Figure 11b).

10 | In Situ U-Pb Dating of Monazite

U-Pb in monazite crystals from the omphacite-quartz–rich vein RO2114 (Figure 12) gave a well-constrained isochron of 40.4 ± 0.2 Ma (n = 91). All monazite crystals have a similar REE pattern suggesting that they belong to a unique generation (Figure 12), such as supported by their homogeneous composition (Data S5).

11 | Discussion

11.1 | The Rocciavrè Massif: A True Analogue of the Monviso Lago Superiore Unit?

Estimated RSCM temperature in the range 509°C–549°C for the Rocciavrè unit and 511°C–553°C for Orsiera (Table 1) are fitting those previously estimated in the literature for Orsiera

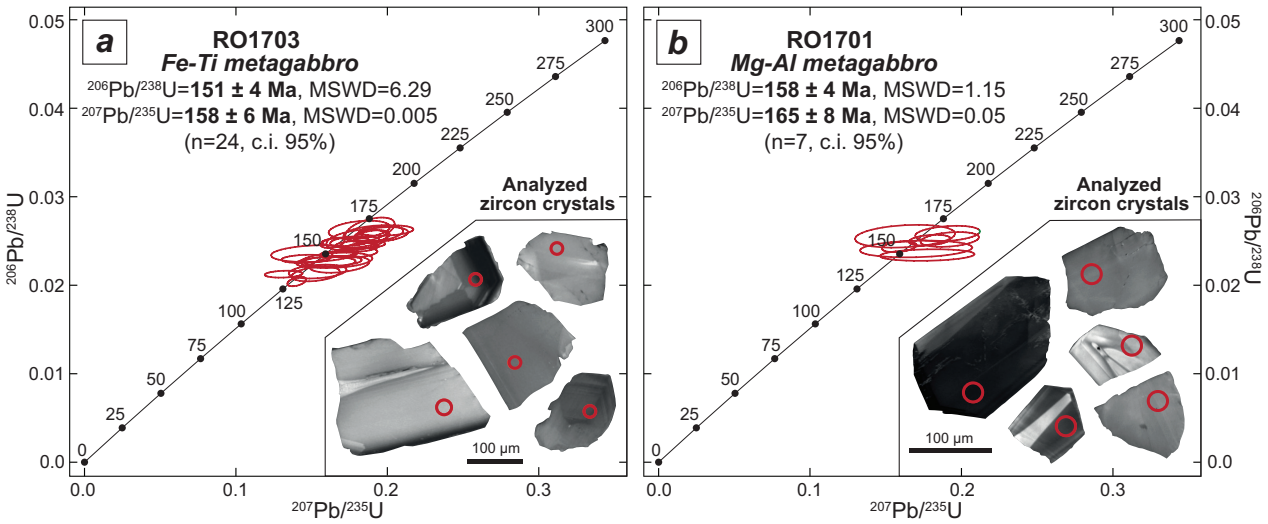

FIGURE 11 | Wetherill Concordia U-Pb plots with ^{208}Pb-corrected for zircon crystals of (a) a Fe-Ti metagabbro (RO1703) and a Mg-Al metagabbro (RO1701).

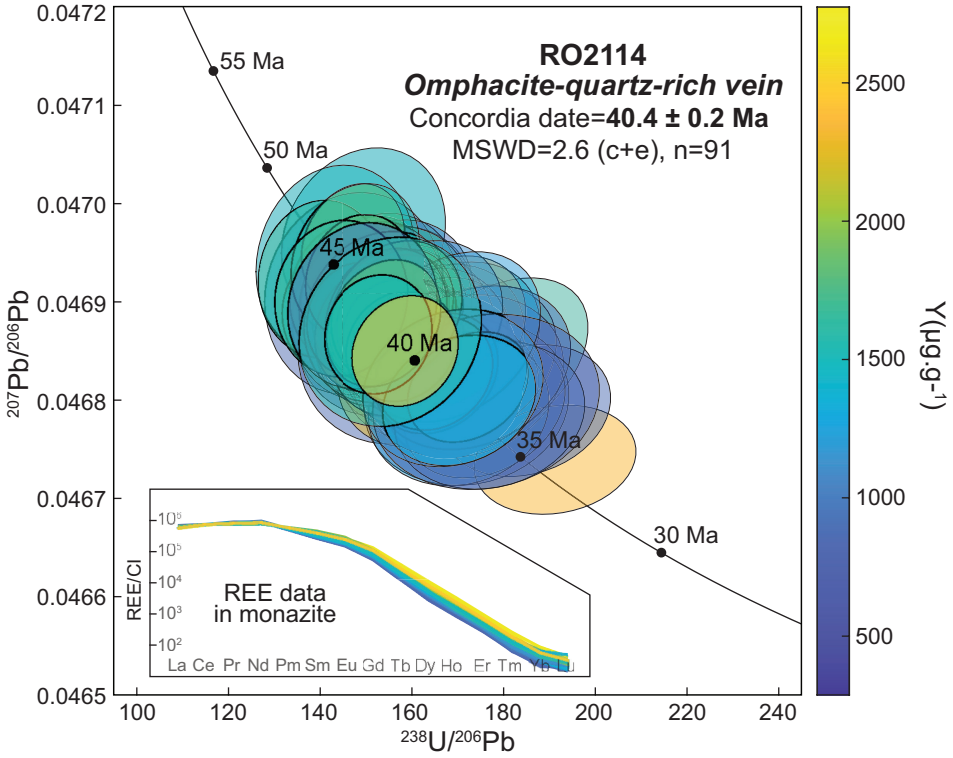

FIGURE 12 | Tera–Wasserburg Concordia U-Pb plot and trace element pattern in monazite crystals of an omphacite-quartz–rich vein. The colour scale ranging from dark blue to yellow corresponds to Y concentration in monazite.

metasediments (503°C–542°C; Beyssac et al. 2002; Gabalda et al. 2009; Herviou et al. 2022) and are consistent with the peak P–T conditions that we estimated independently in mafic rocks using thermodynamic modelling (~545°C–570°C/2.6–2.9 GPa for Rocciavrè and 575°C–590°C/2.2–3.0 GPa for Orsiera). No metamorphic gradient through the units such as observed in the blueschist-facies LPU and LPM units (Herviou et al. 2022) is detected, and no metamorphic gap is observed between the two studied LPL slices, having relatively consistent peak P–T estimations. However, although an absence of a temperature gap is likely considering the same range of RSCM temperature, a potential peak pressure gap between the two units may have been undetected because of the poorly constrained pressure estimates in the Orsiera metabasalt (Figure 7b). These peak P–T conditions are significantly higher than those previously estimated for Rocciavrè (~450°C–500°C/> 1.2–1.4 GPa; e.g., Pognante and Kienast 1987) and Orsiera eclogites (400°C–500°C/> 1.2 GPa; Bouffette and Caron 1991) but are in a range closer to previous estimates for Orsiera metasediments (~500°C–540°C/2.2–2.5 GPa; Agard, Jolivet, and Goffe 2001; Herviou et al. 2022).

These new estimates fit well the peak P–T conditions estimated for LPL units exposed south and north of the studied area, such as the Lago Superiore unit of the Monviso massif (~550°C–580°C, 2.6–2.8 GPa; Groppo and Castelli 2010; Angiboust et al. 2012b; Locatelli et al. 2018) and the eclogites of the Savoy-Susa region (~500°C–550°C, 2.3–2.9 GPa; Plunder et al. 2012; Ghignone et al. 2021a, 2024; Herviou et al. 2022). In both of latter examples, thermobarometric estimates initially predicted a potential peak burial at conditions close to the quartz–coesite transition (Angiboust et al. 2012b; Locatelli et al. 2018; Ghignone et al. 2021a) later confirmed by the observation of coesite in the Monviso massif (Ghignone et al. 2023) and in the Susa valley (Ghignone et al. 2024). Whereas coesite crystals have not been observed in our samples, peak P–T conditions estimated by thermodynamic modelling overlap both the quartz and coesite stability fields (Figure 7a,b), suggesting that coesite may have occurred in Rocciavrè and Orsiera units at peak burial. In addition, the presence of lawsonite pseudomorphs in Orsiera eclogitic metabasalts and in some Rocciavrè eclogites suggest a peak burial within or close to the lawsonite-eclogite-facies such as suggested in other LPL units (Lago Superiore: Groppo and Castelli 2010; Angiboust et al. 2011, 2012b; Zermatt-Saas Angiboust and Agard 2010).

In the Monviso eclogites from the Lago Superiore unit, zircon cores suggest the crystallization of Fe-Ti gabbros during the Late Jurassic (ca. 163 Ma), whereas their rims suggest a peak burial at ca. 50–45 Ma (Rubatto and Hermann 2003; Rubatto and Angiboust 2015; Garber et al. 2020). In the Rocciavrè massif, our zircon U-Pb analyses in Mg-Al and Fe-Ti gabbros give ages of 158 ± 4 Ma and 151 ± 4 Ma, respectively (Figure 11a–b; note that the age for the Fe-Ti gabbro is more reliable that the Mg-Al one thanks to (1) the larger number of analyses and (2) a smaller effect of the common Pb correction), suggesting a synchronous formation of oceanic crust in both units. These new ages globally fit the global range of U-Pb ages in magmatic zircon from Alpine mafic rocks (ca. 170–150 Ma; e.g., Manatschal and Müntener 2009; Li et al. 2013). The Fe-Ti metagabbro age is slightly younger than the peak of magmatic accretion estimated for the Liguro-Piemont domain (ca. 165–160 Ma) but fits recently collected U-Pb zircon ages in the nearby Susa and Lanzo valleys (De Togni et al. 2024). Although no metamorphic rims were observed around Rocciavrè zircon

crystals, a phengite-glaucophane-epidote-apatite Rb-Sr isochron age at 46.3 ± 2.8 in Rocciavrè metagabbros (mostly constrained by peak phengite analyses) also suggests overlapping peak burial ages for the Lago Superiore unit and Rocciavrè LPL units (Angiboust and Glodny 2020).

With a similar lithostratigraphic content (volumetrically dominant gabbros and serpentinites overlaid by a thin sedimentary series restricted to Upper Jurassic sediments; e.g., Herviou et al. 2022), overlapping magmatic and metamorphic ages and peak P–T conditions in the same range, the Rocciavrè and Lago Superiore LPL units can be considered as true analogues. These different characteristics are globally shared by all mafic-ultramafic–dominated LPL units (Lago Superiore, Rocciavrè, Savoy Lower unit, Avic, Zermatt-Saas), suggesting their similar initial palaeogeography close to the continental margin and equivalent mechanical processes controlling their slicing at depth of ~70–80 km, during a short-lived period prior to continental subduction (Agard 2021; Herviou et al. 2022).

11.2 | Different Fluid Sources Detected During Oceanic Crust Subduction

Metamorphic veins reflect crystal growth in fractures and are generally considered the best rock record of fossil fluid circulation and fluid–rock interactions (e.g., Oliver and Bons 2001). Their mineralogy and geochemistry therefore give valuable clues on fluid sources responsible for vein formation and, in consequence, on the scales of fluid migration (e.g., Spandler, Pettke, and Rubatto 2011; Locatelli et al. 2019). In the following points, mineral assemblages, mineral compositions and FI chemistry (salinity, gas content, solids) of the high-pressure veins and their host rocks are used to discuss potential fluid sources. P–T conditions of the different steps of vein formation, presented in Figure 13a–e, are briefly addressed here and detailed in the following discussion section.

11.2.1 | Evidence From Vein Mineral Assemblages and Their Compositions

Omphacite-rich veins and garnet-rich veins contain minerals (omphacite or garnet ± rutile; Figures 2c and 3d–g) occurring in the peak burial eclogite-facies assemblage preserved in host Fe-Ti metagabbros (Figures 3a and 7a). In these veins, omphacite and garnet crystals have compositions and zoning patterns similar to the same minerals in Fe-Ti metagabbros (Figures 5a–c and 6a,b,d,f), suggesting vein formation at or close to peak burial and a potential local fluid source (Figure 13a,e). In addition, the folded and tortuous structure of these veins suggests their early formation (Figure 3e,g). Similar omphacite-rich and omphacite-garnet–rich veins and breccia matrices from the Monviso massif are interpreted to form at eclogite-facies conditions and to be related to a local fluid transfer, at least for the majority of them (Spandler, Pettke, and Rubatto 2011; Locatelli et al. 2018, 2019; Herviou et al. 2021).

In contrast to omphacite-rich veins, omphacite-quartz–rich veins contain large amounts of quartz (Figures 2b–e and 3h), which is only a minor phase in Rocciavrè Fe-Ti metagabbros (modal proportion reaching a few vol.% at most), suggesting that the fluid was Si-rich. These veins also contain centimetre-long prisms of rutile (Figure 2d) and have omphacite zoning patterns different from those observed in the host rocks (Figures 6g–h and 10; see also Figure 5). In omphacite-quartz veins, the presence of quartz, allanite, monazite and the U enrichment of rutile crystal rims suggests that the fluid was enriched in elements (Si, REE, U, P, Ca) that can be mobilized in high-pressure fluids (e.g., Ague 2017) and previously interpreted as likely to reflect a sedimentary source because of their high concentrations in sediments (e.g., Bebout and Barton 1989; Gyomlai et al. 2021; Herviou and Bonnet 2023; Figures 4f, 10 and 13b). The oscillatory Cr-rich zoning pattern near the rims of rutile crystals (Figure 10) could reflect an ultramafic contribution (e.g., Spandler, Pettke, and Rubatto 2011; Angiboust et al. 2014) or a contribution from less differentiated metagabbros (closer to a Mg-Al composition; Locatelli et al. 2019). Hourglass (sector) zoning patterns for some HFSE in rutile likely evidence a differential uptake of elements on some crystal faces, controlled by the crystal structure (Dowty 1976; Van Hinsberg et al. 2006; Lefeuvre et al. 2024), whereas oscillatory zoning patterns of omphacite may reflect the local breakdown of hydrous minerals (such as already documented in the Monviso eclogitic vugs; Angiboust and Raimondo 2022). Vein textures (i.e., coarse-grain omphacite crystals close to the veins walls with broken textures and prismatic omphacite crystals hosting quartz inclusions close to the vein cores) and field relationships suggest that omphacite-quartz–rich veins likely correspond to former omphacite-rich veins that were reopened (Figures 2c and 13b). Considering that omphacite-rich veins likely formed at conditions close to peak burial, the formation of omphacite-quartz–rich veins therefore occurred at a later stage during the early part of the retrograde P–T path. Precise P–T conditions for the formation of these veins are challenging to estimate considering their high variance mineral assemblage. However, they are expected to occur somewhere on the retrograde P–T path between peak burial and the jadeite-out reaction (jadeite + quartz = albite reaction; Figure 13e). The absence of glaucophane, except in late features such as replacing omphacite crystals (Figure 4b) and in epidote/clinozoisite-apatite-glaucophane-quartz aggregates (Figure 4e), likely suggests the formation of the omphacite-quartz–rich veins before entering in the epidote-blueschist-facies (Figure 13e). The early retrograde character of these high-pressure veins is demonstrated by our monazite U-Pb age of 40.4 ± 0.2 Ma (Figure 12), significantly younger than the 46.3 ± 2.8 Ma age considered for peak burial (Angiboust and Glodny 2020).

The mineralogical content of glaucophane-quartz–rich veins resembles that of omphacite-quartz–rich veins, except that glaucophane occurs instead of omphacite (Figure 3i). Omphacite inclusions in glaucophane crystals suggest that glaucophane-quartz–rich veins may correspond to former omphacite-quartz–rich veins in which anhydrous clinopyroxene was replaced by a hydrous phase of close chemistry (i.e., glaucophane) during an episode of fluid infiltration (Figure 13c). The association of epidote/clinozoisite with glaucophane crystals suggests that crystallization of epidote/clinozoisite-apatite-glaucophane-quartz aggregates was contemporaneous to vein formation and that the fluid was carrying elements such as Si, P and Ca. Although petrological clues

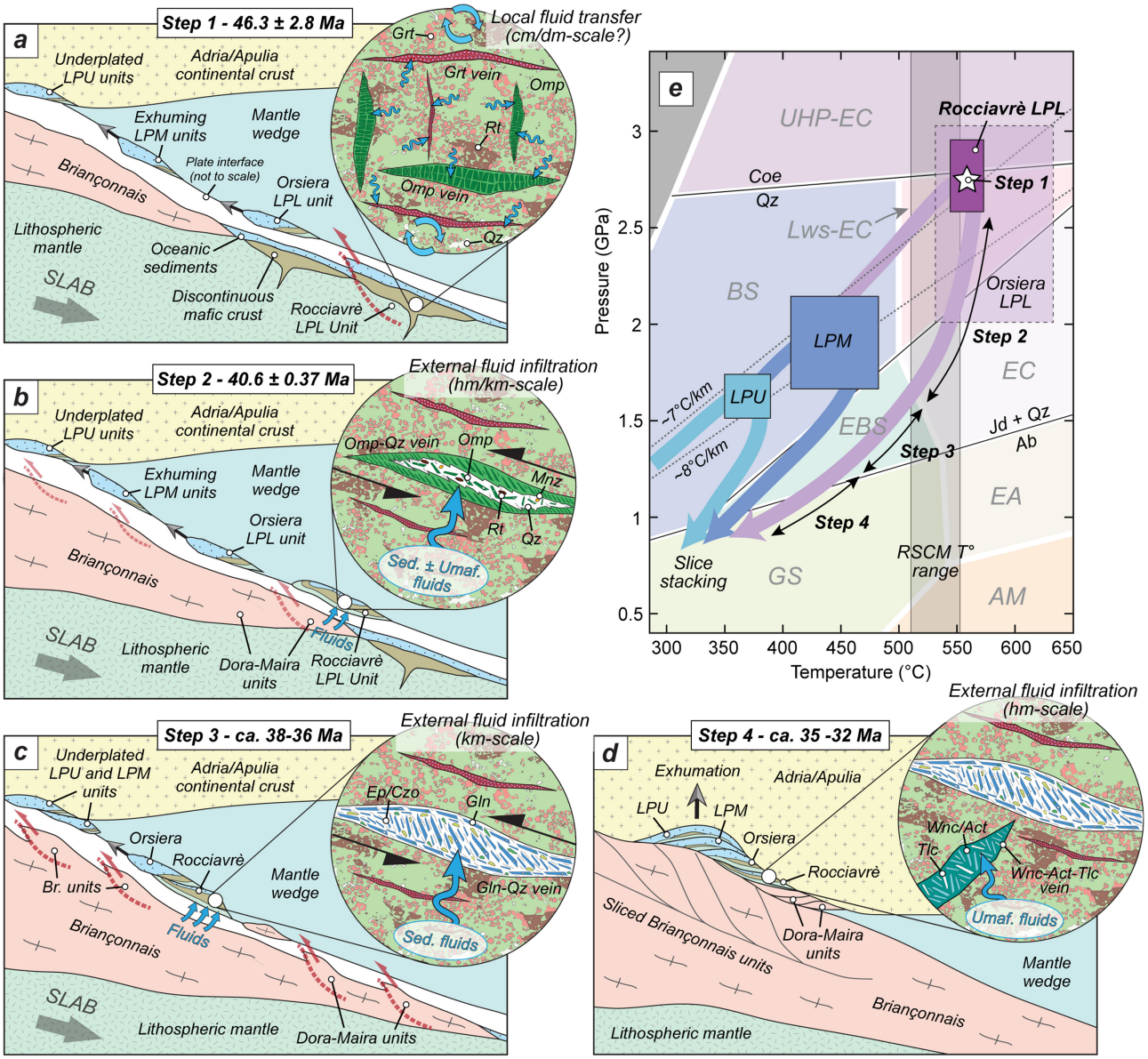

FIGURE 13 | (a) to (e) Different steps of fluid transfer and vein formation during burial and exhumation of the Rocciavrè unit in subduction. Step 1 corresponds to the formation of omphacite-rich and garnet-rich veins during local fluid transfer (cm-dm-scale) at peak burial (~545°C–570°C/2.6–2.9 GPa; 46.3 ± 2.8 Ma). Step 2 corresponds to the formation of omphacite-quartz–rich veins by the reopening of former omphacite-rich veins. This step records the infiltration of external sediment-derived (± ultramafic-derived) fluids, during exhumation at eclogite-facies conditions (40.4 ± 0.2 Ma). Step 3 corresponds to the formation of glaucophane-quartz–rich veins by reopening former omphacite-rich (and/or omphacite-quartz–rich veins) during exhumation in the epidote-blueschist-facies (ca. 38–36 Ma). These veins record the km-scale infiltration of sediment-derived fluids likely coming from the underlying and subducting Briançonnais micro-continent. Step 4 corresponds to the formation of winchite-actinolite-talc veins recording the infiltration of ultramafic-derived fluids at greenschist-facies conditions during exhumation and slice stacking (ca. 35–32 Ma). The different types of high-pressure veins observed in the Rocciavrè eclogitic massif therefore record the evolution of fluid migration scales in the subducted oceanic lithosphere, from local fluids transferred over small distance at peak burial to large kilometre-scale circulation and infiltration of external fluids during exhumation. The orientation and position of the blue arrows illustrating the fluids in (b) to (d) do not aim to characterize a preferential fluid pathway. Abbreviations: Act: actinolite; AM: amphibolite-facies; BS: blueschist-facies; Coe: coesite; EBS: epidote-blueschist-facies; EA: epidote-amphibolite-facies; EC: eclogite-facies; Ep/Czo: epidote/clinozoisite; Gln: glaucophane; Grt: garnet; GS: greenschist-facies Jd: jadeite; LPU: Liguro-Piemont Upper units; LPM: Liguro-Piemont Middle units; LPL: Liguro-Piemont Lower units; Omp: omphacite; Lws-EC: lawsonite-eclogite-facies; Qz: quartz; RSCM: Raman Spectroscopy on Carbonaceous Material; Sed.: sediment; Tlc: talc; UHP-EC: ultra-high-pressure-eclogite-facies; Umaf.: ultramafic; Wnc: winchite.

are limited to determining a precise fluid source, there is no evidence of any major fluid change compared with omphacite-quartz–rich veins. The widespread crystallization of glaucophane, locally at the expense of vein omphacite crystals associated with epidote/clinozoisite, suggests the formation of the glaucophane-quartz–rich veins along the retrograde path and at epidote-blueschist-facies conditions (Evans 1990; Figure 13e).

Finally, winchite-actinolite-talc veins have a very distinct mineral assemblage compared with the other vein types. The presence of these three phases having high magnesium contents suggests that the fluid was Mg-rich. In addition, talc and actinolite are ubiquitous phases in altered ultramafic rocks (e.g., Spandler et al. 2008; Herviou and Bonnet 2023; Nishiyama et al. 2023), also commonly observed in sheared Mg-Al metagabbros suggesting an ultramafic or Mg-Al gabbro fluid source (Figure 13d). Amphibole and talc crystals are generally millimetre-long, automorphous and with almost no evidence of plastic deformation (Figure 3j) supporting a late formation of these veins during exhumation. Although talc is stable over a very large range of P–T conditions across subduction gradients (e.g., Peacock and Wang 2021), winchite and actinolite crystallization along retrograde HP-LT P–T paths generally occurs from the blueschist-greenschist-facies transition to greenschist-facies conditions (Banno and Sakai 1989; Otsuki and Banno 1990; Wintsch, Byrne, and Toriumi 1999; Figure 13e).

11.2.2 | Evidence From Fluid Inclusion Salinity

Salinity values estimated for FIs hosted in the Fe-Ti metagabbro (mean: 18.5 wt.% NaCl eq.), in the garnet-rich vein (mean: 22.4 wt.% NaCl eq.), in the omphacite-rich veins (mean: 15.1 wt.% NaCl eq.), in the omphacite-quartz–rich veins (mean: 19.2 wt.% NaCl eq.) and in the winchite-actinolite-talc vein (mean: 23.2 wt.% NaCl eq.) are elevated and significantly higher than the values considered for Late Jurassic seawater (~3.7–4.2 wt.% NaCl eq.; Hay et al. 2006; Figure 9d–e and Table 2).

Such high salinity values have previously been reported in blueschist- and eclogite-facies Alpine metagabbros and associated high-pressure veins (Philippot and Selverstone 1991; Selverstone et al. 1992; Nadeau, Philippot, and Pineau 1993; Vallis and Scambelluri 1996; Philippot, Agrinier, and Scambelluri 1998; Herviou et al. 2021), also in Alpine serpentinites (Scambelluri et al. 1997). Similar $\delta^{18}O$ values between pyroxene crystals and whole rocks of Alpine metagabbros compared with hydrothermally altered ophiolites led authors to propose that estimated high salinity values are at least partially inherited from hydrothermal alteration on the seafloor (e.g., Philippot, Agrinier, and Scambelluri 1998; Scambelluri and Philippot 2001). Indeed, during near-ridge high-temperature hydrothermal alteration of gabbros, phase separation leading to the formation of brine-rich (up to > 50 wt.% NaCl eq.) and vapour-rich fluids is generally observed in FIs (e.g., Vanko 1988; Kelley, Robinson, and Malpas 1992; Kelley and Delaney 1987; Verlaguet et al. 2020). In addition, the storage of large chlorine concentrations in minerals and at mineral grain boundaries of mafic and ultramafic rocks is recognized to occur during hydrothermal alteration (e.g., Sharp and Barnes 2004; Bonifacie et al. 2008; Barnes and Cisneros 2012). In the Western Alps, evidence of intensive hydrothermal alteration that affected the slow-spreading (Lagabrielle and Cannat 1990) oceanic lithosphere are notably highlighted not only by hydrothermal phase relicts and their high Cl-content (Debret et al. 2016) but also by hydrothermal isotopic signatures ($\delta^{18}O$, $\delta^{37}Cl$, $\delta^{11}B$, $\delta^{65}Cu$) preserved up to eclogite-facies conditions (Nadeau, Philippot, and Pineau 1993; Busigny, Cartigny, and Philippot 2011; Busigny et al. 2018; Selverstone and Sharp 2013; Martin et al. 2020; Cannaò et al. 2023). The high salinity values observed in Alpine metagabbros and related high-pressure veins are therefore interpreted to record a hydrothermal signature potentially related to a partitioning of the inherited high chlorine content in the fluid phase during minor dehydration reactions (such as considered for the brucite-out reaction in serpentinites; Scambelluri et al. 1997) and to the partial recycling of the brines initially trapped on the seafloor (Nadeau, Philippot, and Pineau 1993).

It is worth noting that (i) limited dehydration of the subducted hydrothermally altered Alpine metagabbros is predicted to have occurred prior to chlorite- and lawsonite-out reactions (Figure 7a; Herviou et al. 2021; their §7.3) and (ii) the salinity values recorded in our Fe-Ti metagabbros and high-pressure veins (such as for the equivalent veins of the Monviso massif; Philippot and Selverstone 1991; Herviou et al. 2021) are elevated but significantly lower than those of hydrothermal brines (e.g., Kelley and Delaney 1987) or those previously estimated in Rocciavrè for low-strained metagabbros with preserved magmatic textures (Philippot, Agrinier, and Scambelluri 1998). These two points suggest that high salinity may be preserved up to eclogite-facies conditions and that the dehydration reactions encountered may have lowered the initial salinity of hydrothermal fluids that may only have been preserved in undeformed and less metamorphosed rocks.

In contrast to the Fe-Ti metagabbro sample and most high-pressure veins, primary FI salinity values are significantly lower in the Orsiera metabasalt (mean: 8.3 wt.% NaCl eq.) and in the glaucophane-quartz–rich vein (mean: 13.1 wt.% NaCl eq.), yet still higher than the Late Jurassic seawater (Figure 9d–e and Table 2). Hydrothermal alteration generally occurs at lower temperature in basalts compared with gabbros, preventing phase separation and brine formation (e.g., Kelley, Robinson, and Malpas 1992). Metabasalts are therefore not expected to preserve highly saline fluids inherited from hydrothermal processes (Philippot, Agrinier, and Scambelluri 1998; Herviou et al. 2021), which might explain the lower salinity values of FIs from our Orsiera sample. However, glaucophane-quartz–rich veins are cross-cutting Fe-Ti metagabbros and locally produced fluids are expected to be highly saline. The lower salinity values of these veins might therefore record an external fluid source. The fluids produced during devolatilization at high pressure of the Liguro-Piemont metasediments have a low to intermediate salinity generally lower than 10 wt.% NaCl eq. (Agard et al. 2000; Herviou et al. 2021; Herviou and Bonnet 2023). The salinity values recorded in the glaucophane-quartz–rich veins may therefore record a mixing between the highly saline fluids produced locally and externally derived low saline fluids, potentially coming from a sedimentary source.

11.2.3 | Evidence From Fluid Inclusion Gas Content and Solids

A strong N_2 signal was detected in most FIs (Figure 9a). N_2 is a gas species commonly detected in eclogite-facies FIs, generally interpreted as inherited from the breakdown of pre-eclogitic NH_4^+-bearing minerals such as amphiboles, feldspar and micas (Andersen, Burke, and Austrheim 1989; Andersen, Austrheim,

and Burke 1990; Andersen et al. 1993; Klemd, Van den Kerkhof, and Horn 1992; Mukherjee and Sachan 2009). In the Western Alps, N_2 was recently detected in primary FIs from eclogite-facies omphacite-bearing veins and breccia matrices from the Monviso Lago Superiore unit (Herviou et al. 2021), analogous to the Rocciavrè unit. In addition, although N is considered as being retained up to subarc depths in Liguro-Piemont sediments (Busigny et al. 2003; Philippot et al. 2007; Bebout et al. 2013); omphacite-bearing veins of the Monviso have higher N concentrations than their host Fe-Ti metagabbros (Busigny, Cartigny, and Philippot 2011; Busigny et al. 2018), suggesting that N_2 is likely released in the fluids by prograde to peak dehydration reactions in the gabbros but not during sediment devolatilization. Therefore, N in the form NH_4^+ might have been transported by K-Na-Ca–bearing minerals such as glaucophane during subduction (e.g., Halama et al. 2017; Halama and Bebout 2021) and later released and trapped in FIs as N_2 during their breakdown at eclogite-facies conditions (Herviou et al. 2021). In the Rocciavrè Fe-Ti metagabbros, the glaucophane-out reaction is predicted to occur at around 520°C–550°C/2.3–2.5 GPa along a ~7°C–8°C/km gradient (Figure 7a) such as considered for the Alpine oceanic subduction (e.g., Agard, Jolivet, and Goffe 2001; Agard 2021; Herviou et al. 2022). The N_2 signature detected in our samples is thus considered as reflecting the local devolatilization of mafic rocks at conditions close to peak burial.

The presence of CO_2 (1285 and 1388 cm^{-1} peaks) was also detected in two N_2-bearing aqueous FIs from garnet of the Orsiera metabasalt. CO_2-bearing fluids have already been described in primary FIs from eclogites (e.g., El-Shazly and Sisson 1999) sometimes associated with N_2 (e.g., Selverstone et al. 1992). In addition to the association of CO_2 and N_2 in a few primary FIs, the presence of a solid phase identified as calcite in numerous FIs from omphacite-bearing veins and one FI from a garnet-rich vein suggest the presence of an initial N_2-CO_2–bearing aqueous fluid at peak burial conditions. In similar omphacite-bearing veins and Fe-Ti metagabbro host from the Monviso, the occurrence of various carbonates in primary FIs was also interpreted as reflecting the initial presence of CO_2 in the fluids (Philippot and Selverstone 1991; Herviou et al. 2021).

Finally, CO_2 and CH_4 peaks were simultaneously observed in two inclusions from the glaucophane-quartz–rich vein where no N_2 was detected (Figure 9b). Thus, this sample, which contains FIs with significantly different salinity values compared with the other vein types, also has a distinct gas content, suggesting a different fluid source. Low-to-intermediate salinity aqueous CO_2-CH_4–bearing fluids have been identified in lawsonite- and Fe-Mg carpholite-bearing high-pressure veins from the surrounding Liguro-Piemont sediments (Agard et al. 2000; Raimbourg et al. 2018. Herviou et al. 2021). This signature was interpreted to reflect local fluids produced by dehydration reactions and interacting with carbonate- and carbonaceous material–rich horizons of the sediments (Herviou et al. 2021). The exact same fluid composition was also identified in primary FIs from former ultramafic horizons transformed by the infiltration of sediment-derived fluids at peak burial (Herviou and Bonnet 2023). Therefore, the glaucophane-quartz–rich FIs likely records an external fluid migration from a sedimentary fluid source, occurring during exhumation of the Rocciavrè LPL unit at epidote-blueschist-facies conditions.

11.3 | Successive Steps of Vein Formation: Implications for Scales of Fluid Transfer in Subduction, for Strain Localization and for Exhumation of Alpine Oceanic Units

Based on structural, petrological, geochemical and geochronological evidence, several steps of vein formation occurring in subduction during burial and exhumation of the Rocciavrè LPL unit are identified. We hereafter describe the successive steps of veining and assess the potential impacts of our results on strain localization and on the exhumation of Alpine oceanic units.

After the crystallization of its mafic crust during the Late Jurassic (Figure 11a–b), the first high-pressure fluid transfer event recorded in the Rocciavrè massif corresponds to the formation of omphacite-rich and garnet-rich veins (Step 1; Figure 13a,e). As suggested by the similar mineralogical content of these veins with respect to the host Fe-Ti metagabbros, this episode occurred in the (lawsonite-) eclogite-facies at or close to peak burial conditions (~545°C–570°C/2.6–2.9 GPa; Figure 7a and Table 1). Therefore, these veins likely formed at around 46.3 ± 2.8 Ma (Angiboust and Glodny 2020) when the Rocciavrè LPL unit was being sliced off the downgoing plate. At this time, the Orsiera LPL unit was already exhuming and the LPM and LPU blueschist-facies units were either exhuming or already underplated at the base of Adria/Apulia continental crust (Agard et al. 2002; Herviou et al. 2022; Gyomlai et al. 2023; Figure 13a). In addition to the observed mineral assemblages, the high FI salinity accompanied by the presence of $N_2 \pm CO_2$ (calcite crystals in FIs; Figure 9a,c,d,e and Table 2) suggests that the fluids were produced by local dehydration reactions occurring in the Fe-Ti metagabbros. Highly saline brines (up to > 50 wt.% NaCl eq.), trapped as chlorine in minerals and in inclusions during hydrothermal alteration, were likely diluted during breakdown of hydrous minerals, explaining the ~15–20 wt.% NaCl eq. salinity values estimated in omphacite-rich and garnet-rich veins (Figure 9d–e and Table 2). With Alpine glaucophane likely containing N bound as NH_4^+ (Herviou et al. 2021) and high chlorine concentrations (Debret et al. 2016), the glaucophane-out reaction, occurring at conditions close to peak burial (at ~520°C–550°C/2.3–2.5 GPa for a ~7°C–8°C/km gradient; Figure 7a), is a good candidate. Fluid migration is therefore expected to have occurred at a multicentimetre to multimetre scale (Figure 13a).

The second veining episode recorded in the rocks corresponds to the formation of omphacite-quartz–rich veins (Step 2 Figure 13b,e). During this step, we interpret that former omphacite-rich veins are intensively sheared and likely reopened leading to the crystallization of new omphacite crystals and quartz. Omphacite-quartz–rich veins formed at conditions close to peak burial, suggesting that this later step occurred along the retrograde P–T paths somewhere in the eclogite-facies (Figure 13e), as attested by our monazite U-Pb age of 40.4 ± 0.2 Ma (Figure 12). At this time, the continental subduction is well established; all Liguro-Piemont units of the studied area are exhuming or being underplated to Adria/Apulia continental crust (Agard et al. 2002; Angiboust and Glodny 2020; Ghignone et al. 2021b; Gyomlai et al. 2023), whereas units from the Briançonnais microcontinent (Briançonnais s. s. and Internal Crystalline Massifs) are starting to get scrapped off the continental slab (e.g., Bonnet et al. 2022; Mendes et al. 2023).

The new age falls halfway between the ages considered for Rocciavrè peak burial and exhumation in epidote-blueschist-facies conditions (46.3 ± 2.8 Ma and ca. 38–36 Ma, respectively; Angiboust and Glodny 2020), suggesting that mafic-ultramafic–dominated LPL units such as Rocciavrè or the Monviso-Lago Superiore started to exhume before the offscraping of Dora-Maira Brossasco-Isasca ultra-high-pressure unit (ca. 35–34 Ma; Rubatto and Hermann 2001) and that exhumation of these eclogitized oceanic lithosphere portions was not only driven by the positive buoyancy of the continental units. The large amount of quartz, the occurrence of accessory minerals not observed in omphacite-rich veins (monazite, allanite; Figure 4f) and the presence of U-rich rims of rutile crystals (Figure 10) suggest a potential change in the fluid source during this event compared with first step of vein formation, and we think that it most likely that these characteristics are caused by the contribution of an infiltrating externally derived fluid. We therefore propose that the main fluid source involved corresponds to sediment-derived fluids enriched in elements such as Si, REE, U and P and likely derived from the Briançonnais microcontinent underlying the exhuming Rocciavrè unit at this time. N_2-bearing ($\pm CO_2$) saline aqueous fluids characterized by FI study (Figure 9a,c,d,e and Table 2) from these veins suggest that local fluids released by the metagabbros were also involved in this event. Finally, the Cr-rich rims of rutile crystals (Figure 10) also suggest a partial fluid contribution from ultramafic rocks or metagabbros closer in composition to a Mg-Al endmember (e.g., Spandler, Pettke, and Rubatto 2011; Angiboust et al. 2014; Locatelli et al. 2019). Fluid circulation is expected to have occurred at a significantly larger scale compared with the first step. Although the typical transportation range occurs on the centimetre/decimetre scale for the local mafic contribution as documented for Monviso by Spandler, Pettke, and Rubatto (2011) and Angiboust and Raimondo (2022), fluid flow on the order of hectometre scale for the ultramafic/Mg-Al gabbros contribution to kilometre scale is proposed for the continental sediment contribution (Figure 13a).

The third recorded fluid–rock interaction episode corresponds to the formation of glaucophane-quartz–rich veins during the exhumation of the Rocciavrè unit (Step 3; Figure 13c,e). This episode likely occurred in epidote-blueschist-facies conditions as suggested by the presence of glaucophane and epidote/clinozoisite. In Rocciavrè and Monviso massifs, epidote-blueschist-facies retrograde conditions have already been documented by the observation of a glaucophane-bearing west–east lineation and the crystallization of a new phengite generation in metasediments. The Rb-Sr dating of this generation of white mica crystals suggests the crossing of the epidote-blueschist-facies along Rocciavrè and Monviso exhumation paths at ca. 38–36 Ma (Angiboust and Glodny 2020). The same age range obtained in several shear zones bounding the tectonic slices and the shear bands in the neighbouring units suggests that the Liguro-Piemont units started to get stacked together in this time range (Agard et al. 2002; Angiboust and Glodny 2020; Herviou and Bonnet 2023; Figure 13c), whereas most Briançonnais units, including Dora-Maira ones, were being scrapped off the downgoing plate (e.g., Strzerzynski et al. 2012; Bonnet et al. 2022; Mendes et al. 2023). During this retrograde event, former omphacite-quartz–rich (or omphacite-rich) veins are again highly sheared and reopened, leading to the crystallization of quartz, epidote/clinozoisite, apatite and glaucophane (growing locally around omphacite crystals; Figure 13c). The different mineral assemblage of these veins, containing large amounts of quartz compared with the host Fe-Ti metagabbros and to the peak veins (omphacite-rich and garnet-rich), suggests again a contribution from a different fluid source. In addition, the low-to-intermediate salinity CO_2-CH_4–bearing aqueous fluids identified in primary FIs (Figure 9b,d,e and Table 2) have a similar composition to those previously characterized in high-pressure veins from the surrounding Liguro-Piemont metasediments (Herviou et al. 2021; Herviou and Bonnet 2023), suggesting a sediment-derived fluid source. We therefore propose that the glaucophane-quartz–rich veins likely record the infiltration of external fluids coming from continental sediments of the underlying Briançonnais margin during exhumation of the Rocciavrè unit (Figure 13a,d). Fluid migration would thus have reached a kilometric scale during this third step. Such a large-scale fluid migration event is consistent with widespread vein formation in LPU-LPM sediments and titanite recrystallization in talcschists, both dated at the same age (ca. 38–35 Ma; Agard et al. 2000; Herviou and Bonnet 2023). A continental margin sediment source is supported by the ^{87}Sr- and Ar-rich fluids leading to the recrystallization of Orsiera metasediment phengite crystals at ca. 38 Ma (Gyomlai et al. 2023). Finally, the slightly higher salinity values recorded in FIs from these veins, compared with Liguro-Piemont sediments, may reflect (i) a redistribution of the local fluids trapped in minerals (chlorine, FIs) during external fluid infiltration, (ii) an increase of the residual fluid salinity during the formation of hydrous minerals (i.e., glaucophane and epidote; e.g., Brooks et al. 2019) and (iii) simply the signal of continental margin sediment fluids, having a greater evaporite content compared with oceanic sediments (Yardley and Graham 2002; Barré et al. 2017; Herviou et al. 2021).

The final step of vein formation corresponds to the development of winchite-actinolite-talc veins (Step 4; Figure 13d,e). Although the precise timing and P–T conditions of this episode are challenging to constrain, the presence of winchite and actinolite suggests a late vein formation in greenschist-facies conditions, thus likely after ca. 35 Ma when all oceanic and continental units are stacked together at the base of Adria/Apulia continental crust (~30 km depth; Angiboust and Glodny 2020; Agard 2021; Bonnet et al. 2022). Around this time, the Briançonnais units were stacked against the Liguro-Piemont metamorphic duplex, leading to the preservation of a continental subduction interface (Mendes et al. 2023; Figure 13d) and to the orogenic style change from continental subduction to collision (Simon-Labric et al. 2009). In serpentinites, the partitioning of the hydrothermally inherited high chlorine concentrations in the fluid during the brucite-out reaction generally leads to high salinity fluids trapped in FIs, whereas during the antigorite-out reaction, chlorine is diluted in the larger volumes of H_2O released, leading to the trapping of low salinity fluids in FIs (Scambelluri et al. 1997, 2001, 2004; Scambelluri, Pettke, and Cannaò 2015; Kendrick et al. 2011). Our winchite-actinolite-talc veins have the highest FI salinity values among our samples (Figure 9d,e and Table 2), suggesting that the fluids responsible for its formation may be external and could have interacted with the underlying serpentinite sole, or the Mg-Al metagabbros. Fluid migration from the Rocciavrè basal serpentinites to the Fe-Ti metagabbros would therefore be at a hectometre scale (Figure 13d). The presence of N_2 detected in one FI is interpreted as reflecting a local contribution from Fe-Ti metagabbros.

Previous isotopic, trace element and FI studies suggest a globally closed-system behaviour with limited external fluid infiltration during subduction of the Liguro-Piemont oceanic lithosphere at prograde to peak burial conditions (Philippot and Selverstone 1991; Henry, Burkhard, and Goffé 1996; Bebout et al. 2013; Epstein et al. 2020; Herviou et al. 2021; Hoover et al. 2023). A rather pervasive flow of fluids compatible with a relatively limited scale (outcrop-scale) of fluid circulation in these units during subduction is also supported by the distribution of high-pressure veins across outcrops (Herviou et al. 2023). In contrast, larger scale fluid circulation is recorded along major lithological boundaries and tectonic contacts (Angiboust et al. 2014, Debret et al. 2016, 2018; Inglis et al. 2017; Jaeckel, Bebout, and Angiboust 2018; Locatelli et al. 2019; Gilio et al. 2020; Epstein, Bebout, and Angiboust 2021; Herviou and Bonnet 2023). This study suggests that successive steps of high-pressure vein formation observed in the Rocciavrè eclogites record the evolution of fluid migration scales in the subducted oceanic lithosphere, from local fluids transferred over small distances at near-peak burial to large kilometre-scale circulation and infiltration of external fluids during exhumation (Figure 13a–e). This change of behaviour likely started early along the retrograde path, as suggested by the omphacite-quartz–rich vein formation (Figure 13b,e).

Finally, the successive reopening of former omphacite-rich veins during the formation of omphacite-quartz–rich and glaucophane-quartz–rich veins, as well as the highly sheared aspect of these quartz-bearing veins, suggests that veins acted as weaker zones where fracturing preferentially occurred. Although preexisting veins likely helped to localize strain in the rocks, the crystallization of large volumes of quartz may have had an important rheological effect, leading to a weakening of the Fe-Ti metagabbros and to the development of breccia-like textures (Figure 2e). Successive events of strain localization and fracturing of these veins could lead to the formation of high-pressure breccias such as observed in the Monviso massif (Angiboust et al. 2011, 2012a; Locatelli et al. 2018, 2019), in the Mt. Emilius continental unit (Angiboust et al. 2017, Hertgen et al. 2017), in the Voltri Massif (Malatesta et al. 2018), in Calabria (Vitale et al. 2019) and in the Zagros suture zone (Muñoz-Montecinos et al. 2023).

12 | Conclusion

This study reports new petrochronological estimates for the Rocciavrè massif, a large and coherent oceanic lithosphere fragment exposed in the Western Alps (Piemonte, Italy) that was buried up to eclogite-facies conditions during subduction. Thermodynamic modelling conducted in mafic rocks from Rocciavrè and from the nearby Orsiera unit indicates peak P–T conditions in the range 550°C–590°C/2.2–3.0 GPa, whereas Raman spectroscopy on carbonaceous material in metasediments yields temperatures of ~510°C–550°C. No metamorphic gap is detected between these two juxtaposed eclogitic units. Zircon crystals separated from Rocciavrè Fe-Ti and Mg-Al metagabbros dated using U-Pb geochronology give Late Jurassic ages (ca. 151–158 Ma), thus reflecting crystallization on the seafloor.

In addition to these new P–T–t constraints, a variety of high-pressure veins were identified crosscutting the foliation of Rocciavrè Fe-Ti metagabbros and include garnet-rich, omphacite-rich, omphacite-quartz–rich, glaucophane-quartz–rich and winchite-actinolite-talc varieties. Vein textures and mineralogy suggest the formation of garnet-rich and omphacite-rich veins in the eclogite-facies at or close to peak burial conditions. In contrast, omphacite-quartz–rich and glaucophane-quartz–rich veins are interpreted to form by the reopening of former omphacite-rich veins at eclogite- to epidote-blueschist-facies conditions along the exhumation path. In situ U-Pb dating of monazite in omphacite-quartz–rich veins yields a constraint on the age at 40.4 ± 0.2 Ma. Winchite-actinolite-talc veins are considered as late retrograde greenschist-facies features. Major and trace element mapping of vein minerals and primary FI geochemistry suggests the evolution from a closed to an open chemical system during the successive steps of vein formation from peak burial to exhumation. Late sedimentary and ultramafic fluid contributions identified in retrograde high-pressure veins witness the mobility of fluids through the oceanic lithosphere during subduction, likely reaching kilometre-scale transport distances. We conclude that the Rocciavrè massif, which shares a similar metamorphic history to the Monviso Lago Superiore Unit further south, enables a precise characterization of fluid–rock interaction processes in subduction from eclogite-facies to epidote-blueschist-facies and greenschist-facies conditions.

Acknowledgements

This study was partly funded by a RGF-Alpes project (BRGM) and by an ENS de Lyon grant to S. Angiboust. W. Hoover and an anonymous reviewer are thanked for their insightful suggestions. S. Penniston-Dorland is thanked for constructive comments that helped improve the manuscript and for editorial handling. The authors thank N. Rividi, O. Boudouma, M.-C. Caumon, M. Fialin, M. Button, E. Delairis and M. Moroni for analytical and technical support.

References

Abers, G. A., P. E. Van Keken, E. A. Kneller, A. Ferris, and J. C. Stachnik. 2006. "The Thermal Structure of Subduction Zones Constrained by Seismic Imaging: Implications for Slab Dehydration and Wedge Flow." *Earth and Planetary Science Letters* 241: 387–397. https://doi.org/10.1016/j.epsl.2005.11.055.

Agard, P. 2021. "Subduction of Oceanic Lithosphere in the Alps: Selective and Archetypal From (Slow-Spreading) Oceans." *Earth-Science Reviews* 214: 103517. https://doi.org/10.1016/j.earscirev.2021.103517.

Agard, P., and M. R. Handy. 2021. "Ocean Subduction Dynamics in the Alps." *Elements* 17: 9–16. https://doi.org/10.2138/gselements.17.1.9.

Agard, P., B. Goffé, J. L. R. Touret, and O. Vidal. 2000. "Retrograde Mineral and Fluid Evolution in High-Pressure Metapelites (Schistes Lustrés Unit, Western Alps)." *Contributions to Mineralogy and Petrology* 140: 296–315. https://doi.org/10.1007/s004100000190.

Agard, P., L. Jolivet, and B. Goffe. 2001. "Tectonometamorphic Evolution of the Schistes Lustres Complex; Implications for the Exhumation of HP and UHP Rocks in the Western Alps." *Bulletin de la Societe Geologique de France* 172: 617–636. https://doi.org/10.2113/172.5.617.

Agard, P., P. Monie, L. Jolivet, and B. Goffe. 2002. "Exhumation of the Schistes Lustres Complex: In Situ Laser Probe 40Ar/39Ar Constraints

and Implications for the Western Alps." *Journal of Metamorphic Geology* 20: 599–618. https://doi.org/10.1046/j.1525-1314.2002.00391.x.

Agard, P., P. Yamato, L. Jolivet, and E. Burov. 2009. "Exhumation of Oceanic Blueschists and Eclogites in Subduction Zones: Timing and Mechanisms." *Earth-Science Reviews* 92: 53–79. https://doi.org/10.1016/j.earscirev.2008.11.002.

Agard, P., A. Plunder, S. Angiboust, G. Bonnet, and J. Ruh. 2018. "The Subduction Plate Interface: Rock Record and Mechanical Coupling (From Long to Short Timescales)." *Lithos* 320–321: 537–566. https://doi.org/10.1016/j.lithos.2018.09.029.

Ague, J. J. 2017. "Element Mobility During Regional Metamorphism in Crustal and Subduction Zone Environments With a Focus on the Rare Earth Elements (REE)." *American Mineralogist* 102: 1796–1821.

Aleinikoff, J. N., W. S. Schenck, M. O. Plank, et al. 2006. "Deciphering Igneous and Metamorphic Events in High-Grade Rocks of the Wilmington Complex, Delaware: Morphology, Cathodoluminescence and Backscattered Electron Zoning, and SHRIMP U-Pb Geochronology of Zircon and Monazite." *Geological Society of America Bulletin* 118: 39–64. https://doi.org/10.1130/B25659.1.

Andersen, T., E. A. J. Burke, and H. Austrheim. 1989. "Nitrogen-Bearing, Aqueous Fluid Inclusions in Some Eclogites From the Western Gneiss Region of the Norwegian Caledonides." *Contr. Mineral. And Petrol.* 103: 153–165. https://doi.org/10.1007/BF00378501.

Andersen, T., H. Austrheim, and E. A. J. Burke. 1990. "Fluid Inclusions in Granulites and Eclogites From the Bergen Arcs, Caledonides of W. Norway." *Mineralogical Magazine* 54: 145–158. https://doi.org/10.1180/minmag.1990.054.375.02.

Andersen, T., H. Austrheim, E. A. J. Burke, and S. Elvevold. 1993. "N_2 and CO_2 in Deep Crustal Fluids: Evidence From the Caledonides of Norway." *Chemical Geology* 108: 113–132. https://doi.org/10.1016/0009-2541(93)90320-I.

Angiboust, S., and P. Agard. 2010. "Initial Water Budget: The key to Detaching Large Volumes of Eclogitized Oceanic Crust Along the Subduction Channel?" *Lithos* 120: 453–474. https://doi.org/10.1016/j.lithos.2010.09.007.

Angiboust, S., and J. Glodny. 2020. "Exhumation of Eclogitic Ophiolitic Nappes in the W. Alps: New Age Data and Implications for Crustal Wedge Dynamics." *Lithos* 356–357: 105374. https://doi.org/10.1016/j.lithos.2020.105374.

Angiboust, S., and T. Raimondo. 2022. "Permeability of Subducted Oceanic Crust Revealed by Eclogite-Facies Vugs." *Geology* 50: 964–968. https://doi.org/10.1130/G50066.1.

Angiboust, S., P. Agard, L. Jolivet, and O. Beyssac. 2009. "The Zermatt-Saas Ophiolite: The Largest (60-Km Wide) and Deepest (c. 70-80 km) Continuous Slice of Oceanic Lithosphere Detached From a Subduction Zone?" *Terra Nova* 21: 171–180. https://doi.org/10.1111/j.1365-3121.2009.00870.x.

Angiboust, S., P. Agard, H. Raimbourg, P. Yamato, and B. Huet. 2011. "Subduction Interface Processes Recorded by Eclogite-Facies Shear Zones (Monviso, W. Alps)." *Lithos* 127: 222–238. https://doi.org/10.1016/j.lithos.2011.09.004.

Angiboust, S., P. Agard, P. Yamato, and H. Raimbourg. 2012a. "Eclogite Breccias in a Subducted Ophiolite: A Record of Intermediate-Depth Earthquakes?" *Geology* 40: 707–710. https://doi.org/10.1130/G32925.1.

Angiboust, S., R. Langdon, P. Agard, D. Waters, and C. Chopin. 2012b. "Eclogitization of the Monviso Ophiolite (W. Alps) and Implications on Subduction Dynamics." *Journal of Metamorphic Geology* 30: 37–61. https://doi.org/10.1111/j.1525-1314.2011.00951.x.

Angiboust, S., T. Pettke, J. C. M. De Hoog, B. Caron, and O. Oncken. 2014. "Channelized Fluid Flow and Eclogite-Facies Metasomatism Along the Subduction Shear Zone." *Journal of Petrology* 55: 883–916. https://doi.org/10.1093/petrology/egu010.

Angiboust, S., P. Yamato, S. Hertgen, T. Hyppolito, G. E. Bebout, and L. Morales. 2017. "Fluid Pathways and High- P Metasomatism in a Subducted Continental Slice (Mt. Emilius Klippe, W. Alps)." *Journal of Metamorphic Geology* 35: 471–492. https://doi.org/10.1111/jmg.12241.

Angiboust, S., A. Menant, T. Gerya, and O. Oncken. 2022. "The Rise and Demise of Deep Accretionary Wedges: A Long-Term Field and Numerical Modeling Perspective." *Geosphere* 18: 69–103. https://doi.org/10.1130/GES02392.1.

Ballèvre, M., and O. Merle. 1993. "The Combin Fault: Compressional Reactivation of a Late Cretaceous-Early Tertiary Detachment Fault in the Western Alps." *Schweizerische Mineralogische und Petrographische Mitteilungen* 73: 205–227. https://doi.org/10.5169/SEALS-55570.

Ballèvre, M., Y. Lagabrielle, and O. Merle. 1990. "Tertiary Ductile Normal Faulting as a Consequence of Lithospheric Stacking in the Western Alps." *Mémoires de la Société géologique de France* 156: 227–236.

Banno, S., and C. Sakai. 1989. "Geology and Metamorphic Evolution of the Sanbagawa Metamorphic Belt, Japan." *Geological Society of London, Special Publication* 43: 519–532. https://doi.org/10.1144/GSL.SP.1989.043.01.50.

Barnes, J. D., and M. Cisneros. 2012. "Mineralogical Control on the Chlorine Isotope Composition of Altered Oceanic Crust." *Chemical Geology* 326–327: 51–60. https://doi.org/10.1016/j.chemgeo.2012.07.022.

Barré, G., L. Truche, E. F. Bazarkina, R. Michels, and J. Dubessy. 2017. "First Evidence of the Trisulfur Radical ion S_3^- and Other Sulfur Polymers in Natural Fluid Inclusions." *Chemical Geology* 462: 1–14. https://doi.org/10.1016/j.chemgeo.2017.03.027.

Bebout, G. E., and M. D. Barton. 1989. "Fluid Flow and Metasomatism in a Subduction Zone Hydrothermal System: Catalina Schist Terrane, California." *Geology* 17: 976–980.

Bebout, G. E., and S. C. Penniston-Dorland. 2016. "Fluid and Mass Transfer at Subduction Interfaces—The Field Metamorphic Record." *Lithos* 240–243: 228–258. https://doi.org/10.1016/j.lithos.2015.10.007.

Bebout, G. E., P. Agard, K. Kobayashi, T. Moriguti, and E. Nakamura. 2013. "Devolatilization History and Trace Element Mobility in Deeply Subducted Sedimentary Rocks: Evidence From Western Alps HP/UHP Suites." *Chemical Geology* 342: 1–20. https://doi.org/10.1016/j.chemgeo.2013.01.009.

Beinlich, A., R. Klemd, T. John, and J. Gao. 2010. "Trace-Element Mobilization During Ca-Metasomatism Along a Major Fluid Conduit: Eclogitization of Blueschist as a Consequence of Fluid–Rock Interaction." *Geochimica et Cosmochimica Acta* 74: 1892–1922.

Bellanger, M., R. Augier, N. Bellahsen, et al. 2015. "Shortening of the European Dauphinois Margin (Oisans Massif, Western Alps): New Insights From RSCM Maximum Temperature Estimates and $^{40}Ar/^{39}Ar$ In Situ Dating." *Journal of Geodynamics* 83: 37–64. https://doi.org/10.1016/j.jog.2014.09.004.

Berger, A., and R. Bousquet. 2008. "Subduction-Related Metamorphism in the Alps: Review of Isotopic Ages Based on Petrology and Their Geodynamic Consequences." *Geological Society of London, Special Publication* 298: 117–144. https://doi.org/10.1144/SP298.7.

Beyssac, O., B. Goffé, C. Chopin, and J. N. Rouzaud. 2002. "Raman Spectra of Carbonaceous Material in Metasediments: A New Geothermomete." *Journal of Metamorphic Geology* 20: 859–871. https://doi.org/10.1046/j.1525-1314.2002.00408.x.

Black, L. P., S. L. Kamo, C. M. Allen, et al. 2003. "TEMORA 1: A New Zircon Standard for Phanerozoic U–Pb Geochronology." *Chemical Geology* 200: 155–170. https://doi.org/10.1016/S0009-2541(03)00165-7.

Bonifacie, M., V. Busigny, C. Mével, et al. 2008. "Chlorine Isotopic Composition in Seafloor Serpentinites and High-Pressure Metaperidotites. Insights Into Oceanic Serpentinization and Subduction Processes." *Geochimica et Cosmochimica Acta* 72: 126–139. https://doi.org/10.1016/j.gca.2007.10.010.

Bonnet, G., P. Agard, S. Angiboust, et al. 2018. "Tectonic Slicing and Mixing Processes Along the Subduction Interface: The Sistan Example (Eastern Iran)." *Lithos* 310–311: 269–287. https://doi.org/10.1016/j.lithos.2018.04.016.

Bonnet, G., C. Chopin, M. Locatelli, A. R. C. Kylander-Clark, and B. R. Hacker. 2022. "Protracted Subduction of the European Hyperextended Margin Revealed by Rutile U-Pb Geochronology Across the Dora-Maira Massif (Western Alps)." *Tectonics* 41: e2021TC007170. https://doi.org/10.1029/2021TC007170.

Bons, P. D., M. A. Elburg, and E. Gomez-Rivas. 2012. "A Review of the Formation of Tectonic Veins and Their Microstructures." *Journal of Structural Geology* 43: 33–62. https://doi.org/10.1016/j.jsg.2012.07.005.

Bouffette, J., and J. M. Caron. 1991. "Trajets Métamorphiques Prograde et Rétrograde Dans des Éclogites Piémontaises (Ouest du Massif du Rocciavrè, Alpes cottiennes)." *Comptes Rendus de l'Académie des Sciences - Série II* 312: 1459–1465.

Bousquet, R., R. Oberhänsli, B. Goffé, et al. 2008. "Metamorphism of Metasediments at the Scale of an Orogen: A Key to the Tertiary Geodynamic Evolution of the Alps." *Geological Society, London, Special Publications* 298: 393–411. https://doi.org/10.1144/SP298.18.

Brenan, J. M., H. F. Shaw, D. L. Phinney, and F. J. Ryerson. 1994. "Rutile-Aqueous Fluid Partitioning of Nb, Ta, Hf, Zr, U and Th: Implications for High Field Strength Element Depletions in Island-Arc Basalts." *Earth and Planetary Science Letters* 128: 327–339. https://doi.org/10.1016/0012-821X(94)90154-6.

Brooks, H. L., B. Dragovic, H. M. Lamadrid, M. J. Caddick, and R. J. Bodnar. 2019. "Fluid Capture During Exhumation of Subducted Lithologies: A Fluid Inclusion Study From Sifnos, Greece." *Lithos* 332–333: 120–134. https://doi.org/10.1016/j.lithos.2019.01.014.

Bucher, K., Y. Fazis, C. De Capitani, and R. Grapes. 2005. "Blueschists, Eclogites, and Decompression Assemblages of the Zermatt-Saas Ophiolite: High-Pressure Metamorphism of Subducted Tethys Lithosphere." *American Mineralogist* 90: 821–835. https://doi.org/10.2138/am.2005.1718.

Busigny, V., P. Cartigny, P. Philippot, M. Ader, and M. Javoy. 2003. "Massive Recycling of Nitrogen and Other Fluid-Mobile Elements (K, Rb, Cs, H) in a Cold Slab Environment: Evidence From HP to UHP Oceanic Metasediments of the Schistes Lustrés Nappe (Western Alps, Europe)." *Earth and Planetary Science Letters* 215: 27–42. https://doi.org/10.1016/S0012-821X(03)00453-9.

Busigny, V., P. Cartigny, and P. Philippot. 2011. "Nitrogen Isotopes in Ophiolitic Metagabbros: A Re-Evaluation of Modern Nitrogen Fluxes in Subduction Zones and Implication for the Early Earth Atmosphere." *Geochimica et Cosmochimica Acta* 75: 7502–7521. https://doi.org/10.1016/j.gca.2011.09.049.

Busigny, V., J. Chen, P. Philippot, S. Borensztajn, and F. Moynier. 2018. "Insight Into Hydrothermal and Subduction Processes From Copper and Nitrogen Isotopes in Oceanic Metagabbros." *Earth and Planetary Science Letters* 498: 54–64. https://doi.org/10.1016/j.epsl.2018.06.030.

Cannaò, E., M. Scambelluri, O. Müntener, B. Putlitz, and S. Agostini. 2023. "Inheritance Versus Subduction-Related δ11B Signatures of Eclogites: Insights From the Voltri Massif (Ligurian Western Alps, Italy)." *Chemical Geology* 615: 121218. https://doi.org/10.1016/j.chemgeo.2022.121218.

Caumon, M.-C., J. Dubessy, P. Robert, and A. Tarantola. 2013. "Fused-Silica Capillary Capsules (FSCCs) as Reference Synthetic Aqueous Fluid Inclusions to Determine Chlorinity by Raman Spectroscopy." *ejm* 25: 755–763. https://doi.org/10.1127/0935-1221/2013/0025-2280.

Caurant, C., B. Debret, B. Ménez, C. Nicollet, and P. Bouilhol. 2023. "Redox Heterogeneities in a Subducting Slab: Example From the Monviso Meta-Ophiolite (Western Alps, Italy)." *Lithos* 446–447: 107136. https://doi.org/10.1016/j.lithos.2023.107136.

Cerchiari, A., F. Remitti, S. Mittempergher, A. Festa, F. Lugli, and A. Cipriani. 2020. "Cyclical Variations of Fluid Sources and Stress State in a Shallow Megathrust-Zone mélange." *Journal of the Geological Society* 177: 647–659. https://doi.org/10.1144/jgs2019-072.

Chopin, C. 1984. "Coesite and Pure Pyrope in High-Grade Blueschists of the Western Alps: A First Record and Some Consequences." *Contr. Mineral. and Petrol.* 86: 107–118. https://doi.org/10.1007/BF00381838.

Claoué-Long, J. C., W. Compston, J. Roberts, and C. M. Fanning. 1995. "Two Carboniferous Ages: A Comparison of SHRIMP Zircon Dating With Conventional Zircon Ages and $^{40}Ar/^{39}Ar$ Analysis." In *Geochronology, Time Scales and Global Stratigraphic Correlation*, edited by W. A. Bergrenn, D. V. Kent, M. P. Aubry, and J. Hardenbol, vol. 54, 1–21. Society for Sedimentary Geology Special Publication.

Compagnoni, R., and F. Rolfo. 2003. "UHPM Units in the Western Alps." In *Ultrahigh Pressure Metamorphism*, edited by G. Papp, T. G. Weiszburg, D. A. Carswell, R. Compagnoni, and F. Rolfo, 13–49. Budapest: Mineralogical Society of Great Britain and Ireland. https://doi.org/10.1180/EMU-notes.5.2.

Connolly, J. A. D. 1990. "Multivariable Phase Diagrams: An Algorithm Based on Generalized Thermodynamics." *American Journal of Science* 290: 666–718.

Connolly, J. A. D. 2005. "Computation of Phase Equilibria by Linear Programming: A Tool for Geodynamic Modeling and Its Application to Subduction Zone Decarbonation." *Earth and Planetary Science Letters* 236: 524–541. https://doi.org/10.1016/j.epsl.2005.04.033.

Connolly, J. A. D. 2009. "The Geodynamic Equation of State: What and How." *Geochemistry, Geophysics, Geosystems* 10: n/a–n/a. https://doi.org/10.1029/2009GC002540.

De Togni, M., G. Balestro, D. Rubatto, D. Castelli, M. Gattiglio, and A. Festa. 2024. "Late Jurassic Magmatism in the Ligurian-Piedmont Ocean Constrained by Zircon Ages of Mafic and Felsic Meta-Intrusives." *Terra Nova* 36: 403–413. https://doi.org/10.1111/ter.12723.

Debret, B., K. T. Koga, F. Cattani, C. Nicollet, G. Van den Bleeken, and S. Schwartz. 2016. "Volatile (Li, B, F and Cl) Mobility During Amphibole Breakdown in Subduction Zones." *Lithos* 244: 165–181. https://doi.org/10.1016/j.lithos.2015.12.004.

Debret, B., P. Bouilhol, M. L. Pons, and H. Williams. 2018. "Carbonate Transfer During the Onset of Slab Devolatilization: New Insights From Fe and Zn Stable Isotopes." *Journal of Petrology* 59: 1145–1166. https://doi.org/10.1093/petrology/egy057.

Decrausaz, T., O. Müntener, P. Manzotti, R. Lafay, and C. Spandler. 2021. "Fossil Oceanic Core Complexes in the Alps. New Field, Geochemical and Isotopic Constraints From the Tethyan Aiguilles Rouges Ophiolite (Val d'Hérens, Western Alps, Switzerland)." *Swiss Journal of Geosciences* 114: 3. https://doi.org/10.1186/s00015-020-00380-4.

Deville, E., S. Fudral, Y. Lagabrielle, M. Marthaler, and M. Sartori. 1992. "From Oceanic Closure to Continental Collision: A Synthesis of the "Schistes lustrés" Metamorphic Complex of the Western Alps." *Geological Society of America Bulletin* 104: 127–139.

Diamond, L. W., and A. Tarantola. 2015. "Interpretation of Fluid Inclusions in Quartz Deformed by Weak Ductile Shearing: Reconstruction of Differential Stress Magnitudes and Pre-Deformation Fluid Properties." *Earth and Planetary Science Letters* 417: 107–119. https://doi.org/10.1016/j.epsl.2015.02.019.

Diamond, L. W., A. Tarantola, and H. Stünitz. 2010. "Modification of Fluid Inclusions in Quartz by Deviatoric Stress. II: Experimentally Induced Changes in Inclusion Volume and Composition." *Contributions to Mineralogy and Petrology* 160: 845–864. https://doi.org/10.1007/s00410-010-0510-6.

Diener, J. F. A., R. Powell, R. W. White, and T. J. B. Holland. 2007. "A New Thermodynamic Model for Clino- and Orthoamphiboles in the System

Na2O-CaO-FeO-MgO-Al2O3-SiO2-H2O." *Journal of Metamorphic Geology* 25: 631–656. https://doi.org/10.1111/j.1525-1314.2007.00720.x.

Dowty, E. 1976. "Crystal Structure and Crystal Growth: II. Sector Zoning in Minerals." *American Mineralogist* 61: 460–469.

Dragovic, B., S. Angiboust, and M. J. Tappa. 2020. "Petrochronological Close-Up on the Thermal Structure of a Paleo-Subduction Zone (W. Alps)." *Earth and Planetary Science Letters* 547: 116446. https://doi.org/10.1016/j.epsl.2020.116446.

Droop, G. T. R. 1987. "A General Equation for Estimating Fe^{3+} Concentrations in Ferromagnesian Silicates and Oxides From Microprobe Analyses, Using Stoichiometric Criteria." *Mineralogical Magazine* 51: 431–435. https://doi.org/10.1180/minmag.1987.051.361.10.

El-Shazly, A. K., and V. B. Sisson. 1999. "Retrograde Evolution of Eclogite Facies Rocks From NE Oman: Evidence From Fluid Inclusions and Petrological Data." *Chemical Geology* 154: 193–223. https://doi.org/10.1016/S0009-2541(98)00132-6.

Epstein, G. S., G. E. Bebout, S. Angiboust, and P. Agard. 2020. "Scales of Fluid-Rock Interaction and Carbon Mobility in the Deeply Underplated and HP-Metamorphosed Schistes Lustrés, Western Alps." *Lithos* 354–355: 105229. https://doi.org/10.1016/j.lithos.2019.105229.

Epstein, G. S., G. E. Bebout, and S. Angiboust. 2021. "Fluid and Mass Transfer Along Transient Subduction Interfaces in a Deep Paleo-Accretionary Wedge (Western Alps)." *Chemical Geology* 559: 119920. https://doi.org/10.1016/j.chemgeo.2020.119920.

Evans, B. W. 1990. "Phase Relations of Epidote-Blueschists." *Lithos* 25: 3–23.

Fagereng, Å. 2011. "Fractal Vein Distributions Within a Fault-Fracture Mesh in an Exhumed Accretionary mélange, Chrystalls Beach Complex, New Zealand." *Journal of Structural Geology* 33: 918–927. https://doi.org/10.1016/j.jsg.2011.02.009.

Fermi, E. 1931. "Über den ramaneffekt des kohlendioxyds." *Zeitschrift für Physik* 71, no. 3–4: 250–259. https://doi.org/10.1007/bf01341712.

Ferrando, S., M. L. Frezzotti, P. Orione, R. Carlo, and R. Compagnoni. 2010. "Late-Alpine Rodingitization in the Bellecombe Meta-Ophiolites (Aosta Valley, Italian Western Alps): Evidence From Mineral Assemblages and Serpentinization-Derived H2-Bearing Brine." *International Geology Review* 52: 1220–1243.

Fisher, D. M., S. L. Brantley, M. Everett, and J. Dzvonik. 1995. "Cyclic Fluid Flow Through a Regionally Extensive Fracture Network Within the Kodiak Accretionary Prism." *Journal of Geophysical Research* 100: 12881–12894. https://doi.org/10.1029/94JB02816.

Frezzotti, M. L., and S. Ferrando. 2015. "The Chemical Behavior of Fluids Released During Deep Subduction Based on Fluid Inclusions." *American Mineralogist* 100: 352–377. https://doi.org/10.2138/am-2015-4933.

Frezzotti, M. L., F. Tecce, and A. Casagli. 2012. "Raman Spectroscopy for Fluid Inclusion Analysis." *Journal of Geochemical Exploration* 112: 1–20. https://doi.org/10.1016/j.gexplo.2011.09.009.

Fudral, S. 1996. "Etude Géologique de la Suture Tethysienne Dans les Alpes Franco-Italiennes Nord-Occidentales de la Doire Ripaire (Italie) à la Région de Bourg Saint-Maurice." PhD thesis, Université de Savoie.

Fuhrman, M. L., and D. H. Lindsley. 1988. "Ternary-Feldspar Modeling and Thermometry." *American Mineralogist* 73: 201–215.

Gabalda, S., O. Beyssac, L. Jolivet, P. Agard, and C. Chopin. 2009. "Thermal Structure of a Fossil Subduction Wedge in the Western Alps." *Terra Nova* 21: 28–34. https://doi.org/10.1111/j.1365-3121.2008.00849.x.

Garber, J. M., A. J. Smye, M. D. Feineman, A. R. C. Kylander-Clark, and S. Matthews. 2020. "Decoupling of Zircon U–Pb and Trace-Element Systematics Driven by U Diffusion in Eclogite-Facies Zircon (Monviso Meta-Ophiolite, W. Alps)." *Contributions to Mineralogy and Petrology* 175: 55. https://doi.org/10.1007/s00410-020-01692-2.

Ghignone, S., A. Borghi, G. Balestro, D. Castelli, M. Gattiglio, and C. Groppo. 2021a. "HP Tectono-Metamorphic Evolution of the Internal Piedmont Zone in Susa Valley (Western Alps): New Petrologic Insight From Garnet+Chloritoid-Bearing Micaschists and Fe–Ti Metagabbro." *Journal of Metamorphic Geology* 39: 391–416.

Ghignone, S., M. Sudo, G. Balestro, et al. 2021b. "Timing of Exhumation of Meta-Ophiolite Units in the Western Alps: New Tectonic Implications From $^{40}Ar/^{39}Ar$ White Mica Ages From Piedmont Zone (Susa Valley)." *Lithos* 404–405: 106443. https://doi.org/10.1016/j.lithos.2021.106443.

Ghignone, S., E. Scaramuzzo, M. Bruno, and F. A. Livio. 2023. "A New UHP Unit in the Western Alps: First Occurrence of Coesite From the Monviso Massif (Italy)." *American Mineralogist* 108: 1368–1375. https://doi.org/10.2138/am-2022-8621.

Ghignone, S., M. Gilio, A. Borghini, F. Boero, M. Bruno, and E. Scaramuzzo. 2024. "Mineralogical and Petrological Constraints and Tectonic Implications of a New Coesite-Bearing Unit From the Alpine Tethys Oceanic Slab (Susa Valley, Western Alps)." *Lithos* 472: 107575.

Gilio, M., M. Scambelluri, S. Agostini, et al. 2020. "Fingerprinting and Relocating Tectonic Slices Along the Plate Interface: Evidence From the Lago Superiore Unit at Monviso (Western Alps)." *Lithos* 352: 105308.

Green, E., T. Holland, and R. Powell. 2007. "An Order-Disorder Model for Omphacitic Pyroxenes in the System Jadeite-Diopside-Hedenbergite-Acmite, With Applications to Eclogitic Rocks." *American Mineralogist* 92: 1181–1189. https://doi.org/10.2138/am.2007.2401.

Groppo, C., and D. Castelli. 2010. "Prograde P–T Evolution of a Lawsonite Eclogite from the Monviso Meta-Ophiolite (Western Alps): Dehydration and Redox Reactions During Subduction of Oceanic FeTi-oxide Gabbro." *Journal of Petrology* 51: 2489–2514. https://doi.org/10.1093/petrology/egq065.

Groppo, C., M. Beltrando, and R. Compagnoni. 2009. "The P-T Path of the Ultra-High Pressure Lago Di Cignana and Adjoining High-Pressure Meta-Ophiolitic Units: Insights Into the Evolution of the Subducting Tethyan Slab." *Journal of Metamorphic Geology* 27: 207–231. https://doi.org/10.1111/j.1525-1314.2009.00814.x.

Guillot, S., K. Hattori, P. Agard, S. Schwartz, and O. Vidal. 2009. "Exhumation Processes in Oceanic and Continental Subduction Contexts: A Review." In *Subduction Zone Geodynamics, Frontiers in Earth Sciences*, edited by S. Lallemand and F. Funiciello, 175–205. Berlin, Heidelberg: Springer Berlin Heidelberg. https://doi.org/10.1007/978-3-540-87974-9_10.

Gyomlai, T., P. Agard, H. R. Marschall, L. Jolivet, and A. Gerdes. 2021. "Metasomatism and Deformation of Block-In-Matrix Structures in Syros: The Role of Inheritance and Fluid-Rock Interactions Along the Subduction Interface." *Lithos* 386–387: 105996. https://doi.org/10.1016/j.lithos.2021.105996.

Gyomlai, T., P. Agard, C. Herviou, et al. 2023. "In Situ Rb–Sr and ^{40}Ar–^{39}Ar Dating of Distinct Mica Generations in the Exhumed Subduction Complex of the Western Alps." *Contributions to Mineralogy and Petrology* 178: 58. https://doi.org/10.1007/s00410-023-02042-8.

Hacker, B. R., S. M. Peacock, G. A. Abers, and S. D. Holloway. 2003. "Subduction Factory 2. Are Intermediate-Depth Earthquakes in Subducting Slabs Linked to Metamorphic Dehydration Reactions?" *Journal of Geophysical Research* 108: 1–16. https://doi.org/10.1029/2001JB001129.

Halama, R., and G. Bebout. 2021. "Earth's Nitrogen and Carbon Cycles." *Space Science Reviews* 217, no. 3: 45.

Halama, R., G. E. Bebout, H. R. Marschall, and T. John. 2017. "Fluid-Induced Breakdown of White Mica Controls Nitrogen Transfer During Fluid–Rock Interaction in Subduction Zones." *International Geology Review* 59, no. 5-6: 702–720.

Handy, M. R., S. M. Schmid, R. Bousquet, E. Kissling, and D. Bernoulli. 2010. "Reconciling Plate-Tectonic Reconstructions of Alpine Tethys

With the Geological–Geophysical Record of Spreading and Subduction in the Alps." *Earth-Science Reviews* 102: 121–158.

Hawthorne, F. C., R. Oberti, G. E. Harlow, et al. 2012. "IMA Report: Nomenclature of the Amphibole Supergroup." *American Mineralogist* 97: 2031–2048. https://doi.org/10.2138/am.2012.4276.

Hay, W. W., A. Migdisov, A. N. Balukhovsky, C. N. Wold, S. Flögel, and E. Söding. 2006. "Evaporites and the Salinity of the Ocean During the Phanerozoic: Implications for Climate, Ocean Circulation and Life." *Palaeogeography, Palaeoclimatology, Palaeoecology* 240: 3–46. https://doi.org/10.1016/j.palaeo.2006.03.044.

Hellstrom, J., C. Paton, J. D. Woodhead, and J. Hergt. 2008. "Iolite: Software for Spatially Resolved LA-(Quad and MC) ICPMS Analysis." *Mineralogical Association of Canada Short Course Series* 40: 343–348.

Henry, C., M. Burkhard, and B. Goffé. 1996. "Evolution of Synmetamorphic Veins and Their Wallrocks Through a Western Alps Transect: No Evidence for Large-Scale Fluid Flow. Stable Isotope, Major- and Trace-Element Systematics." *Chemical Geology* 127: 81–109. https://doi.org/10.1016/0009-2541(95)00106-9.

Hertgen, S., P. Yamato, L. F. G. Morales, and S. Angiboust. 2017. "Evidence for Brittle Deformation Events at Eclogite-Facies P-T Conditions (Example of the Mt. Emilius Klippe, Western Alps)." *Tectonophysics* 706–707: 1–13. https://doi.org/10.1016/j.tecto.2017.03.028.

Herviou, C., and G. Bonnet. 2023. "Paleocene-Eocene High-Pressure Carbonation of Western Alps Serpentinites: Positive Feedback Between Deformation and CO_2-CH_4 Fluid Ingression Responsible for Slab Slicing?" *Geochemistry, Geophysics, Geosystems* 24: e2022GC010557. https://doi.org/10.1029/2022GC010557.

Herviou, C., A. Verlaguet, P. Agard, et al. 2021. "Along-Dip Variations of Subduction Fluids: The 30–80 km Depth Traverse of the Schistes Lustrés Complex (Queyras-Monviso, W. Alps)." *Lithos* 394–395: 106168. https://doi.org/10.1016/j.lithos.2021.106168.

Herviou, C., P. Agard, A. Plunder, et al. 2022. "Subducted Fragments of the Liguro-Piemont Ocean, Western Alps: Spatial Correlations and Offscraping Mechanisms During Subduction." *Tectonophysics* 827: 229267. https://doi.org/10.1016/j.tecto.2022.229267.

Herviou, C., P. Agard, A. Verlaguet, et al. 2023. "Fractal Distribution of Subduction-Related Crack-Seal Veins (Schistes Lustrés, W. Alps): Implications for Fluid Flow and Rupture Processes at the Downdip End of the Seismogenic Zone." *JGR Solid Earth* 128: e2022JB026317. https://doi.org/10.1029/2022JB026317.

Holland, T., and R. Powell. 1991. "A Compensated-Redlich-Kwong (CORK) Equation for Volumes and Fugacities of CO_2 and H_2O in the Range 1 bar to 50 kbar and I00°C–1600°C." *Contributions to Mineralogy and Petrology* 109: 265–273.

Holland, T. J. B., and R. Powell. 1998. "An Internally Consistent Thermodynamic Data set for Phases of Petrological Interest." *Journal of Metamorphic Geology* 16: 309–343. https://doi.org/10.1111/j.1525-1314.1998.00140.x.

Holland, T., J. Baker, and R. Powell. 1998. "Mixing Properties and Activity-Composition Relationships of Chlorites in the System MgO-FeO-Al2O3-SiO2-H2O." *Ejm* 10: 395–406. https://doi.org/10.1127/ejm/10/3/0395.

Hoover, W. F., S. Penniston-Dorland, P. Piccoli, and A. Kylander-Clark. 2023. "Reaction-Induced Porosity in an Eclogite-Facies Vein Selvage (Monviso Ophiolite, W. Alps): Textural Evidence and In Situ Trace Elements and Sr Isotopes in Apatite." *Journal of Petrology* 64: egac128. https://doi.org/10.1093/petrology/egac128.

Horstwood, M. S. A., J. Kosler, G. Gehrels, et al. 2016. "Community-Derived Standards for LA-ICP-MS U-(Th-)Pb Geochronology—Uncertainty Propagation, Age Interpretation and Data Reporting." *Geostandards and Geoanalytical Research* 40: 311–332.

Hyppolito, T., A. Cambeses, S. Angiboust, T. Raimondo, A. García-Casco, and C. Juliani. 2019. "Rehydration of Eclogites and Garnet-Replacement Processes During Exhumation in the Amphibolite Facies." *Geological Society, London, Special Publications* 478, no. 1: 217–239. https://doi.org/10.1144/SP478.3.

Inglis, E. C., B. Debret, K. W. Burton, et al. 2017. "The Behavior of Iron and Zinc Stable Isotopes Accompanying the Subduction of Mafic Oceanic Crust: A Case Study From Western Alpine Ophiolites." *Geochemistry, Geophysics, Geosystems* 18: 2562–2579. https://doi.org/10.1002/2016GC006735.

Jaeckel, K., G. E. Bebout, and S. Angiboust. 2018. "Deformation-Enhanced Fluid and Mass Transfer Along Western and Central Alps Paleo-Subduction Interfaces: Significance for Carbon Cycling Models." *Geosphere* 14: 2355–2375. https://doi.org/10.1130/GES01587.1.

Jochum, K. P., U. Weis, B. Stoll, et al. 2011a. "Determination of Reference Values for NIST SRM 610–617 Glasses Following ISO Guidelines." *Geostandards and Geoanalytical Research* 35: 397–429. https://doi.org/10.1111/j.1751-908X.2011.00120.x.

Jochum, K. P., S. A. Wilson, W. Abouchami, et al. 2011b. "GSD-1G and MPI-DING Reference Glasses for In Situ and Bulk Isotopic Determination." *Geostandards and Geoanalytical Research* 35: 193–226.

John, T., N. Gussone, Y. Y. Podladchikov, et al. 2012. "Volcanic Arcs Fed by Rapid Pulsed Fluid Flow Through Subducting Slabs." *Nature Geoscience* 5: 489–492.

van Keken, P. E., B. R. Hacker, E. M. Syracuse, and G. A. Abers. 2011. "Subduction Factory: 4. Depth-Dependent Flux of H 2 O From Subducting Slabs Worldwide." *Journal of Geophysical Research* 116: B01401. https://doi.org/10.1029/2010JB007922.

Kelley, D. S., and J. R. Delaney. 1987. "Two-Phase Separation and Fracturing in Mid-Ocean Ridge Gabbros at Temperatures Greater Than 700°C." *Earth and Planetary Science Letters* 83: 53–66. https://doi.org/10.1016/0012-821X(87)90050-1.

Kelley, D. S., P. T. Robinson, and J. G. Malpas. 1992. "Processes of Brine Generation and Circulation in the Oceanic Crust: Fluid Inclusion Evidence From the Troodos Ophiolite, Cyprus." *Journal of Geophysical Research* 97: 9307–9322. https://doi.org/10.1029/92JB00520.

Kendrick, M. A., M. Scambelluri, M. Honda, and D. Phillips. 2011. "High Abundances of Noble Gas and Chlorine Delivered to the Mantle by Serpentinite Subduction." *Nature Geoscience* 4: 807–812. https://doi.org/10.1038/ngeo1270.

Kita, S., T. Okada, J. Nakajima, T. Matsuzawa, and A. Hasegawa. 2006. "Existence of a Seismic Belt in the Upper Plane of the Double Seismic Zone Extending in the Along-Arc Direction at Depths of 70–100 km Beneath NE Japan." *Geophysical Research Letters* 33: 2006GL028239. https://doi.org/10.1029/2006GL028239.

Klemd, R., A. M. Van den Kerkhof, and E. E. Horn. 1992. "High-Density CO_2-N_2 Inclusions in Eclogite-Facies Metasediments of the Mfinchberg Gneiss Complex, SE Germany." *Contributions to Mineralogy and Petrology* 111: 409–419.

Kylander-Clark, A. R. C., B. R. Hacker, and J. M. Cottle. 2013. "Laser-Ablation Split-Stream ICP Petrochronology." *Chemical Geology* 345: 99–112. https://doi.org/10.1016/j.chemgeo.2013.02.019.

Lagabrielle, Y. 1987. "Les Ophiolites: Marqueurs de L'histoire Tectonique des Domaines Océaniques." PhD thesis, Université de Bretagne Occidentale.

Lagabrielle, Y., and M. Cannat. 1990. "Alpine Jurassic Ophiolites Resemble the Modern Central Atlantic Basement." *Geology* 18: 319–322.

Lagabrielle, Y., and R. Polino. 1985. "Origine Volcano-Détritique de Certaines Prasinites des Schistes Lustrés du Queyras (France); Arguments Texturaux et Géochimiques." *Bulletin de la Societe Geologique de France* 1: 461–471.

Lagabrielle, Y., A. Vitale Brovarone, and B. Ildefonse. 2015. "Fossil Oceanic Core Complexes Recognized in the Blueschist Metaophiolites of Western Alps and Corsica." *Earth-Science Reviews* 141: 1–26. https://doi.org/10.1016/j.earscirev.2014.11.004.

Lefeuvre, B., B. Dubacq, A. Verlaguet, et al. 2024. "Disentangling the Compositional Variations of Lawsonite in Blueschist-Facies Metasediments (Schistes Lustrés, W. Alps)." *Contributions to Mineralogy and Petrology* 179: 25.

Lemoine, M. 2003. "Schistes Lustrés From Corsica to Hungary: Back to the Original Sediments and Tentative Dating of Partly Azoic Metasediments." *Bulletin de la Société Géologique de France* 174: 197–209. https://doi.org/10.2113/174.3.197.

Lemoine, M., and P. Tricart. 1986. "Les Schistes Lustrés Piémontais des Alpes Occidentales: Approche Stratigraphique, Structurales et Sédimentologique." *Eclogae Geologicae Helvetiae* 79: 271–294. https://doi.org/10.5169/SEALS-165835.

Li, X.-H., M. Faure, W. Lin, and G. Manatschal. 2013. "New Isotopic Constraints on Age and Magma Genesis of an Embryonic Oceanic Crust: The Chenaillet Ophiolite in the Western Alps." *Lithos* 160–161: 283–291. https://doi.org/10.1016/j.lithos.2012.12.016.

Locatelli, M., A. Verlaguet, P. Agard, L. Federico, and S. Angiboust. 2018. "Intermediate-Depth Brecciation Along the Subduction Plate Interface (Monviso Eclogite, W. Alps)." *Lithos* 320–321: 378–402. https://doi.org/10.1016/j.lithos.2018.09.028.

Locatelli, M., A. Verlaguet, P. Agard, T. Pettke, and L. Federico. 2019. "Fluid Pulses During Stepwise Brecciation at Intermediate Subduction Depths (Monviso Eclogites, W. Alps): First Internally Then Externally Sourced." *Geochemistry, Geophysics, Geosystems* 20: 5285–5318. https://doi.org/10.1029/2019GC008549.

Ludwig, K. 2009. "SQUID 2 (Rev. 2.50), A User's Manual." Berkeley Geochronology Center Special Publication 5, 110.

Malatesta, C., L. Federico, L. Crispini, and G. Capponi. 2018. "Fluid-Controlled Deformation in Blueschist-Facies Conditions: Plastic vs Brittle Behaviour in a Brecciated Mylonite (Voltri Massif, Western Alps, Italy)." *Geological Magazine* 155: 335–355.

Manatschal, G., and O. Müntener. 2009. "A Type Sequence Across an Ancient Magma-Poor Ocean–Continent Transition: The Example of the Western Alpine Tethys Ophiolites." *Tectonophysics* 473: 4–19. https://doi.org/10.1016/j.tecto.2008.07.021.

Martin, C., K. E. Flores, A. Vitale-Brovarone, S. Angiboust, and G. E. Harlow. 2020. "Deep Mantle Serpentinization in Subduction Zones: Insight From In Situ B Isotopes in Slab and Mantle Wedge Serpentinites." *Chemical Geology* 545: 119637. https://doi.org/10.1016/j.chemgeo.2020.119637.

Maruyama, S., J. G. Liou, and M. Terabayashi. 1996. "Blueschists and Eclogites of the World and Their Exhumation." *International Geology Review* 38: 485–594. https://doi.org/10.1080/00206819709465347.

Mendes, K., P. Agard, A. Plunder, and C. Herviou. 2023. "Lithospheric-Scale Dynamics During Continental Subduction: Evidence From a Frozen-In Plate Interface." *Geology* 51: 1153–1157. https://doi.org/10.1130/G51480.1.

Mukherjee, B. K., and H. K. Sachan. 2009. "Fluids in Coesite-Bearing Rocks of the Tso Morari Complex, NW Himalaya: Evidence for Entrapment During Peak Metamorphism and Subsequent Uplift." *Geological Magazine* 146: 876–889. https://doi.org/10.1017/S0016756809990069.

Muñoz-Montecinos, J., S. Angiboust, A. Cambeses, and A. García-Casco. 2020. "Multiple Veining in a Paleo–Accretionary Wedge: The Metamorphic Rock Record of Prograde Dehydration and Transient High Pore-Fluid Pressures Along the Subduction Interface (Western Series, Central Chile)." *Geosphere* 16: 765–786. https://doi.org/10.1130/GES02227.1.

Muñoz-Montecinos, J., S. Angiboust, A. Garcia-Casco, and T. Raimondo. 2023. "Shattered Veins Elucidate Brittle Creep Processes in the Deep Slow Slip and Tremor Region." *Tectonics* 42: e2022TC007605.

Nadeau, S., P. Philippot, and F. Pineau. 1993. "Fluid Inclusion and Mineral Isotopic Compositions (HCO) in Eclogitic Rocks as Tracers of Local Fluid Migration During High-Pressure Metamorphism." *Earth and Planetary Science Letters* 114: 431–448. https://doi.org/10.1016/0012-821X(93)90074-J.

Nishiyama, N., K. Ujiie, K. Noro, Y. Mori, and H. Masuyama. 2023. "Megathrust Slip Enhanced by Metasomatic Actinolite in the Source Region of Deep Slow Slip." *Lithos* 446–447: 107115. https://doi.org/10.1016/j.lithos.2023.107115.

Oliver, N. H. S., and P. D. Bons. 2001. "Mechanisms of Fluid Flow and Fluid-Rock Interaction in Fossil Metamorphic Hydrothermal Systems Inferred From Vein-Wallrock Patterns, Geometry and Microstructure." *Geofluids* 1: 137–162. https://doi.org/10.1046/j.1468-8123.2001.00013.x.

Otsuki, M., and S. Banno. 1990. "Prograde and Retrograde Metamorphism of Hematitebearing Basic Schists in the Sanbagawa Belt in Central Shikoku." *Journal of Metamorphic Geology* 8: 425–439. https://doi.org/10.1111/j.1525-1314.1990.tb00629.x.

Paton, C., J. Hellstrom, B. Paul, J. Woodhead, and J. Hergt. 2011. "Iolite: Freeware for the Visualisation and Processing of Mass Spectrometric Data." *Journal of Analytical Atomic Spectrometry* 26: 2508. https://doi.org/10.1039/c1ja10172b.

Peacock, S. M., and K. Wang. 2021. "On the Stability of Talc in Subduction Zones: A Possible Control on the Maximum Depth of Decoupling Between the Subducting Plate and Mantle Wedge." *Geophysical Research Letters* 48: e2021GL094889. https://doi.org/10.1029/2021GL094889.

Pearce, N. J. G., W. T. Perkins, J. A. Westgate, et al. 1997. "A Compilation of New and Published Major and Trace Element Data for NIST SRM 610 and NIST SRM 612 Glass Reference Materials." *Geostandards and Geoanalytical Research* 21: 115–144.

Philippot, P. 1987. ""Crack Seal" Vein Geometry in Eclogitic Rocks." *Geodinamica Acta* 1: 171–181.

Philippot, P. 1990. "Opposite Vergence of Nappes and Crustal Extension in the French-Italian Western Alps." *Tectonics* 9: 1143–1164. https://doi.org/10.1029/TC009i005p01143.

Philippot, P., and J.-R. Kienast. 1989. "Chemical-Microstructural Changes in Eclogite-Facies Shear Zones (Monviso, Western Alps, North Italy) as Indicators of Strain History and the Mechanism and Scale of Mass Transfer." *Lithos* 23: 179–200. https://doi.org/10.1016/0024-4937(89)90004-2.

Philippot, P., and J. Selverstone. 1991. "Trace-Element-Rich Brines in Eclogitic Veins: Implications for Fluid Composition and Transport During Subduction." *Contr. Mineral. And Petrol.* 106: 417–430. https://doi.org/10.1007/BF00321985.

Philippot, P., and H. L. M. Van Roermund. 1992. "Deformation Processes in Eclogitic Rocks: Evidence for the Rheological Delamination of the Oceanic Crust in Deeper Levels of Subduction Zones." *Journal of Structural Geology* 14: 1059–1077. https://doi.org/10.1016/0191-8141(92)90036-V.

Philippot, P., P. Agrinier, and M. Scambelluri. 1998. "Chlorine Cycling During Subduction of Altered Oceanic Crust." *Earth and Planetary Science Letters* 12: 33–44.

Philippot, P., V. Busigny, M. Scambelluri, and P. Cartigny. 2007. "Oxygen and Nitrogen Isotopes as Tracers of Fluid Activities in Serpentinites and Metasediments During Subduction." *Mineralogy and Petrology* 91: 11–24. https://doi.org/10.1007/s00710-007-0183-7.

Platt, J. P., D. Grujic, N. J. Phillips, S. Piazolo, and D. A. Schmidt. 2024. "Geological Fingerprints of Deep Slow Earthquakes: A Review of Field Constraints and Directions for Future Research." *Geosphere* 20: 981–1004.

Plunder, A., P. Agard, B. Dubacq, C. Chopin, and M. Bellanger. 2012. "How Continuous and Precise Is the Record of P-T Paths? Insights From Combined Thermobarometry and Thermodynamic Modelling Into Subduction Dynamics (Schistes Lustrés, W. Alps): Towards Continuous P-T PATHS?" *Journal of Metamorphic Geology* 30: 323–346. https://doi.org/10.1111/j.1525-1314.2011.00969.x.

Plunder, A., P. Agard, C. Chopin, A. Pourteau, and A. I. Okay. 2015. "Accretion, Underplating and Exhumation Along a Subduction Interface: From Subduction Initiation to Continental Subduction (Tavşanlı Zone, W. Turkey)." *Lithos* 226: 233–254. https://doi.org/10.1016/j.lithos.2015.01.007.

Pognante, U. 1979. "The Osiera-Rocciavre Metaophiolitic Complex (Italian Western Alps)." *Ofioliti* 4: 183–198.

Pognante, U. 1981. "Magmatic and Metamorphic Evolution of Two Fe-Ti Gabbroic Series From the Piemonte Ophiolite Nappe in the Susa Valley Area, Italian Western Alps." *Mem. Sci. Geol. Padova* 35: 21–34.

Pognante, U. 1984. "Eclogitic Versus Blueschist Metamorphism in the Internal Western Alps Along the Susa Valley Traverse." *sgeol* 37: 29–36. https://doi.org/10.3406/sgeol.1984.1650.

Pognante, U. 1985. "Coronitic Reactions and Ductile Shear Zones in Eclogitised Ophiolite Metagabbro, Western Alps, North Italy." *Chemical Geology* 50: 99–109. https://doi.org/10.1016/0009-2541(85)90114-7.

Pognante, U. 1991. "Petrological Constraints on the Eclogite- and Blueschistfacies Metamorphism and P-T-t Paths in the Western Alps*." *Journal of Metamorphic Geology* 9: 5–17. https://doi.org/10.1111/j.1525-1314.1991.tb00501.x.

Pognante, U., and J.-R. Kienast. 1987. "Blueschist and Eclogite Transformations in Fe-Ti Gabbros: A Case From the Western Alps Ophiolites." *Journal of Petrology* 28: 271–292. https://doi.org/10.1093/petrology/28.2.271.

Pognante, U., and L. Toscani. 1985. "Geochemistry of Basaltic and Gabbroid Metaophiolites From the Susa Valley, Italian Western Alps." *Schweizerische Mineralogische und Petrographische Mitteilungen* 65: 265–277. https://doi.org/10.5169/SEALS-50224.

Pognante, U., B. Lombardo, and G. Venturelli. 1982. "Petrology and Geochemistry of Fe-Ti Gabbros and Plagiogranites From the Western Alps Ophiolites." *Schweizerische Mineralogische und Petrographische Mitteilungen* 62: 457–472. https://doi.org/10.5169/SEALS-47981.

Raimbourg, H., V. Famin, G. Palazzin, et al. 2018. "Fluid Properties and Dynamics Along the Seismogenic Plate Interface." *Geosphere* 14: 469–491. https://doi.org/10.1130/GES01504.1.

Raimondo, T., J. Payne, B. Wade, P. Lanari, C. Clark, and M. Hand. 2017. "Trace Element Mapping by LA-ICP-MS: Assessing Geochemical Mobility in Garnet." *Contributions to Mineralogy and Petrology* 172: 17. https://doi.org/10.1007/s00410-017-1339-z.

Rajič, K., H. Raimbourg, C. Lerouge, et al. 2023a. "Metamorphic Reactions and Their Implication for the Fluid Budget in Metapelites at Seismogenic Depths in Subduction Zones." *Tectonophysics* 857: 229844. https://doi.org/10.1016/j.tecto.2023.229844.

Rajič, K., H. Raimbourg, V. Famin, et al. 2023b. "Exhuming an Accretionary Prism: A Case Study of the Kodiak Accretionary Complex, Alaska, USA." *Tectonics* 42: e2023TC007754. https://doi.org/10.1029/2023TC007754.

Reinecke, T. 1991. "Very-High-Pressure Metamorphism and Uplift of Coesite-Bearing Metasediments From the Zermatt-Saas Zone, Western Alps." *Ejm* 3: 7–18. https://doi.org/10.1127/ejm/3/1/0007.

Reinecke, T. 1998. "Prograde High- To Ultrahigh-Pressure Metamorphism and Exhumation of Oceanic Sediments at Lago di Cignana, Zermatt-Saas Zone, Western Alps." *Lithos* 42: 147–189. https://doi.org/10.1016/S0024-4937(97)00041-8.

Roedder, E. 1984. *Fluid Inclusions. Reviews in Mineralogy*. Vol. 12, 644. Mineralogical Society of America.

Rubatto, D., and S. Angiboust. 2015. "Oxygen Isotope Record of Oceanic and High-Pressure Metasomatism: A P–T–Time–Fluid Path for the Monviso Eclogites (Italy)." *Contributions to Mineralogy and Petrology* 170: 44. https://doi.org/10.1007/s00410-015-1198-4.

Rubatto, D., and J. Hermann. 2001. "Exhumation as Fast as Subduction?" *Geology* 29: 3–6.

Rubatto, D., and J. Hermann. 2003. "Zircon Formation During Fluid Circulation in Eclogites (Monviso, Western Alps): Implications for Zr and Hf Budget in Subduction Zones." *Geochimica et Cosmochimica Acta* 67: 2173–2187.

Rupke, L., J. P. Morgan, M. Hort, and J. A. D. Connolly. 2004. "Serpentine and the Subduction Zone Water Cycle." *Earth and Planetary Science Letters* 223: 17–34. https://doi.org/10.1016/j.epsl.2004.04.018.

Sandrone, R., P. Cadoppi, R. Sacchi, and P. Vialon. 1993. "The Dora-MairaMassif." In *Pre-Mesozoic Geology in the Alps*, 317–325. Berlin, Heidelberg: Springer.

Scambelluri, M., and P. Philippot. 2001. "Deep Fluids in Subduction Zones." *Lithos* 55: 213–227. https://doi.org/10.1016/S0024-4937(00)00046-3.

Scambelluri, M., G. Piccardo, P. Philippot, A. Robbiano, and L. Negretti. 1997. "High Salinity Fluid Inclusions Formed From Recycled Seawater in Deeply Subducted Alpine Serpentinite." *Earth and Planetary Science Letters* 148: 485–499. https://doi.org/10.1016/S0012-821X(97)00043-5.

Scambelluri, M., P. Bottazzi, V. Trommsdorff, et al. 2001. "Incompatible Element-Rich Fluids Released by Antigorite Breakdown in Deeply Subducted Mantle." *Earth and Planetary Science Letters* 192: 457–470.

Scambelluri, M., J. Fiebig, N. Malaspina, O. Müntener, and T. Pettke. 2004. "Serpentinite Subduction: Implications for Fluid Processes and Trace-Element Recycling." *International Geology Review* 46: 595–613. https://doi.org/10.2747/0020-6814.46.7.595.

Scambelluri, M., T. Pettke, and E. Cannaò. 2015. "Fluid-Related Inclusions in Alpine High-Pressure Peridotite Reveal Trace Element Recycling During Subduction-Zone Dehydration of Serpentinized Mantle (Cima di Gagnone, Swiss Alps)." *Earth and Planetary Science Letters* 429: 45–59. https://doi.org/10.1016/j.epsl.2015.07.060.

Schmid, S. M., O. A. Pfiffner, N. Froitzheim, G. Schönborn, and E. Kissling. 1996. "Geophysical-Geological Transect and Tectonic Evolution of the Swiss-Italian Alps." *Tectonics* 15: 1036–1064. https://doi.org/10.1029/96TC00433.

Schmid, S. M., E. Kissling, T. Diehl, D. J. J. van Hinsbergen, and G. Molli. 2017. "Ivrea Mantle Wedge, Arc of the Western Alps, and Kinematic Evolution of the Alps–Apennines Orogenic System." *Swiss Journal of Geosciences* 110: 581–612. https://doi.org/10.1007/s00015-016-0237-0.

Schmidt, M. W., and S. Poli. 2014. "Devolatilization During Subduction." In *Treatise on Geochemistry*, 669–701. Pergamon, Oxford, UK: Elsevier. https://doi.org/10.1016/B978-0-08-095975-7.00321-1.

Schmitz, M. D., and B. Schoene. 2007. "Derivation of Isotope Ratios, Errors, and Error Correlations for U-Pb Geochronology Using 205 Pb- 235 U-(233 U)-spiked Isotope Dilution Thermal Ionization Mass Spectrometric Data." *Geochemistry, Geophysics, Geosystems* 8: 2006GC001492. https://doi.org/10.1029/2006GC001492.

Schwartz, S., J. M. Lardeaux, P. Tricart, S. Guillot, and E. Labrin. 2007. "Diachronous Exhumation of HP-LT Metamorphic Rocks From South-Western Alps: Evidence From Fission-Track Analysis." *Terra Nova* 19: 133–140. https://doi.org/10.1111/j.1365-3121.2006.00728.x.

Schwartz, S., C. Gautheron, R. A. Ketcham, et al. 2020. "Unraveling the Exhumation History of High-Pressure Ophiolites Using Magnetite

(U-Th-Sm)/He Thermochronometry." *Earth and Planetary Science Letters* 543: 116359. https://doi.org/10.1016/j.epsl.2020.116359.

Selverstone, J., and Z. D. Sharp. 2013. "Chlorine Isotope Constraints on Fluid-Rock Interactions During Subduction and Exhumation of the Zermatt-Saas Ophiolite." *Geochemistry, Geophysics, Geosystems* 14: 4370–4391. https://doi.org/10.1002/ggge.20269.

Selverstone, J., G. Franz, S. Thomas, and S. Getty. 1992. "Fluid Variability in 2 GPa Eclogites as an Indicator of Fluid Behavior During Subduction." *Contr. Mineral. And Petrol.* 112: 341–357. https://doi.org/10.1007/BF00310465.

Sharp, Z. D., and J. D. Barnes. 2004. "Water-Soluble Chlorides in Massive Seafloor Serpentinites: A Source of Chloride in Subduction Zones." *Earth and Planetary Science Letters* 226: 243–254. https://doi.org/10.1016/j.epsl.2004.06.016.

Simon-Labric, T., Y. Rolland, T. Dumont, et al. 2009. "$^{40}Ar/^{39}Ar$ Dating of Penninic Front Tectonic Displacement (W Alps) During the Lower Oligocene (31–34 Ma)." *Terra Nova* 21: 127–136. https://doi.org/10.1111/j.1365-3121.2009.00865.x.

Smye, A. J., and P. C. England. 2023. "Metamorphism and Deformation on Subduction Interfaces: 2. Petrological and Tectonic Implications." *Geochemistry, Geophysics, Geosystems* 24: e2022GC010645. https://doi.org/10.1029/2022GC010645.

Soret, M., G. Bonnet, P. Agard, et al. 2022. "Timescales of Subduction Initiation and Evolution of Subduction Thermal Regimes." *Earth and Planetary Science Letters* 584: 117521. https://doi.org/10.1016/j.epsl.2022.117521.

Spandler, C., and J. Hermann. 2006. "High-Pressure Veins in Eclogite From New Caledonia and Their Significance for Fluid Migration in Subduction Zones." *Lithos* 89: 135–153. https://doi.org/10.1016/j.lithos.2005.12.003.

Spandler, C., J. Hermann, K. Faure, J. A. Mavrogenes, and R. J. Arculus. 2008. "The Importance of Talc and Chlorite "Hybrid" Rocks for Volatile Recycling Through Subduction Zones; Evidence From the High-Pressure Subduction Mélange of New Caledonia." *Contributions to Mineralogy and Petrology* 155: 181–198. https://doi.org/10.1007/s00410-007-0236-2.

Spandler, C., T. Pettke, and D. Rubatto. 2011. "Internal and External Fluid Sources for Eclogite-Facies Veins in the Monviso Meta-Ophiolite, Western Alps: Implications for Fluid Flow in Subduction Zones." *Journal of Petrology* 52: 1207–1236. https://doi.org/10.1093/petrology/egr025.

Stacey, J. S., and J. D. Kramers. 1975. "Approximation of Terrestrial Lead Isotope Evolution by a Two-Stage Model." *Earth and Planetary Science Letters* 26: 207–221.

Stipp, M., H. Stünitz, R. Heilbronner, and S. M. Schmid. 2002. "The Eastern Tonale Fault Zone: A 'Natural Laboratory' for Crystal Plastic Deformation of Quartz Over a Temperature Range From 250 to 700°C." *Journal of Structural Geology* 24: 1861–1884.

Strzerzynski, P., S. Guillot, P. H. Leloup, et al. 2012. "Tectono-Metamorphic Evolution of the Briançonnais Zone (Modane-Aussois and Southern Vanoise Units, Lyon Turin Transect, Western Alps)." *Journal of Geodynamics* 56–57: 55–75. https://doi.org/10.1016/j.jog.2011.11.010.

Taetz, S., T. John, M. Bröcker, C. Spandler, and A. Stracke. 2018. "Fast Intraslab Fluid-Flow Events Linked to Pulses of High Pore Fluid Pressure at the Subducted Plate Interface." *Earth and Planetary Science Letters* 482: 33–43. https://doi.org/10.1016/j.epsl.2017.10.044.

Tomascak, P. B., E. J. Krogstad, and R. J. Walker. 1996. "U-Pb Monazite Geochronology of Granitic Rocks From Maine: Implications for Late Paleozoic Tectonics in the Northern Appalachians." *Journal of Geology* 104: 185–195.

Ujiie, K., H. Saishu, Å. Fagereng, et al. 2018. "An Explanation of Episodic Tremor and Slow Slip Constrained by Crack-Seal Veins and Viscous Shear in Subduction Mélange." *Geophysical Research Letters* 45: 5371–5379. https://doi.org/10.1029/2018GL078374.

Vallis, F., and M. Scambelluri. 1996. "Redistribution of High-Pressure Fluids During Retrograde Metamorphism of Eclogite-Facies Rocks (Voltri Massif, Italian Western Alps)." *Lithos* 39: 81–92. https://doi.org/10.1016/S0024-4937(96)00012-6.

Van den Kerkhof, A. M., and U. F. Hein. 2001. "Fluid Inclusion Petrography." *Lithos* 55: 27–47.

Van Hinsberg, V. J., J. C. Schumacher, S. Kearns, et al. 2006. "Hourglass Sector Zoning in Metamorphic Tourmaline and Resultant Major and Trace-Element Fractionation." *American Mineralogist* 91: 717–728. https://doi.org/10.2138/am.2006.1920.

Vanko, D. A. 1988. "Temperature, Pressure, and Composition of Hydrothermal Fluids, With Their Bearing on the Magnitude of Tectonic Uplift at Mid-Ocean Ridges, Inferred From Fluid Inclusions in Oceanic Layer 3 Rocks." *Journal of Geophysical Research* 93: 4595–4611.

Verlaguet, A., D. Bonnemains, C. Mével, et al. 2020. "Fluid Circulation Along an Oceanic Detachment Fault: Insights From Fluid Inclusions in Silicified Brecciated Fault Rocks (Mid-Atlantic Ridge at 13°20'N)." *Geochemistry, Geophysics, Geosystems* 22: 1–32. https://doi.org/10.1029/2020GC009235.

Vermeesch, P. 2018. "IsoplotR: A Free and Open Toolbox for Geochronology." *Geoscience Frontiers* 9: 1479–1493. https://doi.org/10.1016/j.gsf.2018.04.001.

Vitale, S., L. Fedele, F. D. A. Tramparulo, and E. P. Prinzi. 2019. "Fault Rocks Within the Blueschist Metabasalts of the Diamante–Terranova Unit (southern Italy): Potential Fossil Record of Intermediate-Depth Subduction Earthquakes." *Geological Magazine* 156: 1771–1782.

Williams, I. S., and S. Claesson. 1987. "Isotopic Evidence for the Precambrian Provenance and Caledonian Metamorphism of High Grade Paragneisses From the Seve Nappes, Scandinavian Caledonides." *Contributions to Mineralogy and Petrology* 97: 205–217.

Wintsch, R. P., T. Byrne, and M. Toriumi. 1999. "Exhumation of the Sanbagawa Blueschist Belt, SW Japan, by Lateral Flow and Extrusion: Evidence From Structural Kinematics and Retrograde *P-T-t* Paths." *Geological Society, London, Special Publications* 154: 129–155.

Woodhead, J. D., J. Hellstrom, J. M. Hergt, A. Creig, and R. Mass. 2007. "Isotopic and Elemental Imaging of Geological Materials by Laser Ablation Inductively Coupled Plasma-Mass Spectrometry." *Geostandards and Geoanalytical Research* 31: 331–343.

Yardley, B. W. D., and J. T. Graham. 2002. "The Origins of Salinity in Metamorphic Fluids: Origins of Salinity in Metamorphic Fluids." *Geofluids* 2: 249–256. https://doi.org/10.1046/j.1468-8123.2002.00042.x.

Zanoni, D., G. Rebay, and M. I. Spalla. 2016. "Ocean Floor and Subduction Record in the Zermatt-Saas Rodingites, Valtournanche, Western Alps." *Journal of Metamorphic Geology* 34: 941–961. https://doi.org/10.1111/jmg.12215.

Supporting Information

Additional supporting information can be found online in the Supporting Information section.